NTNU
Norwegian University of
Science and Technology

Effect of Fe and Mn Additions on Al Alloy Melt and Their Effect on Intermetallic Phase Formation

Authors
Kjetil-André Sponland
Sebastian Bjelde Grorud

40 ECTS
Department of Material Science and Engineering
Norwegian University of Science and Technology,

27.05.2019

Supervisor
Robert Fritzsch
Shahid Akhtar
Ragnhild Aune

Sammendrag av Bacheloroppgaven

Tittel:	**Effekt av Fe og Mn tilsetninger på Al-legeringssmelte og deres effekt på formasjon av intermetalliske faser**
Oppgave no.	IMA-B-10-2019
Dato:	27.05.2019
Deltakere:	Kjetil-André Sponland Sebastian Bjelde Grorud
Veiledere:	Robert Fritzsch Shahid Akhtar
Oppdragsgiver:	NTNU og Hydro
Kontaktperson:	Kjetil-André Sponland, ka.sponland@gmail.com, 99319889
Nøkkelord:	Aluminium, Intermetalliske faser, Jern, Mangan
Antall sider:	81
Antall vedlegg:	8
Tilgjengelighet:	Åpen

Sammendrag:

Dannelsen av jernholdige intermetalliske faser i 3103 og 6082 legeringer er forventet å bli et økende problem ettersom Fe nivåer øker i resikulert alumnium. Legeringer ble støpt med nominell wt%, 150 wt% og 200 wt% Fe og Mn med fire forskjellige rekkefølger på tilsattsen. Resultater ble innsamlet gjennom kjemsik analyse, metalografiske undersøkelser og mekansike tester. Økte Fe og Mn nivåer ble funnet til å øke mengden interetalliske utfellinger som endret de mekansike egenskapene til legeringen. Videre arbeid bør gjøres for å bruke FactSage til å kalkulere fasediagram for de forskjellige legeringene.

Summary of Graduate Project

Title:	**Effect of Fe and Mn Additions on Al Alloy Melt and Their Effect on Intermetallic Phase Formation**
Project no.	IMA-B-10-2019
Date:	27.05.2019
Authors:	Kjetil-André Sponland Sebastian Bjelde Grorud
Supervisor:	Robert Fritzsch Shahid Akhtar
Employer:	NTNU og Hydro
Contact Person:	Kjetil-André Sponland, ka.sponland@gmail.com, 99319889
Keywords:	Aluminium, Intermetallic phases, Iron, Manganese
Pages:	81
Attachments:	8
Availability:	Open

Abstract: The formation of iron intermetallic phases in the 3103 and 6082 alloys is expected to become an increasing problem as Fe levels increase in recycled Aluminum. Alloys were cast with nominal wt%, 150 wt% and 200 wt% Fe and Mn, with four different orders of adding the additives. Industry specifications were followed for the procedure. Results were obtained through chemical analysis, metallographic investigations and mechanical testing. Increased Fe and Mn levels were found to precipitate more intermetallic phases. This leads to an altering of the mechanical properties of the alloy. Further work should be put into the use of FactSage for modelling the different phase diagrams.

Preface

The purpose of this study is to examine the formation of intermetallic phases in the 3103 and 6082 alloys of aluminium containing different wt% iron and manganese. Further to study the effect of adding certain alloying elements in different sequence and stage of the melting and alloying process.

The project was completed at Gløshaugen, NTNU, at the department of materials science and engineering spring 2019.

We want to thank our main supervisor, Robert Fritzsch, for answering our questions and helping us with the experimental work. We would also like to thank professor Ragnhild Aune for giving us guidance. We would also like to thank Shahid Akhtar and Hydro for supplying us with materials and information.

Contents

List of Figures

List of Tables

1 Introduction

1.1 Background

The topic of the thesis is directly related to issues experienced by casthouses using the 3xxx- and 6xxx-series alloys. The goal is to observe the intermetallic phases present in the different alloys and study the effect of varying the amount and sequence of the alloying elements Fe and Mn.

The intermetallic phases are known for causing issues during the further processing of the generated alloys, and it is an acute quality issue if not treated correctly. The focus has therefore been directed towards the formation of the intermetallic phases, with anticipation of the amount and sequence of the addition of the alloying elements.

1.2 Objective and experimental work

The objective of this study is to elaborate on the effect of adding certain alloying elements in different amount and sequence and stage of the melting and alloying process and study the intermetallic phases present in the different alloys. The effect of this on the mechanical properties, the electrical conductivity and the microstructural characteristics of the material will be studied.

A specific receipt for the casting procedure has been supported and supervised by Hydro Aluminium. The casting practice, melt treatments and sample preparations followed a standardized method. The results have been obtained by mechanical testing, e.g. conductivity and tensile testing, by chemical analysis, spark testing and EDS, and by metallographic investigations, e.g. light microscope and SEM.

In this work, two different aluminium alloys are used, 3103 and 6082. For each of these alloys tests on nominal Fe and Mn composition (100%), Fe and Mn 150% composition, and Fe and Mn 200% composition are done. Additionally, each of the tests was conducted with four parallel slightly varied trials:

- 1. with iron and manganese added as cold metal in the cold crucible
- 2. with iron added prior the manganese when completely molten
- 3. with manganese added prior the iron when completely molten
- 4. iron and manganese added together when completely molten.

For the navigation through the various castings, a numbering system consisting of three digits was developed. 1. The first digit describes which series the sample is from, 2. the second digit describes the composition, and 3. the last digit describes which parallel the sample is from. E.g. 314 is a 3103 alloy, with 150wt% Fe and Mn, where Fe and Mn are added together when completely molten. From each casting, three different samples

types were taken, i) rapid solidified discs (RSD), ii) slow cooling samples (SC), and iii) tensile samples.

Table 1: Different alloying sequences for the parallel trials of the 3103-alloy are shown.

Parallel	**Before melting, cold crucible**	**After complete melting**
1	Al and all alloying elements together	-
2	Al and remaining alloying elements	Fe added + 10 min of stirring and degassing, Mn added + 10 min of stirring and degassing
3	Al and remaining alloying elements	Mn added + 10 min of stirring and degassing, Fe added + 10 min of stirring and degassing
4	Al and remaining alloying elements	Fe and Mn added together + 10 min of stirring and degassing

Table 2: Different alloying sequences for the parallel trials of the 6082-alloy are shown.

Parallel	**Before melting, cold crucible**	**After complete melting**
1	Al and all alloying elements together	-
2	Al and remaining alloying elements	Fe added + 10 min of stirring and degassing, Mn added + 10 min of stirring and degassing, Mg added + 10 min of stirring and degassing
3	Al and remaining alloying elements	Mn added + 10 min of stirring and degassing, Fe added + 10 min of stirring and degassing, Mg added + 10 min of stirring and degassing
4	Al and remaining alloying elements	Fe, Mn and Mg added together + 10 min of stirring and degassing

2 Theory

2.1 Aluminium and its alloys

Aluminium is the most widely used light metal, and the daily production rate in January 2019 was 171,1 thousand metric tonnes, while the same period in 2009 produced 100 thousand metric tonnes [15]. This is an increase of 71,1%. Aluminium is used in a variety of applications, and the different applications require different properties of the metal. To achieve these properties, aluminium has to be alloyed with different elements, called "alloying elements", changing and enhancing the characteristics of the material. These different alloys are given by a four-digit number, where the first digit classifies what alloying system the given alloy belongs to [16]. This can be seen in table 3.

Table 3: Shows the major alloying element in the different Al-series [13].

Series	Major alloying element(s)
1xxx	Aluminium >99%
2xxx	Copper
3xxx	Manganese
4xxx	Silicon
5xxx	Magnesium
6xxx	Magnesium-Silicon
7xxx	Zinc
8xxx	Other element
9xxx	Unused series

2.1.1 Aluminium alloy 3103

The 3xxx-alloy series are non-heat-treatable alloys, where the main alloying component is manganese (Mn). Mn is a microstructure modifying element, enhancing the tensile strength and corrosion properties of aluminium [17]. Non-heat-treatable alloys gain their strength from cold working or strain hardening, by increasing the dislocation- and vacancy densities, which again increases the strength of the alloy. Magnesium is a major alloying element which can amplify this effect [16][18].
The current project work is directly linked to the alloys used by Hydro Aluminium, *e.g.* the 3103 alloy. The wt% of the different alloying elements of the 3103 alloy can be found in table 4, where the nominal and maximum tolerable wt% are given.

Table 4: Chemical composition of the 3103 alloy, supplied by Hydro [14].

Alloying element	nom% - max% [wt%]
Si	0,10 - 0,15
Fe	0,55 - 0,60
Mn	1,00 - 1,08
Cu	0,00 - 0,01
Mg	0,00 - 0,03
Cr	0,00 - 0,03
Ni	0,00 - 0,01
Zn	0,00 - 0,01
Ti	0,00 - 0,02

To achieve the Fe and Mn content for the 150 wt% samples, 0,83-0,90 wt% Fe and 1,50-1,54 wt% Mn was added. To achieve the Fe and Mn content for the 200 wt% samples, 1,10-1,20 wt% Fe and 2,00-2,16 wt% Mn was added. The other alloying elements were kept constant for all the parallels.

2.1.2 Aluminium alloy 6082

The 6xxx-alloy series are heat-treatable alloys, where the main alloying components are magnesium (Mg) and silicon (Si). Magnesium is the major alloying element which provides substantial strengthening and improves the work hardening characteristics. Silicon is the most essential single alloying element. It is responsible for good castability, where it lowers the viscosity and shrinkage of the melt. Si has a lower weight than aluminium, so it reduces the total weight of the component, and it also reduces the thermal expansion in Al-Si alloys [17]. The current project work is directly linked to the alloys used by Hydro Aluminium, *e.g.* the 6082 alloy. The wt% of the different alloying elements of the 6082 alloy can be found in table 5, where the nominal and maximum tolerable wt% are given.

Table 5: Chemical composition of the 6082 alloy, supplied by Hydro [14].

Alloying element	nom% - max% [wt%]
Si	0,90 - 0,95
Fe	0,22 - 0,24
Mn	0,43 - 0,49
Cu	0,00 - 0,04
Mg	0,62 - 0,68
Cr	0,12 - 0,15
Zn	0,00 - 0,05
Ti	0,00 - 0,05

To achieve the Fe and Mn content for the 150 wt% samples, 0,33-0,36 wt% Fe and 0,65-0,74 wt% Mn was added. To achieve the Fe and Mn content for the 200 wt% samples,

0,44-0,48 wt% Fe and 0,86-0,98 wt% Mn was added. The other alloying elements were kept constant for all the parallels.

2.2 Alloying elements in aluminium and their effects

2.2.1 Iron in Al-alloys

Iron is considered as an impurity element in aluminium, adding larger quantities of this element has a negative effect, and can lead to the formation of complex intermetallic phases. These phases can strongly affect the mechanical properties of Al, as they usually form as needles, or sharp-edged phases, with tough and brittle characteristics. They can act as nucleation grains, but also as hard particles within the alloy structure, increasing the brittleness of the metal [19]. As seen in figure 1, Al can solve only limited amounts of Fe, and the solid solubility of Fe in Al at eutectic temperature is between 0.03-0.05 wt % [20]. For Al-Si alloys high concentrations of Fe can lead to formations of crystal Fe-bearing constitute phases. This may move hypo- and eutectic alloys into the hyper-eutectic area of the phase diagram where most of the particles form [3].

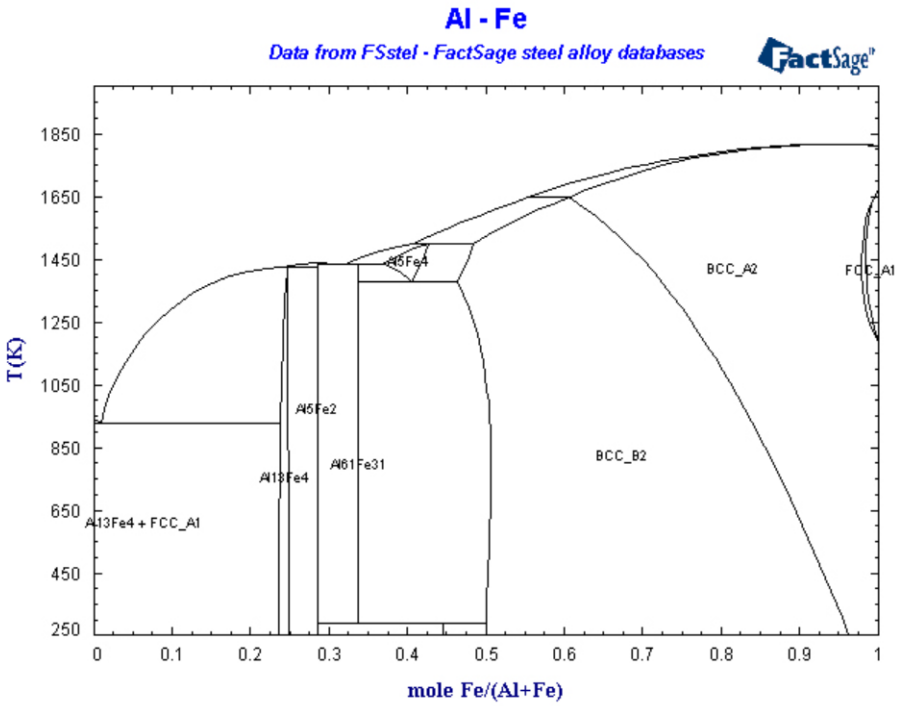

Figure 1: Phase diagram of Al-Fe.

There are two primary mechanisms for iron impurities to enter the aluminium melt [20]:

- Liquid Al is capable of dissolving Fe from furnace equipment and steel tools
- Via the addition of low-purity alloying materials, such as silicon, or via the addition of scrap that contains higher background Fe than the primary metal

During longer exposure times it is possible for the Fe content to reach 2 wt% with stan-

dard melt temperatures being ~700°C. For a metal melt held at a higher temperature of ~800°C, these levels could reach as high as 5 wt% [6]. A general statement and if possible, Fe levels in Al-alloys for industrial applications should be kept as low as possible. It is therefore important to have well-coated equipment if steel is used, and using alloying element and scrap from pure sources with a known history. The following formula can calculate the maximum amount of Fe before reaching critical levels.

$$Fe_{crit} \approx 0.075x[\%Si] - 0.05 \tag{2.1}$$

Where Fe_{crit} is the critical iron content, and [%Si] is the silicon percentage in the melt. The negative effects of Fe emerge at low primary levels but become more severe after surpassing the critical Fe level [6][20]. The Fe_{crit} is shown in Figure 3 for a Al-Fe-Si system containing 0-2 wt% Fe and 4-12 wt% Si.

2.2.2 Manganese in Al-alloys

Mn is considered an ancillary addition to Al-alloys as a microstructure modifying element. The principal goal of Mn in the alloy is to achieve a strengthening effect. Mn is also a common alloying element used to counterbalance the harmful effects of iron [20]. Mn has a high degree of solubility in Al and generally is added in alloys in amounts from 0,1 to 1 wt%. The solubility of Mn decreases with increasing levels of Mg in the alloy [3][7].

2.2.3 Silicon in Al-alloys

Silicon is the most important alloying element in the Al industry and is present in almost all alloying systems. Si additions on Al improves the castability, giving the melt better fluidity, while also reducing shrinking. The density of Si is lower than Al's, ρ_{Si}=2330 kgm^{-3}, making Al-Si alloys lighter than pure Al. Si, as an alloying element, also reduces the thermal expansion experienced in Al-alloys [17].

2.2.4 Intermetallic phases in Al-alloys

An intermetallic phase is a stable phase, consisting of two or more metals, which form a structure with an ordered crystal structure and a defined stoichiometry. Intermetallic compounds can be characterized by their high melting points, hardness and are usually very brittle. In various cases, they are wanted in a structure for their defining properties, but in most cases, they are unwanted in aluminium alloys. The reason behind this can be found by the large difference of the ductile aluminium matrix and the stiff, brittle and sharp-edged intermetallic phases. This results in a weakening of the physical properties of the otherwise ductile aluminium matrix, but can also lead to a change in the chemical resilience of the alloy. Heat treatment of the alloys after casting can, among other things, alter the intermetallic phases in the alloy through diffusion. Heat treatment is used to a large extent on the 6xxx-series.

When studying the formation of intermetallic phases in as-cast industrial alloys, it can be hard to anticipate which phases will form. Phases may form at the hypo-, hyper- and eutectic areas on the phase diagram, and have different origins. The liquid properties of the different elements, as well as melt flow, might alter the composition in the melt during casting. When looking at five element or more compositions, one is moving out

of the well-confirmed areas on the formation of intermetallic phases.

A collection of relevant intermetallic phases are shown in table 7 collected from Al-Fe-Mg, Al-Fe-Mn, Al-Fe-Si, Al-Mn-Si, Al-Mn-Mg, Al-Fe-Mn-Si, Al-Fe-Mn-Mg, Al-Fe-Mn-Mg-Si systems.

In Al-Si alloys the formation of the β-Al_5FeSi is deemed the least desirable. This phase is usually suppressed through; adding Mn creating α-$Al_{15}(Fe, Mn)_3Si_2$, increasing the cooling rate creating α-Al_5FeSi or interaction with Mg creating π-$Al_8FeMg_3Si_6$. The two different α-phases have different crystal structures[7].

2.2.5 Al-Fe

Due to iron's low solid solubility, it forms intermetallic phases with Al and various alloying elements. Between Al and Fe, the most common phases to arise are Al_3Fe and Al_6Fe. The Al-Fe binary phase diagram is shown in figure 2.

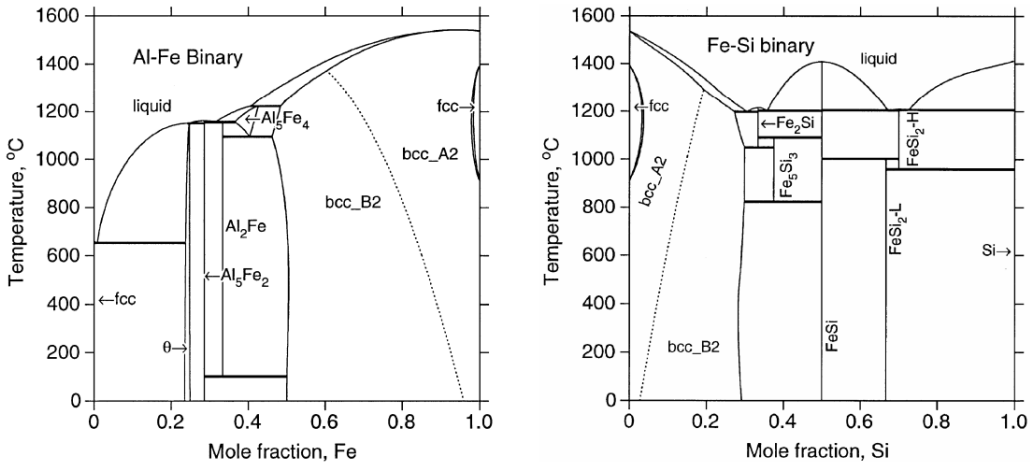

Figure 2: Shows the Al-Fe and Fe-Si binary phase diagrams [1].

2.2.6 Al-Fe-Si

The Al-Fe-Si system is a common but complicated system. In the current literature, there are ten known ternary intermetallic phases, whereas seven of them are stable. These phases are α, β, γ, δ, τ_1, τ_{23}, and τ, and out of these, the α- and β-phases dominate [21]. The β-phase, Al_5FeSi, forms a platelet-like intermetallic phase. This leads to reduced strength and ductility in the alloy. The stoichiometry of the phases varies in literature due to different purities of the aluminium, but the most common model for the α-phase is Al_8Fe_2Si.

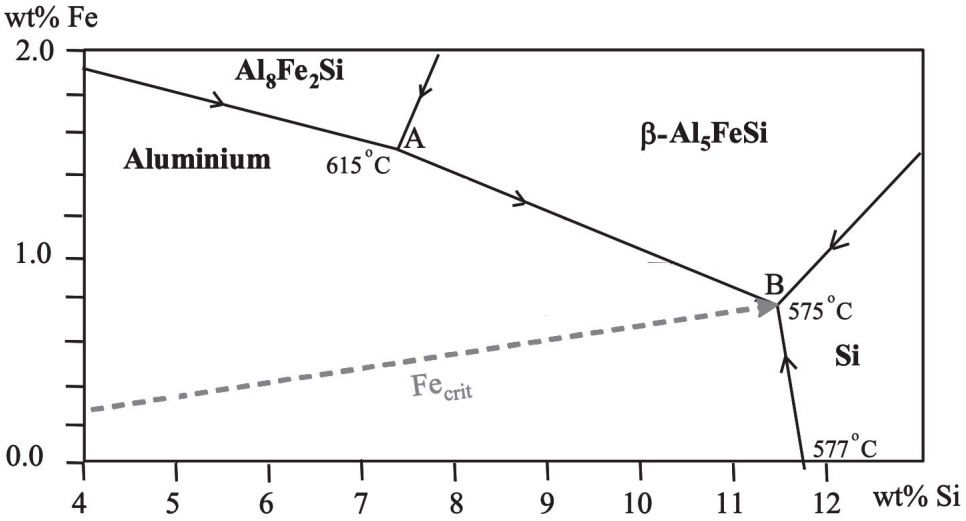

Figure 3: Shows a simplified liquidus projection of the Al-Fe-Si system calculated by Taylor. The figure has been simplified [2].

In addition to the phases described, Si has a solubility in the Al_3Fe in the range of 0,2% to 6%. The Al-Fe-Si system is very complex, and there are still ongoing debates about the existence of certain ternary phases[3]. For industry alloys, the coexistence of several of these phases is likely. The morphology of the phases may also be altered as a function of their origin, making it hard to predict and visually identify them [3][22].

2.2.7 Al-Mn-Si

Al-Si-Mn alloys without the Mg, Fe and Cu are generally not used. Nevertheless, the diagram is important when studying the more complex Al-Fe-Mn-Si system. The formation of Al_6Mn and Al_4Mn is shown in figure 4. These are of importance for alloys containing Fe and Mn.

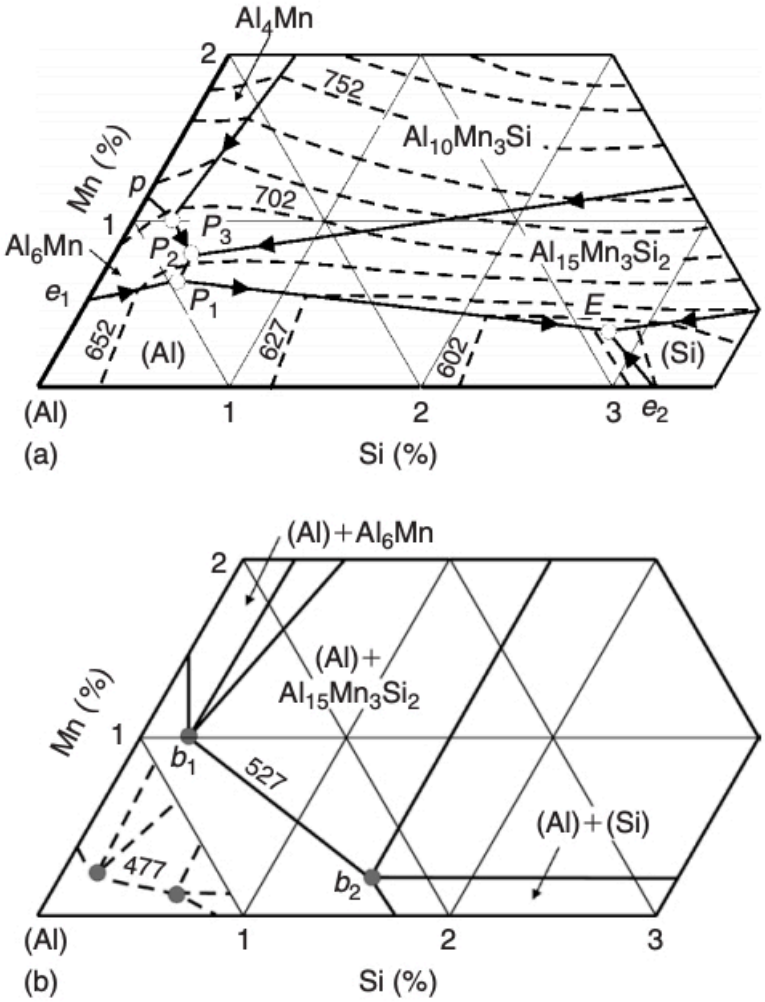

Figure 4: This figure demonstrates the ternary Al-Mn-Si phase diagram in the Al-rich corner: a)liquidus projections and b) distribution of phases in solid state [3].

2.2.8 Al-Fe-Mn

For the Al-Fe-Mn system, only Al_3Fe (often noted α-Al_3Fe) and Al_6FeMn can be at equilibrium with Al. Fe substitutes the Mn in the Al_6Mn and forms $Al_{12}FeMn$. Mn has a solubility of 4-5% in the α-Al_3Fe. Mn also has a stabilizing of the metastable Al_6(FeMn)as shown in figure 5[3]. The growth of this phase is shown in figure 6.

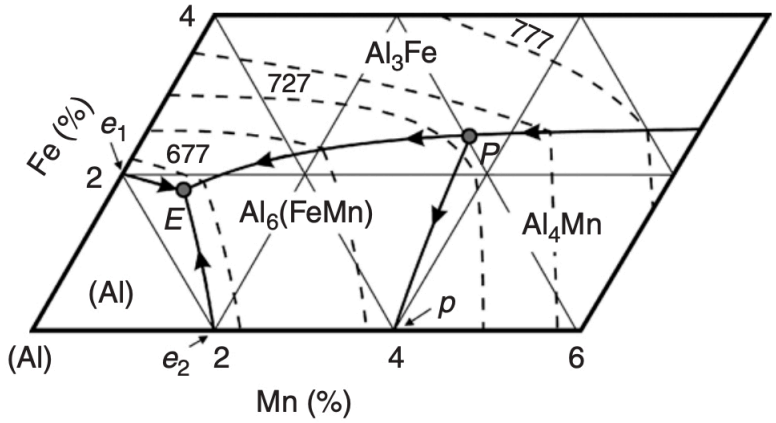

Figure 5: Shows the ternary Al-Fe-Mn phase diagram in the Al-rich corner with liquidus projection [3].

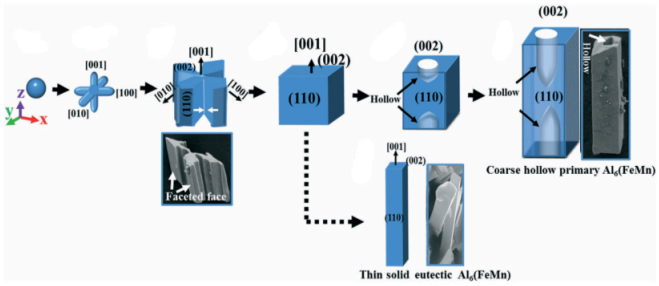

Figure 6: Illustrates the growth of the Al_6(Fe, Mn) intermetallic phase [4]. The figure shows the different growth morphologies for eutectic and primary Al_6(Fe, Mn). The figure has been simplified.

The Al_6(Fe, Mn) intermetallic phase has been found to vary in morphology dependent on the chemical compositions[5]. This effect can be seen in figure 7 and in table 6.

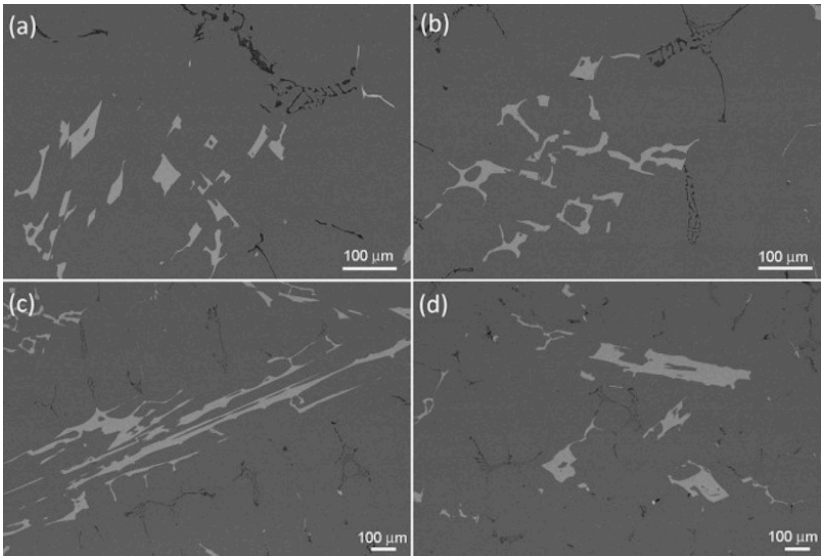

Figure 7: Different morphologies for the Al_6(Fe, Mn) based on the composition; (a)block (b)Chinese script (c)strip-like and (d) platelet-like [5]. The compositions of the phases can be seen in table 6

Table 6: Shows different morphologies (figure 7) of the Al_6(Fe, Mn)-phase based on the chemical composition of Fe and Mn [5].

Element (at%)	(a) Block	(b) Chinese script	(c) Platelet-like	(d) Flake
Al	84.60	84.73	84.67	83.89
Mn	5.15	5.39	8.81	8.46
Fe	10.25	9.88	6.52	7.65

2.2.9 Al-Fe-Mn-Si

In alloying systems with Si and Mn present a common quaternary intermetallic phase is Al_{15}(Fe, Mn)$_3Si_2$. This phase is also known as α-phase, but it dominates the other α-phase when Mn is present [6]. Both α-phases have a script-like morphology, known as "Chinese script", but the introduction of Mn in the α-phase leads to a more block-like Chinese script. The Al_{15}(Fe, Mn)$_3Si_2$-phase can also sometimes occur as polyhedral crystals [2]. These morphologies are preferred to the β-phase, which has a needle-like structure that has negative effects on the mechanical properties on the material. Figure 8 shows the morphology of the α-, β, and π-phase mentioned above.

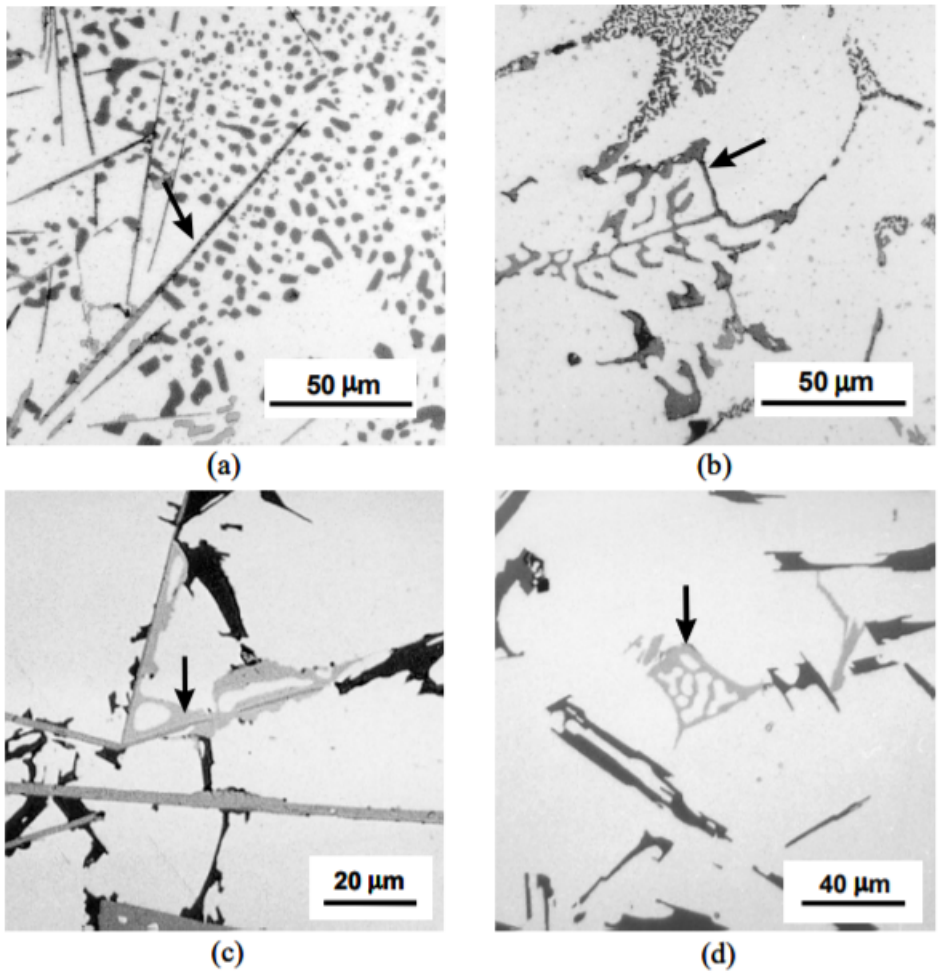

Figure 8: Overview of the morphology of relevant intermetallic phases in Al-5%Si-1%Cu-0.5%Mg-(Fe). (a) shows the β-phase; (b) shows the script-like α-Al_8Fe_2Si; (c) shows the π-phase emerging from the β-phase, and (d) shows the script-like π-phase [6].

European Research Program Al-Fe-Mn-Si did a study on annealed samples at 550°C for 12 weeks. They confirmed the phase distribution as seen in figure 9 made by Mondolfo et al.[7]. The diagram shows a lack of quaternary phases, but a broad homogeneity range on the basis of the $Al_{15}(Fe, Mn)_3Si_2$.

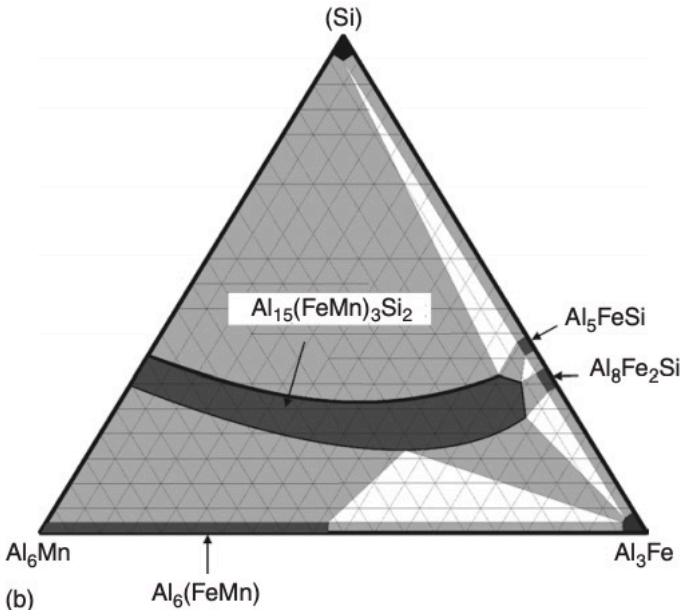

Figure 9: The solid-state phase fields as reported by Mondolfo et al. [7] showing the broad homogeneity of range in the Al_{15}(Fe, Mn)$_3Si_2$-phase, and lack of quaternary phases [3].

For alloys containing a high Si wt% (10–14%Si, 0–3%Fe, and 0–4%Mn), it has been claimed that a quaternary compound Al_{16}(Fe, Mn)$_4Si_3$ may exist [3]. For alloys containing a $\frac{Mn}{Fe}$-ratio > 1,1, solidification will be completed at 575°C. The products will be Al, Al_{16}(Fe, Mn)$_4Si_3$, $Al_{15}Mn_3Si_2$ and Si forming in the solid state [3].

2.2.10 Al-Fe-Mg-Si

The introduction on Mg to the system introduces two new relevant intermetallic phases; Mg_2Si and π-$Al_8FeMg_3Si_6$. The π-phase is often closely related to the peritectic reaction towards the β-phase. The π-phase is often found growing out of β-phases when looking at the grain structure, as shown in figure 8 (c)(d). The conversion from β-phase to Mg_2Si and π-phase is shown in the chemical equation below;

$$L + \beta(Al_5FeSi) \rightarrow Al + Mg_2Si + \pi(Al_8FeMg_3Si_6) \quad \text{or} \quad Al + Si + \pi(Al_8FeMg_3Si_6)$$

The π-phase has a narrow homogeneity range around the chemical formula $Al_8FeMg_3Si_6$ (10,9%Fe, 14,1%Si, 32,9%Mg). In the Al-Fe-Mg-Si systems, several binary and ternary phases can be at equilibrium, as shown in table 7 (Al_3Fe, Mg_2Si, Al_8Fe_2Si, Al_5FeSi and Si [3].

2.2.11 Al-Fe-Mn-Si-Mg

Mn in Al-Mg systems has been found to transform Al_3Fe to the metastable Al_6(Fe, Mn) [23]. Increasing the cooling time further refines this phase [5]. In the Al-Fe-Mn-Mg systems, the Al_6(Fe, Mn) will then transform to the stable Al_{13}(Fe, Mn) but it has been found that increasing Mn stabilizes the Al_6(Fe, Mn) phase [4].

Table 7: Show the non-variant phase reactions in the aluminum corner of the important phase diagrams for Al-Si-Fe-Mn and Al-Si-Fe-Mn-Mg systems[3]

System	Non-variant phase reactions	Temp (°C)	Source
Al-Fe-Mg	$L \Rightarrow (Al) + Al3Fe + Al8Mg5$	451	[7], [24], [25]
Al-Fe-Mn	$L + Al3Fe + Al4Mn \Rightarrow Al6(FeMn)$	727730	[26], [7], [24], [27]
	$L \Rightarrow (Al) + Al3Fe + Al6(FeMn)$	654	[7], [27]]
Al-Fe-Si	$L \Rightarrow (Al) + Al5FeSi + (Si)$	576	[7], [28]
	L +Al8Fe2Si $\Rightarrow (Al) + Al5FeSi$	629	[7],[28],[29]
	L +Al3Fe $\Rightarrow (Al)$+α-Al8Fe2Si	611	[7],[29]
	γ-AlFeSi		[7]
Al-Mg-Mn	$L + Al4Mn \Rightarrow Al6Mn + Al10(MgMn)3(18\%Mg, 2–3\%Mn)$		[7]
	$L + Al6Mn \Rightarrow (Al) + Al10(MgMn)3(22\%Mg, < 0.5\%Mn)$		[7]
	$L \Rightarrow (Al) + Al8Mg5 + Al10(MgMn)3(33\%Mg, 0.1–0.2\%Mn)$	437	[7]
Al-Mg-Si	$L \Rightarrow (Al) + Mg2Si(quasi - binarycross - section)$	595	[[7],[24], [25]]
	$L \Rightarrow (Al) + (Si) + Mg2Si$	555	[[7],[24], [25]]
	$L \Rightarrow (Al) + Mg2Si + Al8Mg5$	449	
Al-Mn-Si	L +Al4Mn $\Rightarrow$ Al6Mn + Al10Mn3Si	690	
	L +Al10Mn3Si $\Rightarrow$ Al6Mn + Al15Mn3Si2	655-657	[[30],[7],[24],[31],[32]]
	L +Al6Mn $\Rightarrow (Al)$ + Al15Mn3Si2	648-649	
	$L \Rightarrow (Al) + (Si) + Al15Mn3Si2$	573–574	
Al-Fe-Mg-Si	$L \Rightarrow (Al) + Al3Fe + Mg2Si$	>587	
	L +Al3Fe $\Rightarrow (Al) + Mg2Si + Al8Fe2Si$	586	
	L +Al8Fe2Si $\Rightarrow (Al) + Mg2Si + Al5FeSi$	576	
	L +Al5FeSi $\Rightarrow (Al) + Mg2Si + Al8FeMg3Si6$	568	
	L +Al5FeSi $\Rightarrow (Al) + (Si) + Al8FeMg3Si6$	567	
	$L \Rightarrow (Al) + (Si) + Mg2Si + Al8FeMg3Si6$	554	
	$L \Rightarrow (Al) + Al3Fe + Al8Mg5 + Mg2Si$	448	
Al-Fe-Mn-Si	L +Al3Fe +Al6(FeMn) $\Rightarrow (Al) + Al15(FeMn)3Si2$	648	[7]
	L +Al3Fe $\Rightarrow (Al) + Al8Fe2Si + Al15(FeMn)3Si2$	627-632	[7]
	L +Al8Fe2Si $\Rightarrow (Al) + Al5FeSi + Al15(FeMn)3Si2$	587-607	[7]
	L +Al5FeSi $\Rightarrow (Al) + (Si) + Al15(FeMn)3Si2$	575	[7]
	L +Al4FeSi2 $\Rightarrow$ (Si) + Al5FeSi + Al16(FeMn)4Si3	596	[32],[33],[34]
	$L \Rightarrow (Al) + (Si) + Al16(FeMn)4Si3$	576	[32],[33],[34]
	$L \Rightarrow (Al) + (Si) + Al5FeSi + Al16(FeMn)4Si3$	574	[32],[33],[34]
	$L \Rightarrow (Al) + (Si) + Al15Mn3Si2 + Al16(FeMn)4Si3$	575	[32],[33],[34]
Al-Fe-Mg-Mn-Si	$L \Rightarrow (Al) + (Si) + Mg2Si + Al15(FeMn)3Si2 + Al8feMg3Si6$		[7]
	$L + Al5FeSi \Rightarrow (Al) + (Si) + Al15(FeMn)3Si2 + Al8FeMg3Si6$		[7]
	$L \Rightarrow (Al) + Al3Fe + Mg2Si + Al8Mg5 + Al10(MgMn)3$		

2.3 Thermodynamic

Earlier studies have found problems with the dissolution on Mn in Al-melts. This is due to the relatively low heat conduction properties of Mn. This forms a freeze-on layer of intermetallic phases on the surface of the Mn-briquettes and hinders dissolving. This process is shown in figure 10.

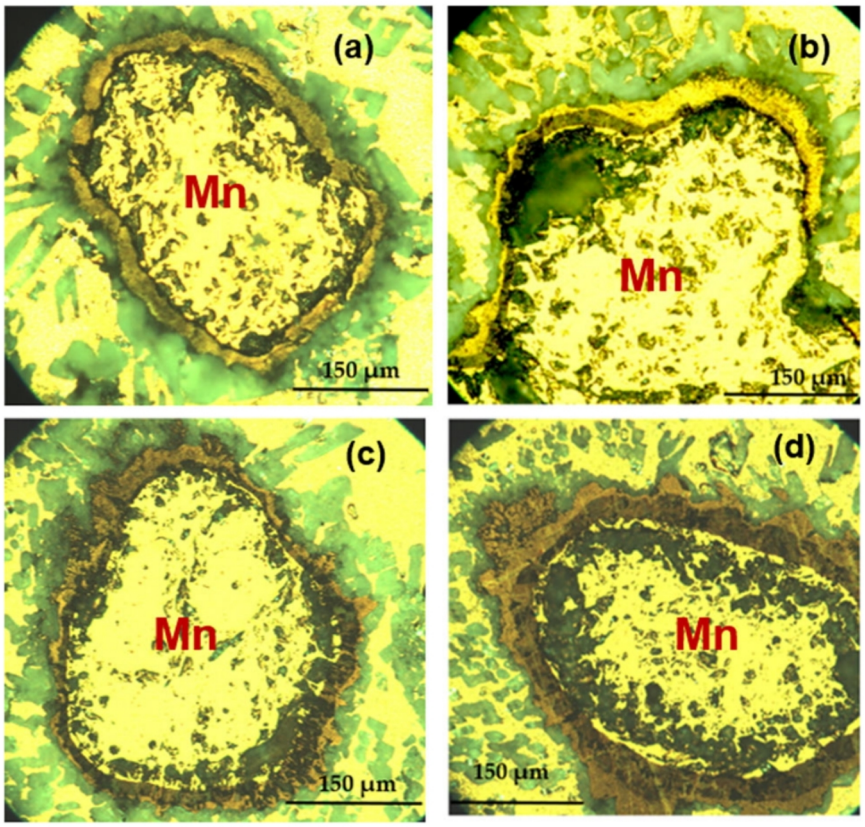

Figure 10: Light microscope images (LMI) of dissolved Mn in Al-melt with dark green intermetallic phases forming around as a freeze-on layer. The LMIs are taken after various dissolution times: a) 2 min, b) 5 min, c) 8 min, and d) 16 min [8].

From SEM- and EDX analysis, the three intermetallic phases forming around the dissolved Mn were determined to be γ_2, $Al_{11}Mn_4$ and μ. The low diffusion coefficient of γ_2 was found to be the most significant hindering factor for diffusion flow of Al atoms towards the dissolved Mn [8].

2.3.1 Diffusion and Fick's 2nd law

How the different alloying elements dissolve into the aluminium melt is described by Fick's 2nd law of diffusion.

$$\frac{\partial C}{\partial t} = D\frac{\partial^2 C}{\partial x^2} \tag{2.2}$$

$\frac{\partial C}{\partial t}$ [$cm^{-3}s^{-1}$] describes the change of concentration over a given time, t [s]. This is proportional to D, the diffusion coefficient of the material [cm^2/s], times the second derivative of the change of concentration per distance x [cm^{-3} cm^{-2}]. This equation can be used to describe how the alloying elements diffuse into the aluminium melt. The equation describes this phenomenon in one dimension only, but for two or more

dimensions, the following equation applies.

$$\frac{\partial C}{\partial t} = D\Delta C \tag{2.3}$$

Where $\Delta = \nabla^2$ is the Laplace operator.

2.3.2 Nucleation

During a phase transformation, generally at least one phase will change chemical and structural composition. This change does not usually occur instantaneously and is divided into two stages; nucleation and growth.
Nucleation is the formation of a small collection of amounts of atoms (sometimes only hundreds) that collect together and start the process of creating the new phase. The formation of the new nuclei is controlled by Gibbs free energy. For the formation of a new phase to be spontaneous, the free energy needs to have a negative value. The nucleation of a phase can happen through two mechanisms referred to as homogeneous and heterogeneous nucleation. In homogeneous nucleation, the new phase form uniformly in the parent phase. A heterogeneous nucleation happens at a structural nonuniform such as grain boundaries, crucible wall, impurities grains, or similar in the parent phase. A simplified equation for a spherical solid in a liquid can be seen in the equation below:

$$\Delta G = \frac{4}{3}\pi r^3 \Delta G_v + 4\pi r^2 \gamma \tag{2.4}$$

Where ΔG_v is the difference in free energy between solid and liquid form, and γ is the surface free energy, which is positive. From the equation, one can see that the ΔG_v is the driving force. The ΔG_v free energy is increased by undercooling the parent phase.

For heterogeneous nucleation the surface free energy, γ, decreases. This happens because of the nuclei forming on an existing surface. The same critical radius will be needed in both nucleation processes, but the heterogeneous can happen with much less undercooling.

2.3.3 Crystal growth and heat transfer

In metallurgy, time and temperature are two important parameters. During solidification, the temperature gradient, which is defined by the time and temperature, greatly influences the microstructure of the material. It is valid for all metals that higher rates of solidification lead to smaller grain size [35]. It was also found that a decrease in cooling time led to an increase in the formation of β-AlFeSi, which gives an indication about the thermodynamics, characterizing the formation of β-AlFeSi to be energetically favourable. The α-AlFeSi were smaller at higher cooling rates [36].

Grains and grain-growth

Aluminium is a polycrystalline material, meaning that the microstructure is divided into many small crystalline areas. These areas are called grains. Inside the grains, the atomic packing is repeated structurally in all three dimensions. The grains are separated by grain boundaries, the grains are built the same, but the orientation of the crystal structure is what separates them. Grain boundaries are a popular area for precipitations to form,

and these precipitations are called grain boundary precipitations [37]. The formation of grains from the melt is shown in figure 11.

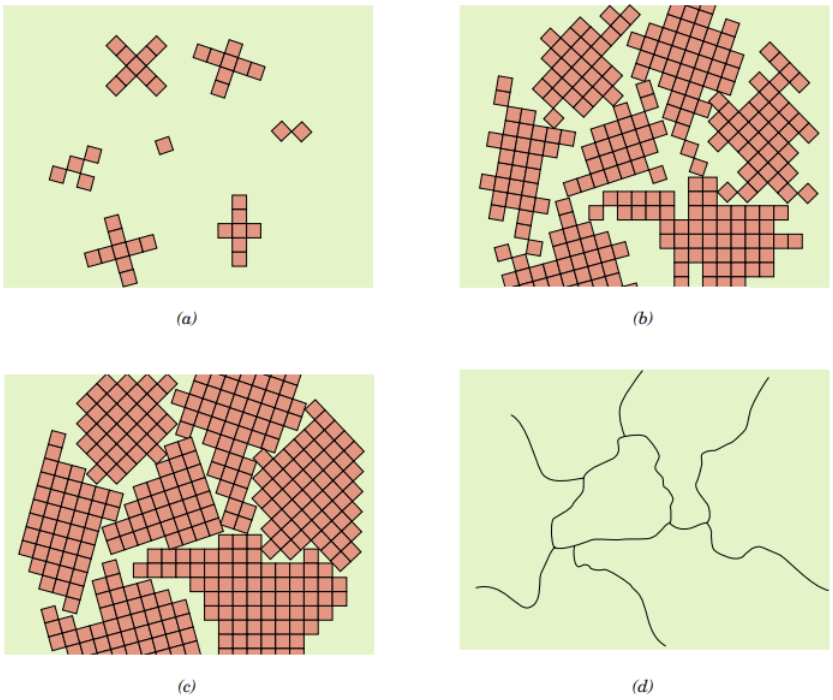

Figure 11: A schematic illustration of various stages of grains forming. (a) Shows nucleation in the melt. (b) Growth of the individual crystals, some boundaries are forming. (c) The material is solidified, and the grains are separated by grain boundaries with irregular shapes. (d) Grain boundaries represented by dark lines [9].

Grain growth is a process where two or more grains grow together and becoming one larger grain. This can be done when external energy is transferred to the material, e.g. heat. Grain growth is a complicated process where many individual factors contribute, and many approaches have been made to model this [38][39][40]. Grain growth is often an unwanted process in metals due to the lowering of strength for the material [41].

The size, distribution and morphology of the grains affect the mechanical properties of the material. Metallurgists take advantage of the grains and grain-boundaries by deforming the metal to induce defects. These defects strengthen the metal and increase its yield strength. An example of this is cold working. The cold working deforms the metal inducing dislocations in the microstructure. The more dislocations in the microstructure, the higher the yield strength, while the ductility decreases. The number of possible dislocations depends on the size and distribution of the grains.

2.3.4 FactSage and Thermodynamic modeling

FactSage is a module-based thermochemical database and software used to calculate chemical and thermodynamic systems [42]. The modules get their parameters and val-

ues from different thermochemical databases for each individual and general/broad compounds (pure substances) and solutions [43]. In this work, the module "Phase Diagram" is used with the FTlite database to calculate and plot relevant phase diagrams for the different alloying systems. The FTlite is a lite alloy database design for Al- and Mg-rich metals. The data from 781 binary systems and several dozen ternary systems have been used. Table 7 was used to verify the computed results.

The Gibbs energy of phases is used to calculate the phase equilibrium and phase boundaries. These values determine at what temperature, pressure and composition the different phases are present [44]. These calculations represent ideal solutions only; hence a real-world problem can behave differently, and other phases might dominate. Nevertheless; these analytic assumptions give an indication of the most probable phase composition and temperatures where the phases form.

When considering the validity of the phase diagram, Gibbs formulated the phase rule saying that;

$$P + F = C + N \tag{2.5}$$

In this equation, P represents the number of phases present, F the number for the degree of freedom (externally controlled variables), C the number of elements and stable compounds and N the number of no composition variables. The standard binary diagram can visualize two degrees of freedom through the X and Y axis. Studying the standard binary phase diagram for Al-Fe (fig. 2), one can see that; C=2 (Al and Fe) and N=1 (constant pressure = 1 atm). When looking at a two-phase area of the diagram, this gives P=2.

$$F = C + N - P = 3 - 2 = 1$$

This means that the composition of one of the phases present must be known, and here, only one degree of freedom can be used; either temperature or composition.
A ternary phase diagram would further be restricted to only be able to have one degree of freedom in the diagram on a two-dimensional plot. This is usually the composition.

2.4 Casting

Shrinkage

One of the issues with casting aluminium is the large density difference between molten and solid aluminium. At room temperature, pure Al has the density ρ_{Al}=2710 kgm^{-3}. When molten, the bondings between the Al-atoms are more extended than when at room temperature, because of the increased energy in the system. Pure Al shrinks by 6,7% when cast. This shrinkage can lead to problems when casting components as it can introduce unwanted defects. When Si is introduced to the system, the shrinkage decreases, and when the Si content is 12 wt%, the shrinkage is as low as 4,5% [45]. Other parameters that affect the castability of aluminium are Fluidity, macrosegregation, hot tearing, and porosity [46].

Macrosegregation

Macrosegregation is when the chemical composition varies within the microstructure, often as a result of low relative movement of the segregated liquid during solidification. This is unavoidable for all casting processes but becomes less of a problem when the convection in the melt is sufficient to create a uniform distribution of alloying elements. When the alloying elements are not uniformly distributed, it can have unfavourable effects on the alloy. Therefore, it is essential to have adequate convection in the melt [47].

Degassing

Degassing is the process where an inert gas is purged into the molten metal. There are many different degassing techniques, and different techniques can be combined. The use of Argon gas is industry standards, but this can be combined with ultrasonic vibrations, or ultrasonic vibrations can be used by itself. Degassing of Al-melt is standard practice in the industry, as degassing has two positive effects. The introduction of inert gas gives convection in the Al-melt, securing a uniform melt, and it gives impurities in the melt a surface to attach to, removing them from the melt. These impurities are, *e.g.* oxides and hydrogen. Degassing the Al-melt produces dross that needs to be removed from the melt before samples are taken [48].

2.5 Mechanical testing

Tensile testing

Tensile testing is one of the most fundamental mechanical testing methods. There are standardized procedures to measure materials yield strength (σ_y), tensile strength (σ_{TS}), Young's modulus (E), strain (ϵ), and elongation (%EL). These are important parameters that define materials mechanical properties.

To make comparisons between different tensile tests, a standard is needed. The *Standard Test Methods for Tension Testing of Metallic Materials* [49] describes the standard specimen sizes. The information obtained from the test can be useful when comparing different alloys or to determine the quality of a specific alloy.

The yield strength is calculated from the force, F [N], applied by the machine divided by the cross-sectional area, A [m^2] of the sample.

$$\sigma_y = \frac{F}{A} \tag{2.6}$$

The strain is calculated from the change of the specimen length, where L_0 [m] is the original length, and L [m] is the new length.

$$\epsilon = \frac{L - L_o}{L} = \frac{\Delta L}{L_0} \tag{2.7}$$

When these two parameters are known, they can be plotted in a graph with stress along the y-axis and strain along the x-axis. This curve can be used to calculate all the parameters mentioned above.

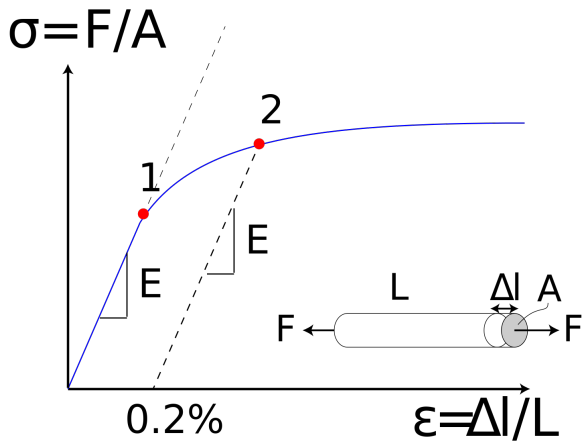

Figure 12: Schematic stress-strain curve [10].

2.6 Conductivity

Conductivity is a measurement of how well a given material is at conducting an electric current. This can be measured in % IACS (International Annealed Copper Standard), a percentage of the conductive properties of annealed copper [50]. A materials crystal structure defines the path of the electrons, and the grain boundaries act as a resistance to the electrons. Pure aluminium metal has better conductivity when comparing it to most alloys, where the only alloy with a better conductivity is with gold (Au) alloyed to Al. The addition of atoms of a different element affects the grain structure by creating imperfections. These imperfections act as resistance for the current, dropping the conductivity [51].

3 Methodology and Materials

3.1 Preparation for casting

3.1.1 Cutting of aluminium

The aluminium used for this project was supplied by Hydro, with a purity of 99,9999%. The aluminium rods were cut using a Struers Labotom-5 tabletop cutter, equipped with an abrasive SiC 20A25 blade. The aluminium was cut into lengths of 10-12 cm, resulting in blocks weighing approximately 1 kg.

3.1.2 Generating the different alloys

There were generated 12 different alloys for each of the 3103 and 6082 systems, with variety in iron (Fe) and manganese (Mn) content, and the sequence they were added. The different parallels can be seen in table 1 and 2.

3.1.3 Alloy composition

A composition calculator was created using MS Office ® Excel for the calculations of the levels of additives needed in the melt. The calculator was based on the max wt% for the alloys that Hydro would allow.

Most of the elements were added in their pure form (between 99,99% and 99,999%), while Ti and Cu were in a binary Al-system. Ti: 80wt% Ti - 20 wt% Al, and the Cu: 20wt% Cu - 80 wt% Al. Mn was added through two different sources; 20wt% Mn - 80 wt% Al alloy and Mn with an unknown fluxing agent. The iron used for these trials also contained an unknown fluxing agent. These are standard samples used in the industry today.

The aluminium metal and the different alloying metals have been weighted with Sartorius BL 6100. The scale has an accuracy of 0,1 gram and is shown in figure 13.

Figure 13: The scale used to weigh the Al and the alloying elements.

3.1.4 Furnace

The furnaces, Nabertherm No.87576 and No.87577, were sett to 750° Celsius. Argon gas was purged into the furnaces at a rate of 1,0 standard litre per minute (SLPM) during pre-heating and holding of the melt. An Alicat MC-10SLPM-D/5M scientific flow-meter was used to keep the gas flow constant at 1 SLPM, and the apparatus is shown in figure 16.

A small Nabertherm furnace, positioned in the centre of the two larger furnaces, as shown in figure 14 was used to pre-heat Mn-Al briquettes and tools to 600°Celsius.

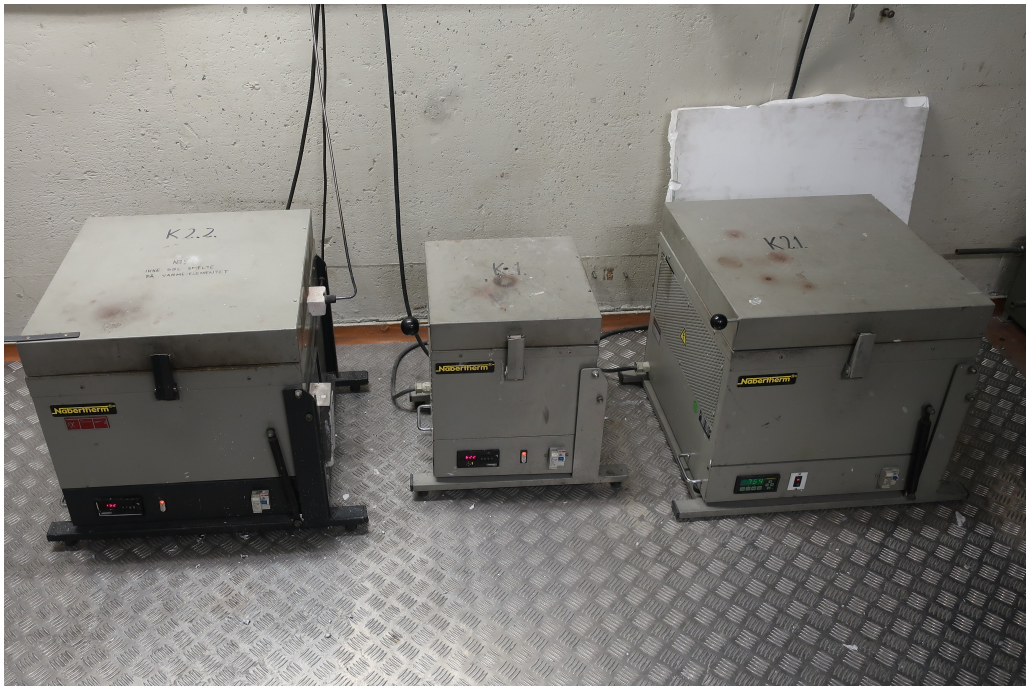

Figure 14: The three Nabertherm furnaces used during the casting trials.

3.1.5 Preparing equipment

For the castings, all the crucibles and metal tools were coated with Boron-nitrated solution. This was to prevent the reaction and adhesion with the aluminium alloys during castings.

The mould for the tensile test rods was preheated to 600 °Celsius to prevent differences in cooling rate on different castings.

3.1.6 Degassing and stirring

An old in-house made engine was used for the stirring process. A boron nitrite coated stainless steel stirrer was placed in the melt to homogenize the chemical composition and thermal gradients within the melt.

Argon gas was used for degassing. An Alicat MC-10SLPM-D/5M scientific flow-meter, shown in figure 16, was used to secure that the degassing procedure was the same for all the trails.

Figure 15: The flow-meter used to control the Ar-gas for purging and degassing.

A coated stainless steel rod with small holes was used for the initial trials to degas the melt. This had to be replaced after the first set of trails due to the rod dissolving in the melt.

Figure 16: Shows the fracture of the coated stainless steel degassing rod. The rod was subjected to Al-melt for 10-20 minutes at a time.

The new degassing rod have been built by combining an alumina-rod with a fine 80-grade ceramic foam filter. The filter and the rod have been connected and sealed by moldable cement, fiberfrax®. The rods were then coated in boron nitrite to avoid any chemical interactions with the alloys. One rod was made of alumina, while the other rod was copper plated with steel.

Figure 17: The homemade jig to hold the degassing rod and the engine used for stirring. During stirring and degassing, alumina-fibres were used to cover the open oven, preventing loss of heat.

3.2 Metallographic preparation

The RSD samples were cut in two, where one side was used for the spark test and the other for metallographic investigations. The samples were cut with a Struers Labotom-15 with an abrasive SiC 20A25 blade, and the machine is shown in figure 18.

Figure 18: Shows the cutter in which the samples were cut [11].

The samples were then polished with a Struers Tegramin-30 polishing machine. The

samples were polished in three steps, down to 1 μm following a standard Struers protocol and automated polishing systems. The machine used is shown in figure 19.

- 1. With a 9μm disc and Largo 9 as a suspension for 5 minutes
- 2. with a 6 μm disc and Mol3 as a suspension for 3 minutes
- 3. with a 1 μm disc and Nap-B1 as a suspension for 3 minutes

Between each step, the samples were washed in water and Zalo, rinsed in alcohol, and dried with a hairdryer. The final step of the metallographic sample preparation was an OSP polishing step, using an oxide polishing disc, an OP-S suspension for 1 minute, providing an oxide etching solution for a better surface finish.

Figure 19: Shows the Struers machine used for polishing the samples [12].

3.3 Casting

Amount of aluminium, alloying elements and observations made during casting can be found in Appendix B.

3.4 Analysis

3.4.1 Scanning Electron Microscope

For the thesis, a Scanning Electron Microscope (SEM) was used to investigate the intermetallic phases in the slow cooled (SC) samples. This was done mainly on a Zeiss Supra 55VP microscope, as shown in figure 20. All the samples were re-polished with a 0,1 μm oxide polish solution (OPS), cleaned with alcohol and dried before loading in the SEM.

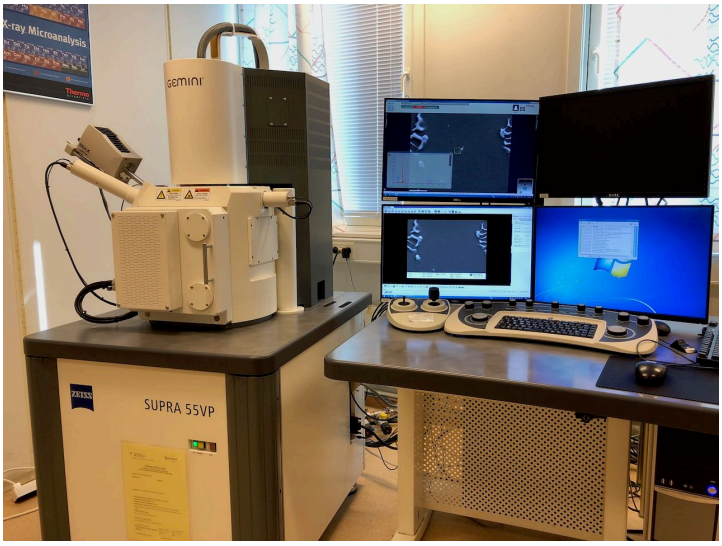

Figure 20: The SEM used to conduct the trials, a Zeiss Supra 55VP.

Energy-dispersive X-ray spectroscopy (EDS) was done on areas and spots of all the slow cooled samples. For EDS, the following parameters were used; Working distance: 10 mm, Beam strength: 20 kV, aperture: 120 µm and scan time: 50 s. The spectres were analyzed on the EDAX TEAM^{TM} EDS System software.

3.4.2 Conductivity

A GE AutoSigma 3000 hand-held electrical conductivity meter was used to measure the samples. The samples were polished with a 400 grit sanding disc. They were then cleaned with alcohol and dried. Five measurements were taken for each RSD sample on a grid of set locations of the cross-sectional area of the sample.

Figure 21: The apparatus used to take conductivity measurements.

3.4.3 Spark test

To quantify the dissolution of the alloying elements, samples were sent to Hydro's lab in Karmøy for spark test analysis. A thin cross-sectional disc was cut from one rapid solidified disc from each cast. The samples were polished with a 400 grit sanding disc. Five tests were done on each sample.

3.4.4 Tensile testing

To determine the mechanical properties of the different castings, tensile tests were performed with the machined samples. The samples had a circular diameter of 6,00 mm, and the production drawing and machined sample can be seen in figure 22.

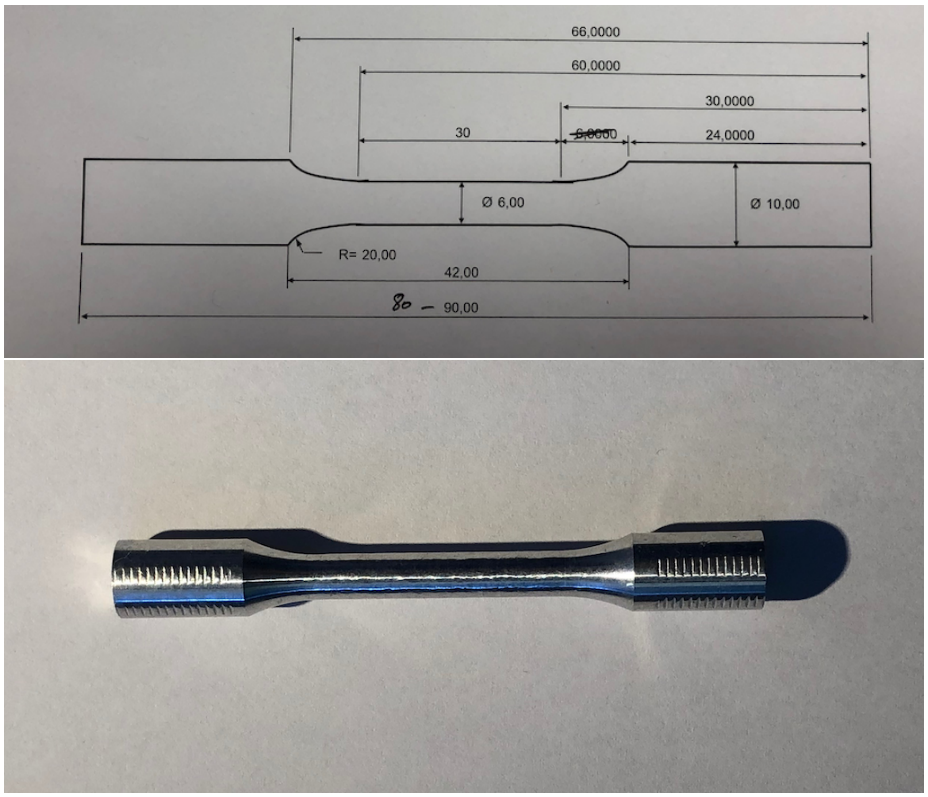

Figure 22: Template for machining and finished machined sample are shown.

As the tensile testing device, an "Instron 5982" floor model was used to conduct the tests and is shown in figure 23. The samples were mounted in the machine and stretched with a constant speed of $5\frac{\mathrm{mm}}{\mathrm{min}}$ until failure. The machine's software, Bluehill ®, was used to measure the forces and automatically calculated the yield strength, tensile strength, elongation, and other parameters of each sample. A total of five samples from each cast was used to get a statistical result.

Figure 23: The Instron 5982 machine used to perform tensile tests.

4 Results and discussion

4.1 Aluminium alloy 3103

4.1.1 Spark test

Spark testing was done to determine the content of the alloying elements in each sample. In table 8, one can see how the actual chemical content in the nom% 3103 samples deviates from the targeted values that were added in the crucibles. In table 9, this is shown for 150% Fe and Mn content, and in table 10, this is shown for 200% Fe and Mn content.

Table 8: Spark test results showing chemical content for nominal 3103 RSD samples, and their targeted values, where the targeted values are Hydros nom% and max%.

	301	**302**	**303**	**304**	**Target**
Al [wt%]	98,5	99,02	98,92	98,37	[98,04]
Fe [wt%]	0,59	0,36	0,28	0,78	[0,55-0,60]
Mn [wt%]	1,10	0,42	0,66	0,55	[1,0-1,08]
Si [wt%]	0,19	0,09	0,06	0,21	[0,1-0,15]
Mg [wt%]	0,01	0,01	0,02	0,00	[0,0-0,03]
Cu [wt%]	0,01	0,01	0,01	0,01	[0,0-0,03]
Cr [wt%]	0,01	0,01	0,01	0,01	[0,0-0,03]
Ni [wt%]	0,01	0,01	0,01	0,01	[0,0-0,1]
Zn [wt%]	0,02	0,03	0,02	0,02	[0,0-0,03]
Ti [wt%]	0,01	0,00	0,00	0,00	[0,0-0,02]

The measured values match the targeted values for most alloying elements. Significant variation of the manganese content, as seen in table 8, was observed. This might be to the use of 20wt% Mn - 80wt% Al waffles, where the manganese dissolved only to some extent when added in the hot metal bath (302, 303, 304). For sample 301 the Mn was added cold, before the heating and melting stages and it had therefore more time to dissolve. When the Mn was added in larger pieces (15-25 g), the undissolved Mn was found at the bottom of the crucible. Nevertheless, when the Mn was added in smaller pieces (1-15 g), it would float to the dross layer of the melt, not wet and interact with the alloy at all.

Table 9: Spark test results showing chemical content for the 150% Fe and Mn content of the 3103 RSD samples, and their targeted values for the chemical composition given by Hydro with nom% and max%.

	311	312	313	314	Target
Al [wt%]	97,46	97,12	97,28	98,14	[97,08]
Fe [wt%]	0,87	1,03	1,11	0,52	[0,83-0,90]
Mn [wt%]	1,30	1,55	1,28	1,23	[1,50-1,54]
Si [wt%]	0,21	0,20	0,23	0,05	[0,10-0,15]
Mg [wt%]	0,00	0,01	0,01	0,00	[0,0-0,03]
Cu [wt%]	0,01	0,01	0,01	0,01	[0,0-0,1]
Cr [wt%]	0,06	0,00	0,01	0,00	[0,0-0,03]
Ni [wt%]	0,03	0,01	0,01	0,00	[0,0-0,01]
Zn [wt%]	0,02	0,03	0,03	0,03	[0,0-0,03]
Ti [wt%]	0,00	0,00	0,00	0,00	[0,0-0,02]

For the chemical composition of the 150% Fe and Mn samples, as shown in table 9, the Mn was heated to 600°C before added to the Al-melt. This was done to ensure dissolving the Mn, as noticeable in the table. For cast 314 the new Mn with flux received from Hydro was used. This source of Mn was much easier to work with and dissolved quicker. The Mn briquettes not dissolving match the findings of T. Carlberg and G. Razaz that studied the dissolution properties of Mn in molten aluminium. They found that the Mn with flux dissolved quicker and to a greater extent than other Mn sources [8].

The spark test result from the samples containing 200 wt% Fe and Mn had large gaps between the different samples, 321, 322, 323, and 324. This can be seen in table 10. Sample 321 had almost no reading on Mn or Si, however the Fe reading was higher than the target. All Si readings matched the target.

Table 10: Shows real chemical content for 200% Fe and Mn content 3103 RSD samples, and their targeted values, where the targeted values are Hydros nom% and max%.

	321	322	323	324	Target
Al [wt%]	98,49	97,64	97,32	97,27	[96,43]
Fe [wt%]	1,33	0,86	1,42	0,96	[1,01-1,2]
Mn [wt%]	0,01	1,22	1,11	1,54	[2,00-2,16]
Si [wt%]	0,10	0,21	0,09	0,16	[0,1-0,15]
Mg [wt%]	0,01	0,01	0,00	0,00	[0,0-0,03]
Cu [wt%]	0,01	0,01	0,01	0,01	[0,0-0,1]
Cr [wt%]	0,01	0,01	0,01	0,01	[0,0-0,03]
Ni [wt%]	0,01	0,01	0,00	0,00	[0,0-0,01]
Zn [wt%]	0,02	0,03	0,03	0,03	[0,0-0,03]
Ti [wt%]	0,00	0,00	0,00	0,00	[0,0-0,02]

A graphic display of the spark test tables can be seen in figure 24, with the targeted Fe and Mn values added.

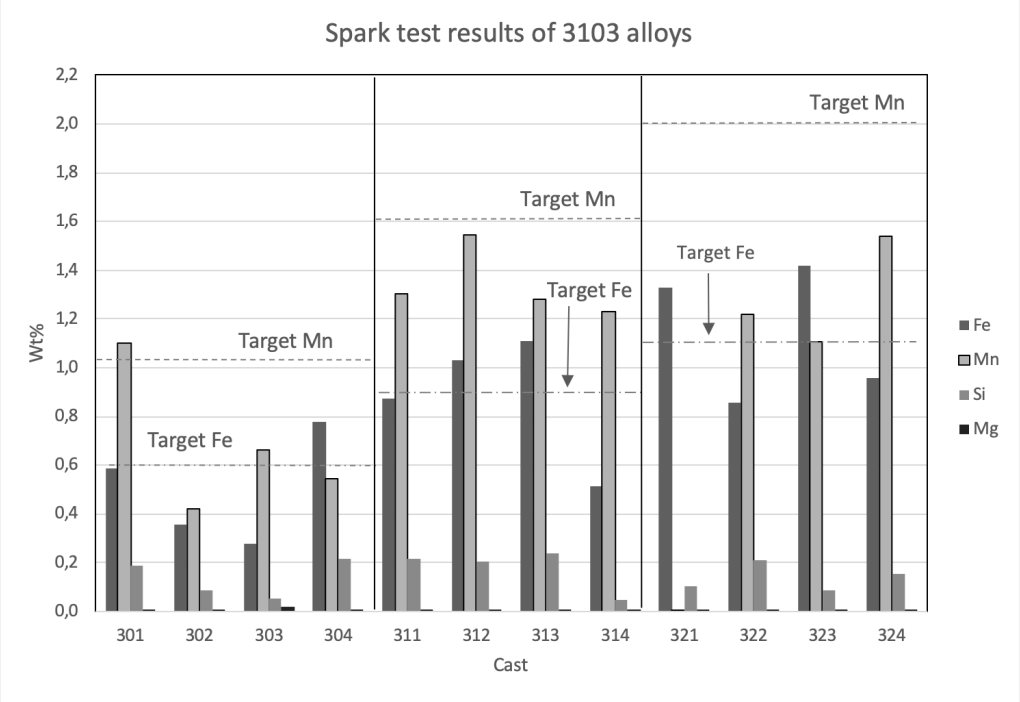

Figure 24: The graph shows the wt% for Fe, Mn, Si and Mg in the different 3103 casts. The target values of Fe and Mn for the different casts are visualized by the stippled lines.

4.1.2 Conductivity

The conductivity of a material depends on the number of impurities the material contains, *e.g.* grain boundaries and intermetallic phases. A perfect crystal will have the highest conductivity. Larger quantities of intermetallic phases would, therefore, decrease the conductivity of the material. Conductivity measurements from the different 3103 casts can be observed in table 11.

Table 11: Conductivity measurements done on the 3103 rapid solidifies samples. Five spots were taken per sample [%IACS].

	1	2	3	4	5	Average
301	30,3	30,1	30,2	30,3	30,1	**30,20**
302	41,1	41,1	41,1	40,9	41,2	**41,08**
303	35,5	35,5	35,5	35,2	35,5	**35,44**
304	37,9	37,8	37,8	37,7	37,8	**37,80**
311	29,0	29,1	29,1	29,2	29,1	**29,10**
312	29,2	29,4	29,1	29,2	29,2	**29,22**
313	31,3	30,8	32,0	31,9	31,7	**31,54**
314	29,2	29,1	29,0	29,3	29,2	**29,16**
321	55,9	55,7	55,7	55,6	55,5	**55,68**
322	30,7	30,5	30,6	30,5	30,7	**30,60**
323	34,4	34,4	34,4	34,2	34,6	**34,40**
324	29,2	29,3	29,2	29,3	29,3	**29,26**

The average values from each cast is shown in figure 25. Here, the %IACS value for 99,99 wt% is also shown for comparison.

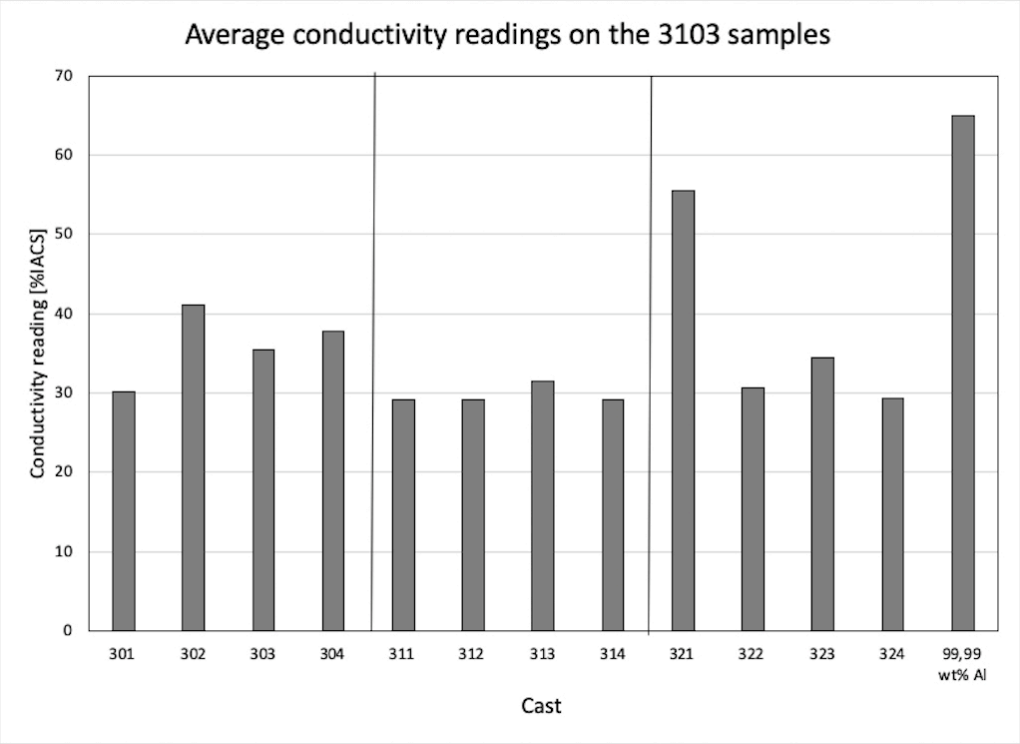

Figure 25: Average conductivity of the samples from 3103 rapid solidified. There is a slight decreasing trend from the nominal (30X) to the 150% (31x) [%IACS].

When looking at the conductivity readings from the nominal 3103 samples, one can see that the 301 sample has a lower average reading compared to the other samples from this set of parallel trials. When further looking at the microstructure, as shown in figure 28 page 38, it can be seen that there are more precipitations in the aluminium. These precipitations can hinder the flow of electrons in the material, increasing the average current path length and reducing the conductivity of the material.

As seen in table 11, the 150 wt% samples have the lowest average readings, and these are also the samples containing the most intermetallic precipitations, indicating that these phases could lead to bad conductivity. The rapid solidified sample from 313 has the highest average conductivity in this parallel, and is also the sample containing the least of these intermetallic precipitations, as can be seen in figure 32 page 43.

When looking at the conductivity measurements from the 200 wt% Fe and Mn samples, e.g. 322, 323, and 324, they show approximately similar average readings, while 321 has a much higher average conductivity. The microstructure from the sample 321 appears completely different when comparing with the other 3103 samples with 200 wt% Fe and Mn, and this can be seen in figure 35 page 47. Samples from 322, 323, and 324 contain different intermetallic precipitations, indicating that these phases can reduce/lower the

conductivity of aluminium.

Excluding single extreme values, the average conductivity readings are dropping with the increase in wt% of alloying elements. When the content of the alloying element increase, the content of Al decrease, indicating less wt% Al. From the conductivity measurements, it can be seen that the samples Nr. 302 and 321 have higher readings when comparing them to the rest of the samples. When comparing these values with those from the spark test in table 8 and 9, the skilled reader can see that the samples Nr. 302 and 321 have a higher concentration of Al and a lower amount of alloying elements than the target concentration of the specific alloy. This indicates that the alloying elements have not been mixed with the Al-melt, but did also not dissolve completely. Another possibility is the loss of alloying material to the slag phase, which has not been the focus of this thesis work.

4.1.3 Morphology and intermetallic phases

For studying the morphology of the different samples, the SEM pictures from the slow cooled (SC) samples were used. To compare the RSD samples with SC samples, light microscope image (LMI) of the RSD samples were taken.

EDS analysis of the different intermetallic phases and base matrix showed a large variation in the chemical composition. The reason for this has been directed towards the Al-matrix surrounding the phases of interest, giving inaccurate readings with the EDS in regards to the composition.

It has been observed from the pictures, and EDS results, that an increase in Mn concentrations/levels within the intermetallic phases can lead to a more block-like morphology. For samples with almost no Mn readings, the intermetallic phases appear almost like painted on with a brush.

The meta-stable primary $Al_6(Fe, Mn)$ intermetallic phases are easily distinguishable as it appears as a block like structure/form with a hole in the middle. The EDS results from this phase also show a consistent Mn/Fe-ratio < 1. The phase contained around 0,4 to 0,5 Wt% Si. Most of the $Al_6(Fe, Mn)$ intermetallic phase were found in the samples with 150% and 200% Mn and Fe.

Notes from nominal 3103, Al-0,6Fe-1,08Mn-0,15Si

301 - Al-0,6Fe-1,08Mn-0,15Si

The rapid solidified sample from the 301 cast showed a chemical composition of Al-0,59Fe-1,10Mn-0,19Si (table 8 page 30). This is in good correlation with the target value. The cast was not stirred with an engine as it broke down during the trial. This was compensated with increasing the holding time to 40 min. The average conductivity of the rapid solidified sample was found to be 30,20 %IACS (table 11 page 32).

There is not much difference in the rapid solidified and slow cooled sample. There appears to be the same type of intermetallic phases in both samples. The intermetallic phase has a script-like morphology that looks similar to the α-$Al_{15}(Fe, Mn)_3Si_2$.
EDS analysis was conducted on two intermetallic phases, as seen in figure 106 page 109,

that appeared to be a bulky α-phase. Both analyses show a $\frac{Mn}{Fe}$-ratio of 0,5. Reading of spot 1 have a higher amount of alloying elements than spot 2, where the respective values are Al-12,22Fe-6,29Mn-5,08Si against Al-8,67Fe-4,45Mn-3,79. This might be due to the spot 1 being a larger intermetallic phase giving better readings to the EDS probe than the smaller phase in spot 2. These phases can be observed in figure 81 page 96.

The tensile test results show similar yield- and tensile strength results, but a large variation in the elongation (figure. 59 in the appendix)

302 - Al-0,6Fe-1,08Mn-0,15Si

The rapid solidified sample cast form the 302 showed a chemical composition of Al-0,36Fe-0,42Mn-0,09Si (table 8). This is far below the target composition, as illustrated in figure 24. The average conductivity of the rapid solidified sample is 41,08 %IACS (table 11 page 32), which is the highest in the parallel.

The rapid solidified and slow cooled sample do not appear to have a large variation in the morphology.
The intermetallic phases have a script like structure, with bulky parts, as seen in figure 28 page 38. The EDS analysis shows no readings of Si, which correlates with the obtained results from the spark test. These intermetallic phases are in the shape of small dots in the microstructure. The phase might be Al_3Fe with a solubility of Mn, or Al_6(Fe, Mn). Many of them have high readings of Fe, with the highest reading being 17,12 wt%, and $\frac{Mn}{Fe}$-ratio of 0,2. The intermetallic phases with the bulkiest forms are also the ones with the highest Mn readings; this result matches the literature where this effect already is observed. This can be seen in figure 107 page 109 spot 243 and 244, where the Mn readings are 3,74 wt% and 3,64 wt% respectively. These spots have a $\frac{Mn}{Fe}$-ratio of 0,2 and 0,3.

The tensile test results show yield strength of 44 Mpa, tensile strength of 118,8 Mpa, but a large variation in the elongation (figure. 60 in the appendix)

303 - Al-0,6Fe-1,08Mn-0,15Si

The rapid solidified cast 303 sample showed a chemical composition of Al-0,28Fe-0,66Mn-0,06Si (table 8). This is far below the target composition, as illustrated in figure 24. The Mn/Fe-ratio is not that far of target levels. The average conductivity of the rapid solidified sample 35,44 is %IACS (table 11).

There appear to be the same types of intermetallic phases in both rapid solidified and slow cooled samples. The precipitations form along the grain boundaries in thin sections. EDS analysis of the phase showed a composition of Al-7,77Fe-1,72Mn-0,71Si, as seen in figure 108.

In figure 26 from the cast 303, the slow cooled sample shows that there is a noticeable difference in grain size between the two. There appear to be areas with up-concentrated amounts of intermetallic precipitations, as shown in figure 27. This might be due to poor distribution of additions in the melt or primary-precipitation.

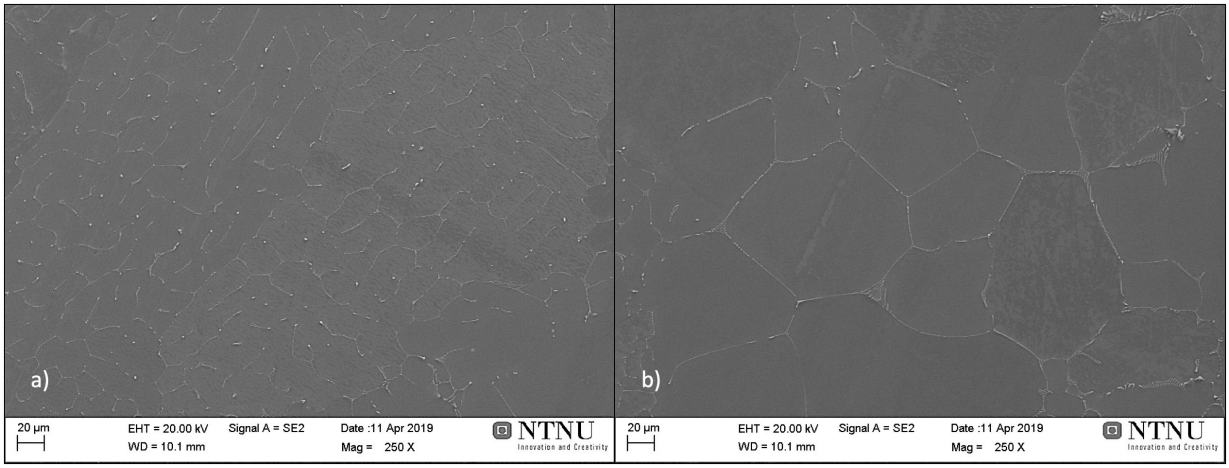

Figure 26: SEM picture of the difference in grain size in the cast 303 slow cooled sample.

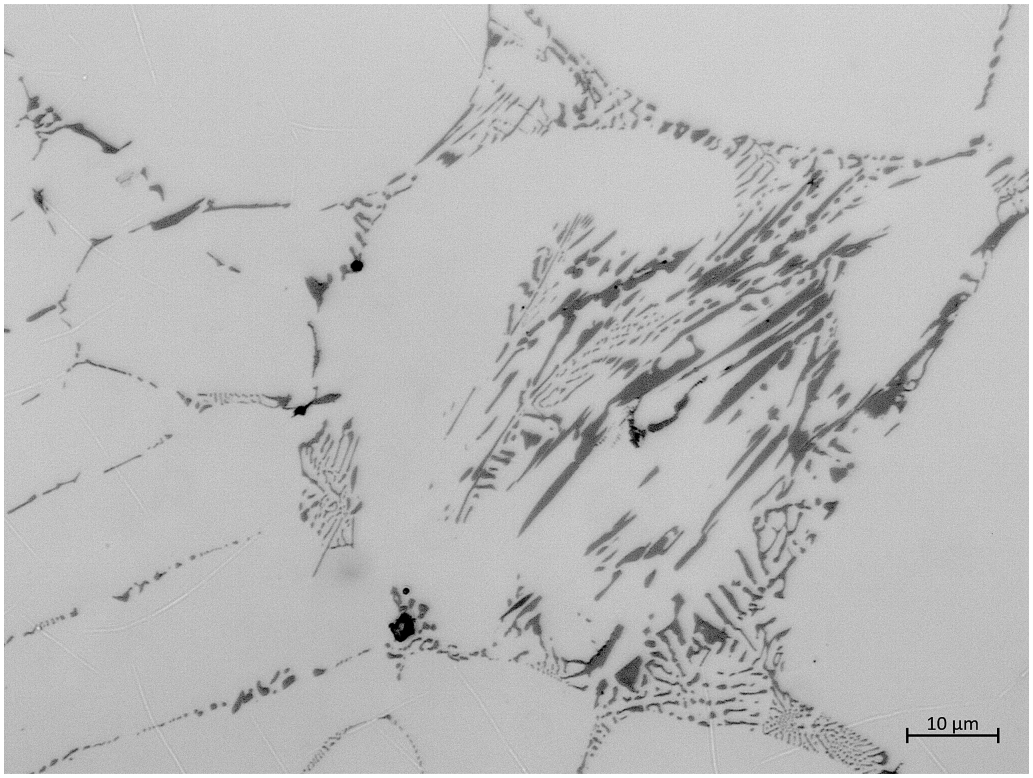

Figure 27: Large intermetallic structure in the cast 303 slow cooled sample.

The tensile test result shows similar yield strength of 40,4 Mpa, a tensile strength of 105,4 Mpa and 11,28% elongation (figure. 61 in the appendix).

304 - Al-0,6Fe-1,08Mn-0,15Si

The rapid solidified cast 304 sample showed a chemical composition of Al-0,78Fe-0,55Mn-0,21Si (table 8). This is far below the target composition, as illustrated in figure 24. The

Mn/Fe-ratio is lower than the target. The average conductivity of the rapid solidified sample is 37,44%IACS (table 11).

There does not seem to be a large difference in morphology between the rapid solidified and slow cooled sample. Both having script like intermetallic phases. EDS analysis was done in two different areas, as seen in figure 109. A small, bulky intermetallic was measured to contain Al-12,14Fe-2,93Mn-0,88Si. This can be a α- or Al_6(Fe, Mn)-phase. In the second area, a grain-like intermetallic phase which is approximately 5 μm long can be seen. It contained 12,16 wt% Fe and 2,19 wt% Mn, giving it a $\frac{Mn}{Fe}$-ratio of 0,2, making it a possible Al_6(Fe, Mn) intermetallic phase. It has a bulky appearance and smears out to a script-like phase.

Due to the lack of time/missing samples, the tensile tests for the sample series 304 were not conducted.

Summary 3103 nominal composition - Al-0,6Fe-1,08Mn-0,15Si

On 301 and 302 almost all the precipitations seem to lie along the grain boundaries, while larger amounts of precipitations do not follow the grain-boundaries on the 303 and 304 castings. The average size of the intermetallic phases seems to be smaller on 302, 303 and 304 than on 301. This may be a result of the longer diffusion time the alloying elements have when added in cold and promote larger intermetallic phases rather than the alloying elements mixing with the Al-matrix.

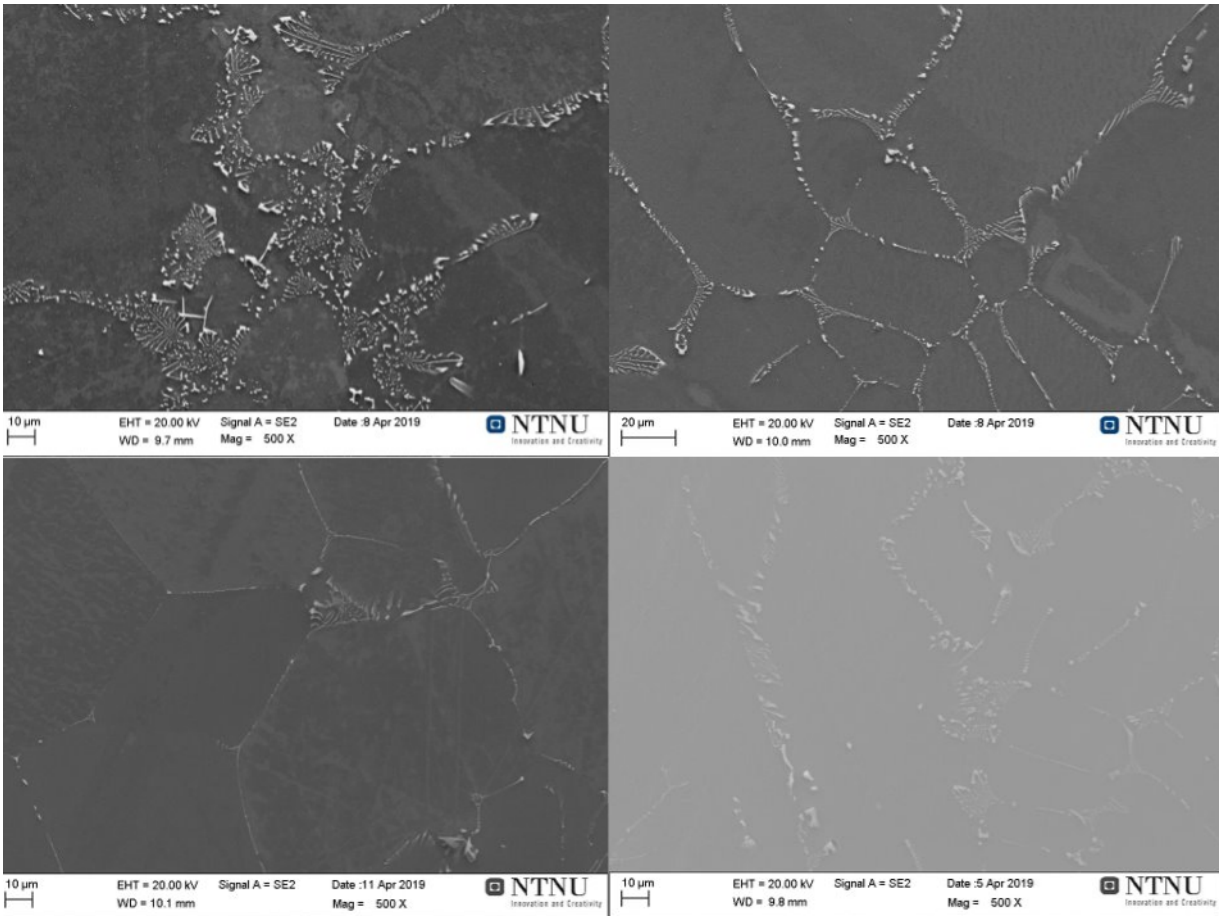

Figure 28: SEM pictures from the parallels on nominal 3103 samples. Top left shows sample 301, top right is 302, bottom left is 303, and bottom right is 304.

Notes from 150% 3103, Al-0,9Fe-1,68Mn-0,15Si

311 - Al-0,9Fe-1,68Mn-0,15Si

The rapid solidified cast 311 sample showed a chemical composition of Al-0,87Fe-1,30Mn-0,21Si (table 8). This is a bit below the target values, as illustrated in figure 24. The average conductivity of the rapid solidified sample was 29,10%IACS (table 11).

In both the rapid solidified and slow cooled sample, there is a large amount of what appears to be Al_6(Fe, Mn). There might be a slight increase in the average size of the primary-Al_6(Fe, Mn) in the slow cooled samples when compared to the rapid solidified. Figure 29 shows a large needle-like phase that was found in the slow cooled sample.

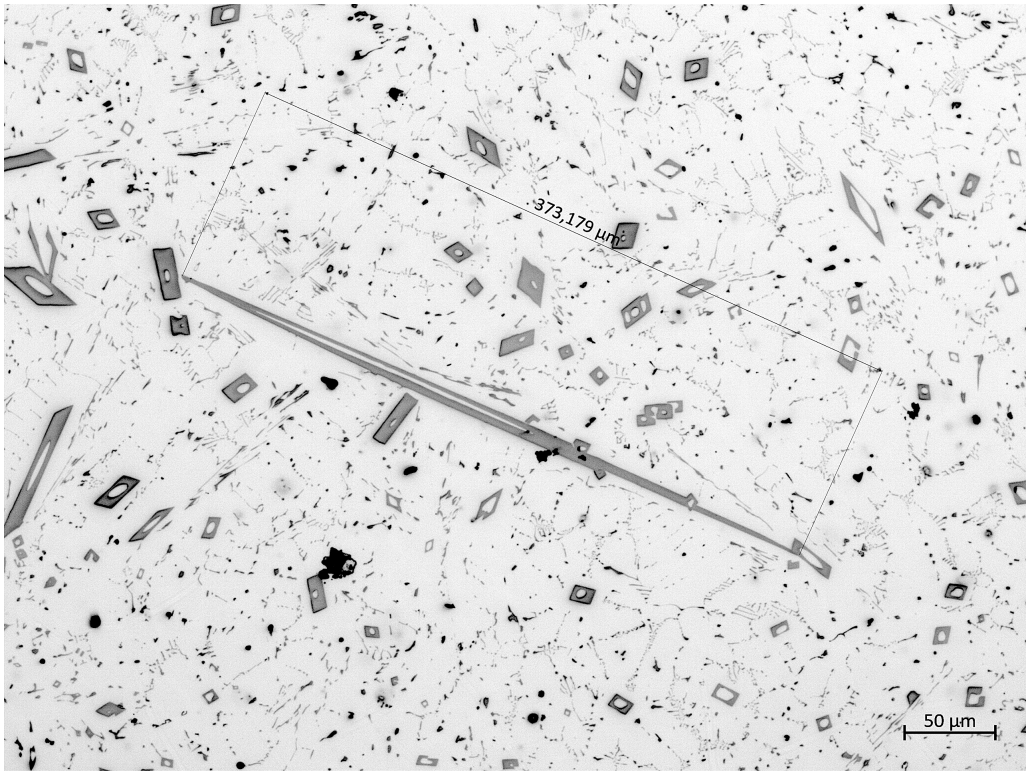

Figure 29: Possible Al_6(Fe, Mn) intermetallic phases in the cast 311 slow cooled sample. Similar needles were found in several of the 150% and 200% Fe and Mn 3103 alloys.

Several of these needles were found in the different samples of this parallel. EDS analysis on some of the needles showed the same composition as what is assumed is the primary-Al_6(Fe, Mn), as seen in figure 30.

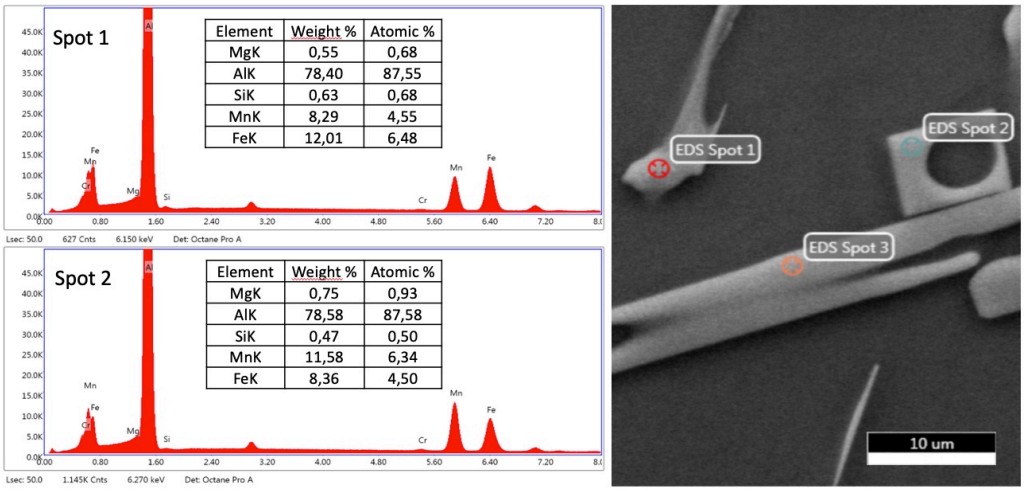

Figure 30: EDS analysis of the intermetallic precipitations found in the cast 311 slow cooled sample. Spot 3 has similar readings as spot 2.

EDS analysis shows the cross-sectional area of a needle structure, Al-8,36Fe-11,58Mn-0,47Si-0,75Mg, as shown in figure 30. This appears to be primary-Al_6(Fe, Mn) with a solubility of low levels of Si and Mg (~ 0,5wt%). Cracking was observed in several of the primary-Al_6(Fe, Mn) precipitations, as shown in figure 31.

There were also found several other smaller precipitations of intermetallic phases. These generally had an $\frac{Mn}{Fe}$-ratio < 1. The morphology is bulky, and this together with the stoichiometric coefficients could indicate this as eutectic-Al_6(Fe, Mn).

The tensile test results show a yield strength of 36,4 Mpa, a tensile strength of 95 Mpa, and an average elongation of 8,25% (figure. 60 in the appendix).

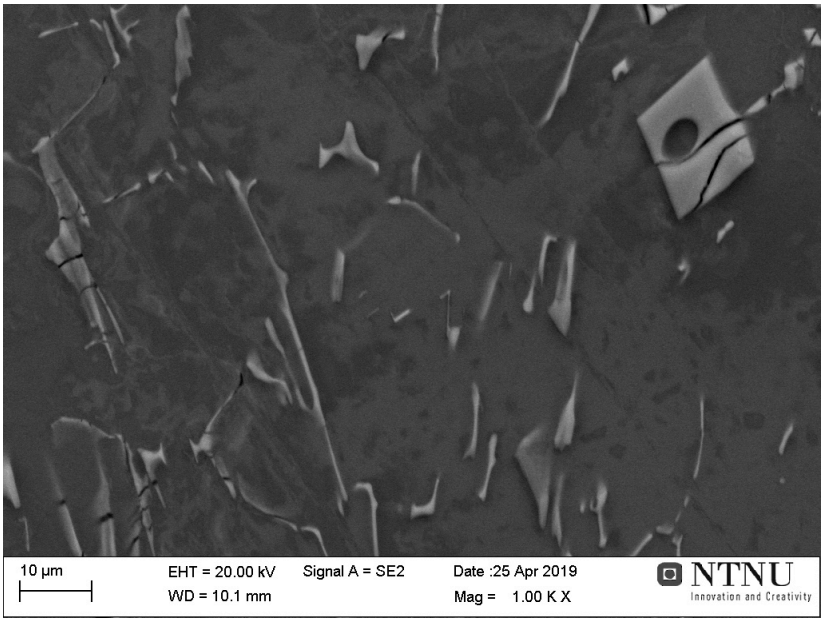

Figure 31: Cracking of the primary-Al_6(Fe, Mn) intermetallic phases in the cast 311 slow cooled sample

312 - Al-0,9Fe-1,68Mn-0,15Si

The rapid solidified cast 312 sample showed a chemical composition of Al-1,03Fe-1,55Mn-0,20Si (table 8). This is a bit above on the Fe and below on Mn compared to the target values as illustrated in figure 24. The average conductivity of the rapid solidified sample is 29,22 %IACS (table 11).

As seen from the SEM-picture and LMI in figure 87, page 99, there are no visible grain boundaries, and all the intermetallic phases grow in the Al-matrix without much order. The intermetallic phase seems to form as large needles, or as Chinese-script around the needle formations. The chemical composition of three needles were taken (figure. 56), showing a composition of spot 1) Al-9,49Fe-13,47Mn-0,48Si-0,45Mg and spot 2) Al-9,31Fe-13,34Mn-0,44Si-0,46Mg. Based on the EDS and morphology, they seem to be Al_6(Fe, Mn), and diagonally the needles measure 10 µm.

The tensile test was not done for the cast.

313 - Al-0,9Fe-1,68Mn-0,15Si

The rapid solidified cast 311 sample showed a chemical composition of Al-1,11Fe-1,28Mn-0,23Si (table 8). This is a bit below the target values, as illustrated in figure 24. The average conductivity of the rapid solidified sample is 31,54 %IACS (table 11).

The 313 microstructure is similar to the rest of the parallel. There are no visible grain-boundaries, and the intermetallic phases form as large needles or Chinese script.
EDS analysis, as seen in figure 112, page 112, of the script like intermetallic precipitations showed a composition of Al-11,51Fe-2,30Mn-4,32Si-0,73Mg, giving a $\frac{Mn}{Fe}$-ratio of 0,20. The length of the precipitation is 15µm.

The tensile test results show a yield strength of 36,4 Mpa, a tensile strength of 95 Mpa, and an average elongation of 8,25% (figure. 62 in the appendix).

314 - Al-0,9Fe-1,68Mn-0,15Si

The rapid solidified cast 314 sample showed a chemical composition of Al-0,52Fe-1,23Mn-0,05Si (table 8). This is below the target values, as illustrated in figure 24. The average conductivity of the rapid solidified sample is 29,16 %IACS (table 11).

The 314 microstructure is interesting compared to the other parallels with the same wt%. The same primary-Al_6(Fe, Mn) intermetallic phases can be observed, but around the phase is only a pure Al-matrix. There are no visible precipitations around the needles, and the size of them vary. Many of the needles are directional, which can indicate a direction of solidification. The largest needle observed measures ~ 80 μm across.

The morphology of the needles is the same as in the previous parallels, making this phase a probable Al_6(Fe, Mn) intermetallic precipitation. The size of the smaller script-like intermetallic phases varies from 1-8 μm.

EDS done on two small needles can be seen in 113, page 112, with different morphologies, where spot 1 is W-shaped, and spot 2 is square-shaped. The composition gathered from spot 1 is Al-15,91Fe-2,51Mn-0,59Si-0,52Mg and small amounts of Ni. The analysis from spot 2 gives Al-17,84Fe-3,79Mn-0,51Si-0,57Mg. These are possible Al_6(Fe, Mn) or $Al_{15}(Fe, Mn)_3Si_2$ intermetallic phases.

The tensile test results show a yield strength of 42,6 Mpa, a tensile strength of 103,6 Mpa, and an average elongation of 11,01% (figure. 63 in the appendix).

Summary 3103 150% - Al-0,9Fe-1,68Mn-0,15Si

The microstructure of 312 and 313 are very similar, but there seem to be more needles in the 312 structure, and more Chinese script in the sample 313. The 311 microstructure is more "messy", containing a lesser degree of order. The Chinese script seen in 311 seems to form in larger clusters than in the other samples. The needles in 314 lie in a pure Al-matrix.

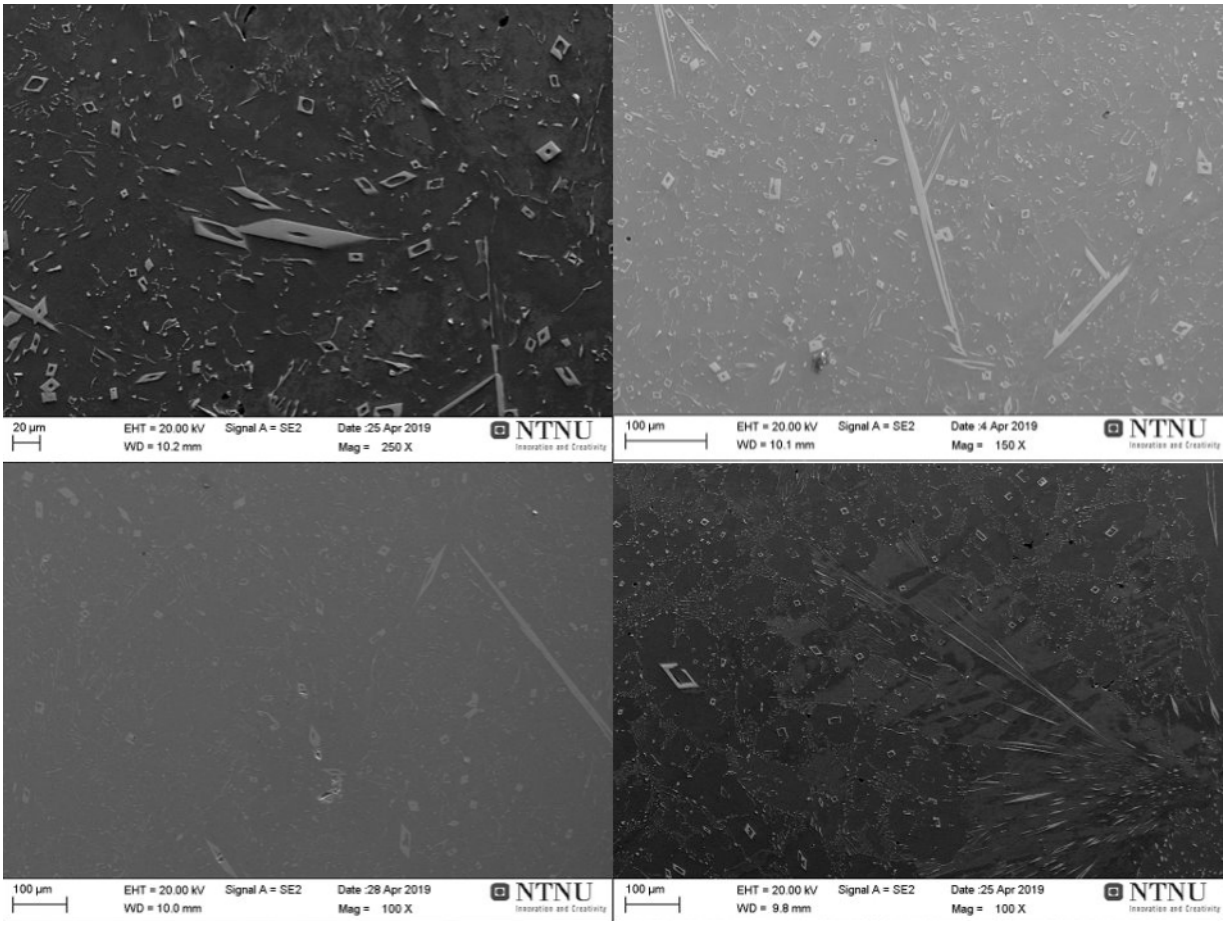

Figure 32: SEM pictures from the 3103 parallels containing 150 wt% Fe and Mn. Top left shows sample 311, top right is 312, bottom left is 313, and bottom right is 314.

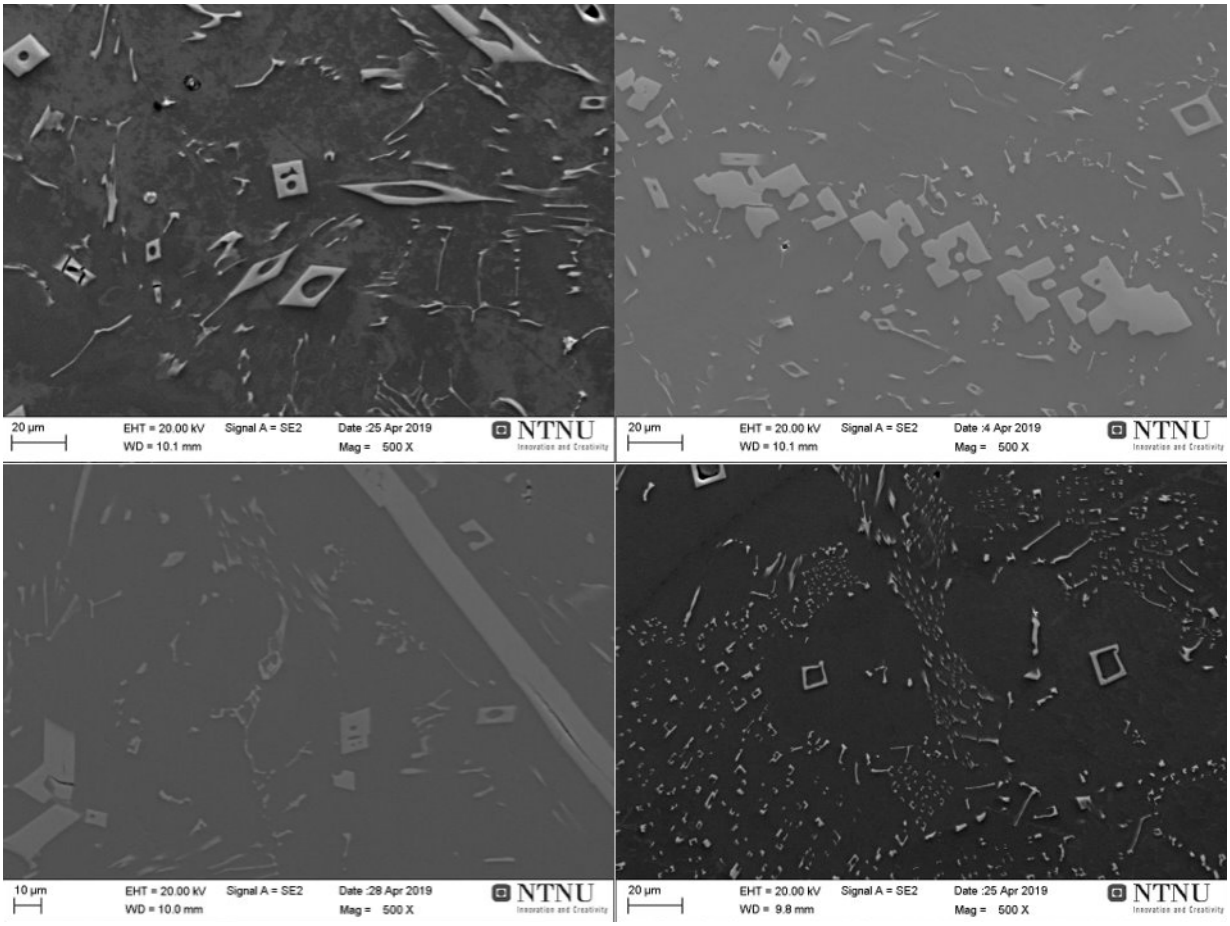

Figure 33: SEM pictures from the 3103 parallels containing 150 wt% Fe and Mn with a higher magnification than figure 32. Top left shows sample 311, top right is 312, bottom left is 313, and bottom right is 314.

Notes from 200% 3103, Al-1,2Fe-2,16Mn-0,15Si

321 - Al-1,2Fe-2,16Mn-0,15Si

The rapid solidified cast 321 sample showed a chemical composition of Al-1,33Fe-0,01Mn-0,10Si (table 10). There is almost no Mn in the sample, and Fe is below the target values, as illustrated in figure 24. The average conductivity of the rapid solidified sample is 55,68 %IACS (table 11) and hereby the highest among the 3103 alloy series of this investigation. This is probably due to the low Mn levels in the cast

The morphology of these intermetallic phases looks like those observed in super-modified structure (figure 35). The same morphology appears on both sets of samples.
There is a large area of precipitations around the grains, where the precipitations are thin script-like lines or round-ish dots. Figure 114 page 113, shows EDS analysis of the precipitations, and that the round dots consist of Al-11,68Fe-2,09Si-0,90Mg, this is a possible α-Al_8Fe_2Si phase.

The tensile test results show a yield strength of 36,4 Mpa, a tensile strength of 95 Mpa, and an average elongation of 8,25% (figure. 64 in the appendix). The deviation of the different casts has been minimum for this set of samples.

322 - Al-1,2Fe-2,16Mn-0,15Si

The rapid solidified cast 314 sample showed a chemical composition of Al-0,86Fe-1,22Mn-0,21Si(table 10). The values are far below the target values, as illustrated in figure 24. The average conductivity of the rapid solidified sample is 30,66 % IACS (table 11).

There was a large difference in the slow cooled and the rapid solidified sample. Both sets of samples show primary-Al_6(Fe, Mn), whereas the slow cooled sample shows this phase to a much higher degree when comparing it to the RSD sample. This can be observed in figure 91, page 101.

The RSD samples show structures which appears to be small dots/spheres and lines around in the samples. An EDS analysis of similar precipitation on the slow cooled sample gives Al-7,69Fe-6,36Mn-0,56Si, as seen in figure 115. The $\frac{Mn}{Fe}$-ratio is lower than the primary-Al_6(Fe, Mn), while the Si wt% is the same. This might indicate that the phase changes its form/shape when the $\frac{Mn}{Fe}$-ratio < 1. The phase might also be eutectic Al_6(Fe, Mn) as shown in figure 6, page 10.

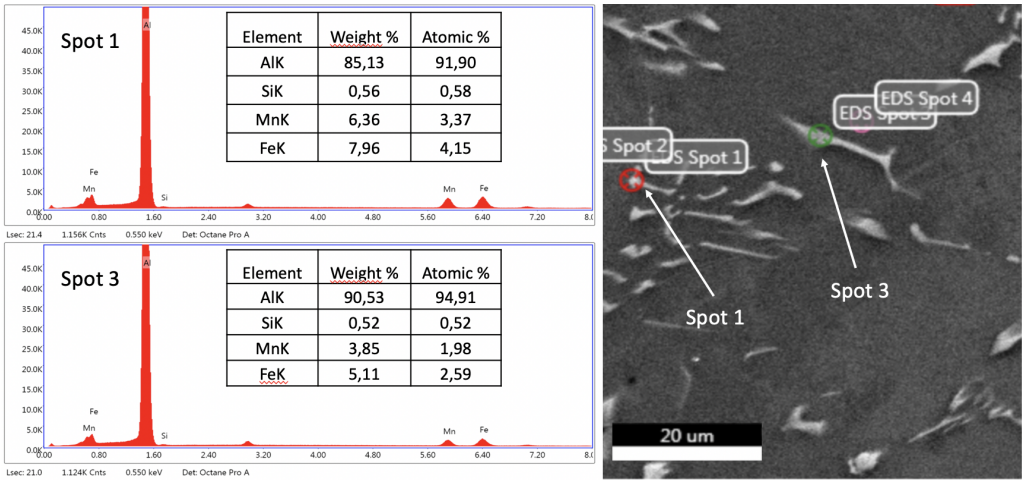

Figure 34: EDS analysis of the script-like intermetallic phase in the slow cooled Al-1,2Fe-2,16Mn-0,15Si sample (322).

The tensile test results show a yield strength of 44,2 Mpa, a tensile strength of 121,8 Mpa, and an average elongation of 7,68% (figure. 65 in the appendix). The different samples of this set show little deviation from one another.

323 - Al-1,2Fe-2,16Mn-0,15Si

The rapid solidified cast sample 323 showed a chemical composition of Al-1,42Fe-1,11Mn-0,09Si (table 10). The values are above for Fe, and below for Mn, the target values are illustrated in figure 24. The average conductivity of the rapid solidified sample is 34,40 %IACS (table 11).

Both the rapid solidified and slow cooled samples show large amounts of primary-Al_6(Fe, Mn). Both in the form of bigger needles but also in the script like form. The precipitations of the phase are bigger in the slow cooled sample when comparing it to the RSD sample, as seen in figure 92 on page 101.

The tensile test results show a yield strength of 36,4 Mpa, a tensile strength of 95 Mpa, and an average elongation of 8,25% (figure. 64 in the appendix). The different samples of this set show little deviation from one another.

324 - Al-1,2Fe-2,16Mn-0,15Si

The rapid solidified cast sample 324 showed a chemical composition of Al-0,96Fe-1,54Mn-0,16Si (table 10). The values are above for Fe, and below for Mn, the target values are illustrated in figure 24. The average conductivity of the rapid solidified sample is 29,26 %IACS (table 11).

SEM-pictures from figure 93 on page 102, show that sample 324 does have needle-like formations, and large precipitations of what can appear to be α-intermetallic phases are visible around the visible grains. EDS from a bulky part of the intermetallic identified the phase to consist of Al-9,13Fe-4,03Mn-5,77Si-0,79Mg, a possible α-$Al_{15}(Fe,Mn)_3Si_2$ phase.

Summary of 200wt% Fe and Mn 3103 - Al-1,2Fe-2,16Mn-0,15Si

There are large variations in the rapid solidified and slow cooled samples. The larger intermetallic seems to be of similar size in both samples, but the smaller precipitations in the samples change morphology.

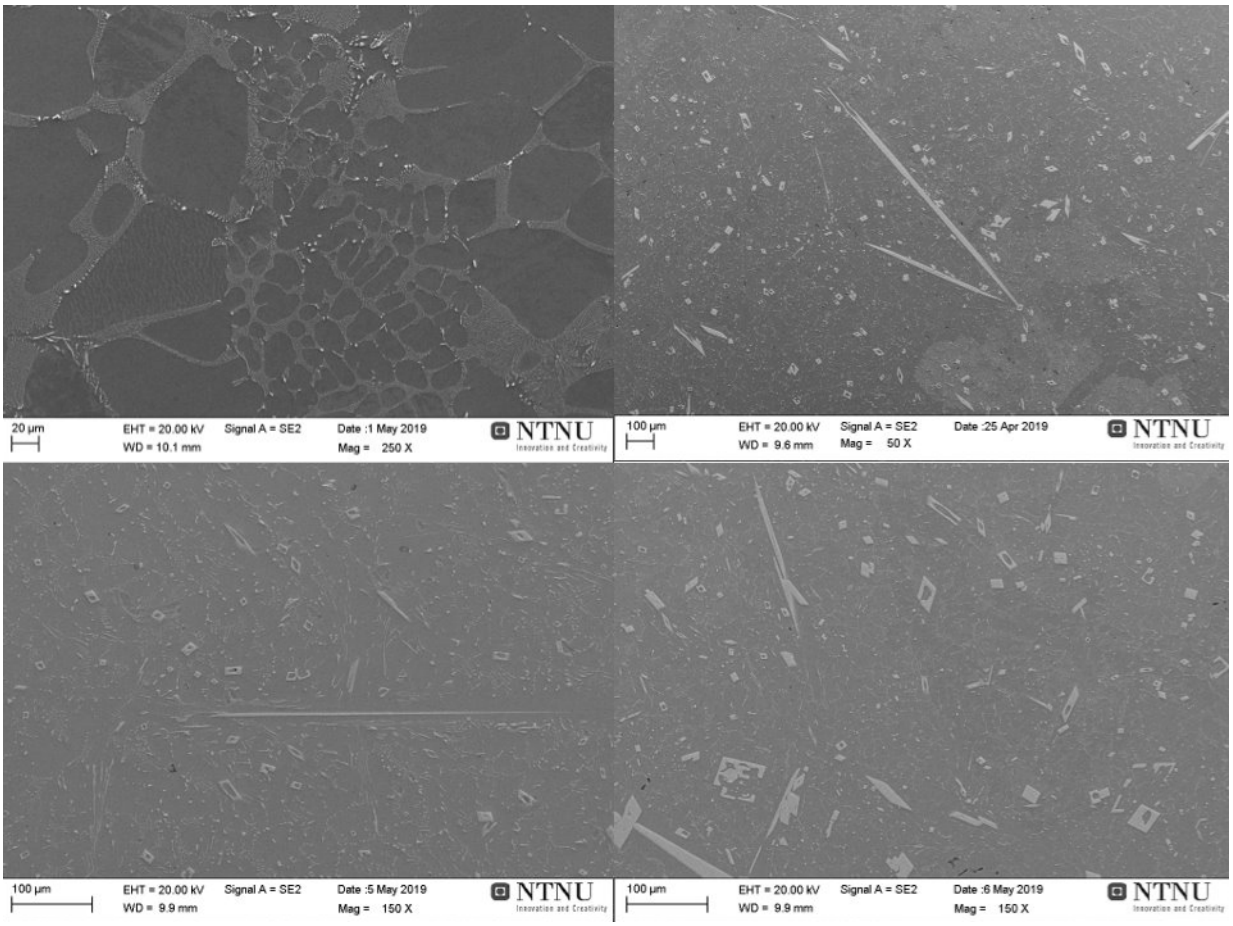

Figure 35: SEM pictures from the 3103 parallels containing 200 wt% Fe and Mn. Top left shows sample 321, top right is 322, bottom left is 323, and bottom right is 324.

4.1.4 Tensile testing 3103

All stress-strain curves can be found in Appendix A(figure 59-67), the average yield and tensile strengths of the 3103 casts can be found in figure 36.

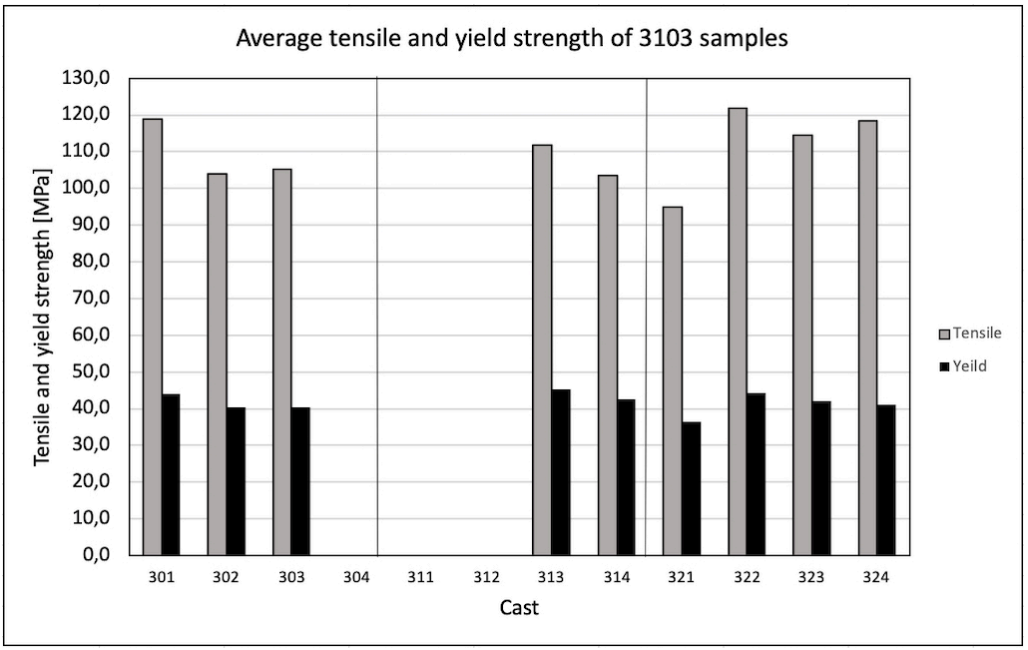

Figure 36: Shows the average yield and tensile strength from the 3103 casts. Five specimens were taken from each cast to get a representative result.

The tensile tests done on the 3103 alloy samples identified the alloy to be somewhat ductile. The stress-strain curves for the samples Nr. 301, 302, and 303 can be found in figure 59, 60, and 61.
For sample 301, the graph shows good consistency on σ_{TS} for specimen 1, 2, 3, and 5, while specimen 4 failed before the rest. This is most likely because of the formation of hard intermetallic phases, altering the behaviour of the ductile Al. Material parameters for the different specimens can be found in figure 59.

When comparing the obtained values from cast 301 and 303, with the highest and lowest values excluded. It was found that the average yield strength is 6,82% higher for the cast 301, the tensile strength is 12,91% higher, while the elongation was 18,6% higher for the cast 303. These findings would suggest sample 301 to be more brittle and less ductile than sample 303. When comparing the sample 301 against 302, the skilled reader can see that the yield- and tensile strength of sample 302 is lower than those of 301, making 301 the most brittle sample of the 3103 nominal samples.

Tensile testing for 304, 311, and 312 was not done, because the copper moulds arrived after those samples were cast. When lacking 2 of the 4 parallels from 150 wt% Fe and Mn, the remaining two are not as statistically relevant to compare, but the individual results are still interesting.

Even with 150 wt% Fe and Mn, the 314 casts stress-strain curve has a ductile behaviour. This can be seen in figure 63. The Average σ_y is 42,6 MPa, the average σ_{TS} is 103,6 MPa, while the average elongation is 11,01%. This is 67,2% longer than the average

elongation values from the 313 cast, which can be seen in figure 62. The 313 cast have similar σ_y and σ_{TS} as 314.

In the 200 wt% castings, which can be seen in figures 64, 65, 66, and 67, the 322 cast has the highest σ_y of 44,2 MPa. The lowest average σ_y is from the 321 cast, which is 36,4 MPa, a difference of +17,6%. The 322 cast also have the highest σ_{TS} =121,8 MPa, and 321 has the lowest of 95 MPa. A difference of +22%. The 321 cast has the highest average elongation of 8,25%, while 324 has the lowest average elongation of 5,98%, a difference of 27,6%.

Based on the acquired data, there is a slight difference in yield strength between the nom%, 150 wt%, and 200 wt% castings. Where the nom% castings have a 6,6% higher average σ_y than the 200 wt% castings, which have the lowest average. The opposite is true for the tensile strength, where the 200 wt% castings have an average σ_{TS} of 112,5 MPa, 4,3% higher than the 150 wt% castings average σ_{TS} of 107,7 MPa. The most significant difference between the castings is in the elongation. There is a 24,7% decrease in the average elongation between nom% and 200 wt%. The elongation in the nominal castings is 9,25% , while it is 7,0% for the 200 wt%. This indicates that the introduction of larger amounts of Fe and Mn to the Al matrix makes the alloy more brittle and less ductile.

4.1.5 Thermodynamic modeling 3103

For the calculations done with FactSage, the Al-Fe-Mn-Si system was chosen for modelling the 3103 phase diagrams. The levels of Si were kept constant at 0,15 wt%. In figure 37 the phase diagram for the nominal 3103 alloy can be seen. Here the Al-Mn diagram is modelled, with Fe = 0.6 wt% as a constant in the background. A reoccurring problem in the calculations was the existence of several binary and ternary products that, according to the literature, should not exist when at equilibrium, or phases that are only theoretically found. Some of these phases were located in the «pure solids» package from FactSage. Excluding the stable phases from the calculations, the software was showing liquid phases down to around 200 °C in the phase diagrams. It was concluded that the exclusion of packages from the calculations is not preferable, as it might hinder the program in calculating intermediate and stable phases. For these calculations, only the formation of the identifiable phases in the samples was interesting. Table 7 page 14 was used to correlate the validity of the different phases in the diagram.

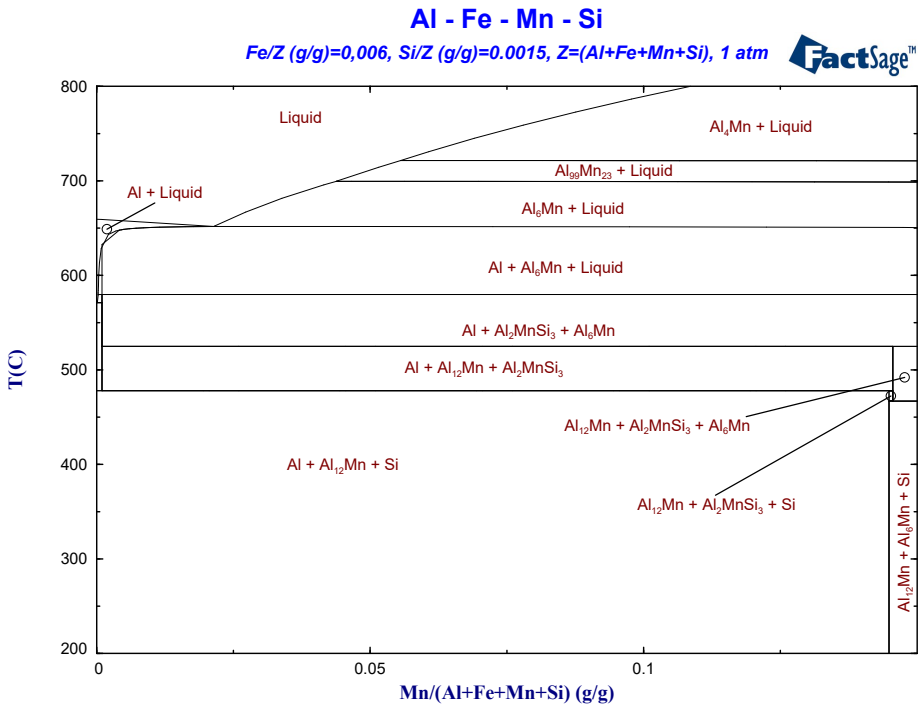

Figure 37: Showing the Al-Mn phase diagram with Fe and Si as constants in the background. The Al-rich corner up to 15 wt% Mn is shown.

The Al-Fe phase diagram was also modelled for the nominal 3103 alloy. This is shown in figure 38, where Mn is a constant in the background, Mn = 1.08 wt%.

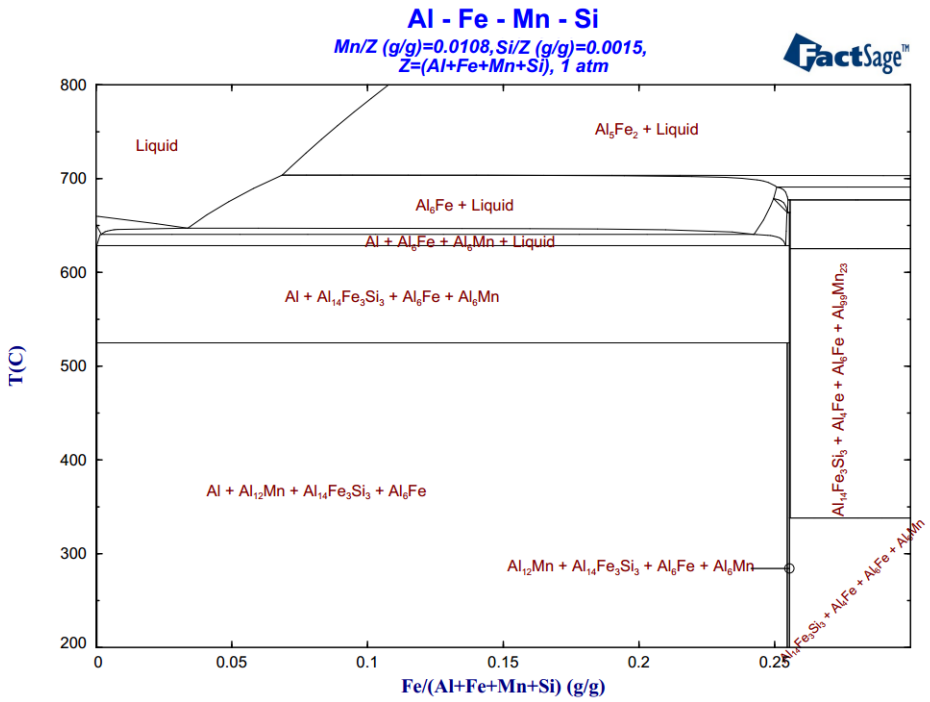

Figure 38: The Al-Fe phase diagram with Mn and Si as constants in the background. Showing the Al-rich corner up to 30 wt% Fe.

Due to the low solid solubility of Fe in Al, some phases start to form at very low wt%, figure 39 is a zoomed in version of 38, and it shows the formation of intermetallic phases close to the pure Al-corner.

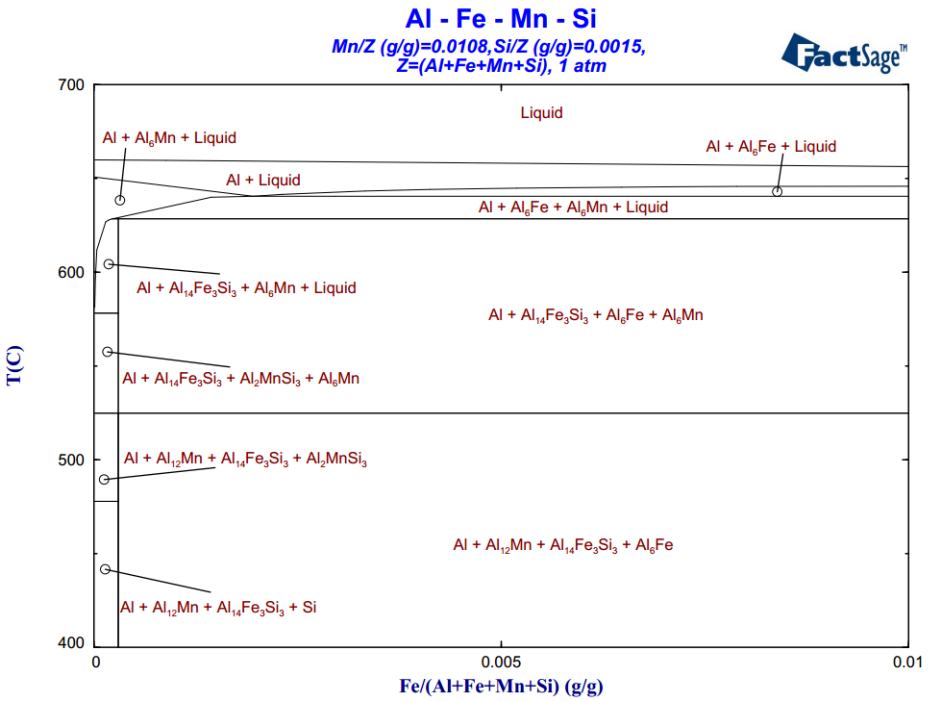

Figure 39: The Al-Fe phase diagram with Mn and Si as constants in the background. Showing the zoomed in version of figure 38, up to 1 wt% Fe.

4.2 Aluminium alloy 6082

4.2.1 Spark test

Table 12, 13, and 14 shows the result from the spark test analysis for the 6082 alloy. nom%, 150% and 200% respectively.

Table 12: Shows real chemical content for nominal 6082 RSD samples, and their targeted values, where the targeted values are Hydros nom% and max%.

	601	602	603	604	Target
Al [wt%]	98,81	97,5	97,64	97,36	[97,35]
Fe [wt%]	0,13	0,38	0,35	0,37	[0,22-0,24]
Mn [wt%]	0,02	0,45	0,36	0,46	[0,43-0,49]
Si [wt%]	0,45	0,92	0,97	1,02	[0,9-0,95]
Mg [wt%]	0,50	0,61	0,57	0,61	[0,65-0,68]
Cu [wt%]	0,03	0,05	0,04	0,05	[0,0-0,04]
Cr [wt%]	0,01	0,01	0,01	0,04	[0,12-0,15]
Zn [wt%]	0,04	0,04	0,05	0,05	[0,0-0,05]
Ti [wt%]	0,00	0,00	0,00	0,01	[0,01-0,05]

From table 12, one can see that the measured values form 602, 603 and 604 concur with the target values. 601 has consistently low readings on almost all alloying elements, and a higher Al wt% than the targeted value. None of the observations made during casting would indicate such a deviation. It is a possibility that the spark test mostly measured areas of pure Al-matrix, and did not pick up areas with higher concentration of alloying elements. It is also a possibility that the alloying elements mixed with the slag instead of mixing with the molten aluminium, resulting in a alloy with higher purity than anticipated. The slag composition was not analyzed for any of the castings, due to the limited time for this work.

Table 13: Shows real chemical content for 150% Fe and Mn content on 6082 RSD samples, and their targeted values, where the targeted values are Hydros nom% and max%.

	611	612	613	614	Target
Al [wt%]	96,79	97,51	97,15	97,49	[97,35]
Fe [wt%]	0,36	0,51	0,52	0,35	[0,33-0,36]
Mn [wt%]	0,45	0,24	0,58	0,50	[0,64-0,74]
Si [wt%]	0,96	0,99	0,83	1,00	[0,90-0,95]
Mg [wt%]	0,99	0,62	0,81	0,53	[0,65-0,68]
Cu [wt%]	0,04	0,04	0,04	0,04	[0,0-0,04]
Cr [wt%]	0,10	0,00	0,01	0,00	[0,12-0,15]
Zn [wt%]	0,09	0,05	0,05	0,05	[0,0-0,05]
Ti [wt%]	0,02	0,00	0,00	0,00	[0,01-0,05]

Here the values for the alloying elements seen in table 13 match the targeted values well. Only the Mn and Cr values are lower than the target. That comes from them both being in powder form. When adding alloying elements in powder form, it is much easier for it to oxidize and become dross or slag. The Manganese can also have formed intermetallic phases with high Mn concentrations that the spark test did not measure.

Table 14: Shows real chemical content for 200% Fe and Mn content on 6082 RSD samples, and their targeted values, where the targeted values are Hydros nom% and max%.

	621	**622**	**623**	**624**	**Target**
Al [wt%]	96,63	98,18	97,02	97,56	[96,62]
Fe [wt%]	0,62	0,19	0,63	0,45	[0,44-0,48]
Mn [wt%]	0,91	0,03	0,65	0,66	[0,92-0,98]
Si [wt%]	0,89	1,00	0,93	0,58	[0,90-0,95]
Mg [wt%]	0,81	0,49	0,65	0,67	[0,65-0,68]
Cu [wt%]	0,05	0,04	0,05	0,05	[0,0-0,04]
Cr [wt%]	0,01	0,01	0,01	0,01	[0,12-0,15]
Zn [wt%]	0,06	0,06	0,04	0,01	[0,0-0,05]
Ti [wt%]	0,00	0,00	0,00	0,00	[0,01-0,05]

The accuracy of the spark test depends on how many readings are done per sample, enough readings to get a statistical accurate answer is required to rely on the result. Because of irons low solid solubility in aluminium, it mostly forms intermetallic phases with the other alloying elements and the Al itself. This causes a large difference in concentration of alloying elements, where areas with intermetallic are more concentrated with Fe, Mn, Si, etc., than areas without these intermetallic phases. Because of the small size of these intermetallic phases, more readings per sample are could be a possibility to get a more representative result.

A graphic display of the spark test tables with the targeted Fe and Mn values can be seen in figure 40.

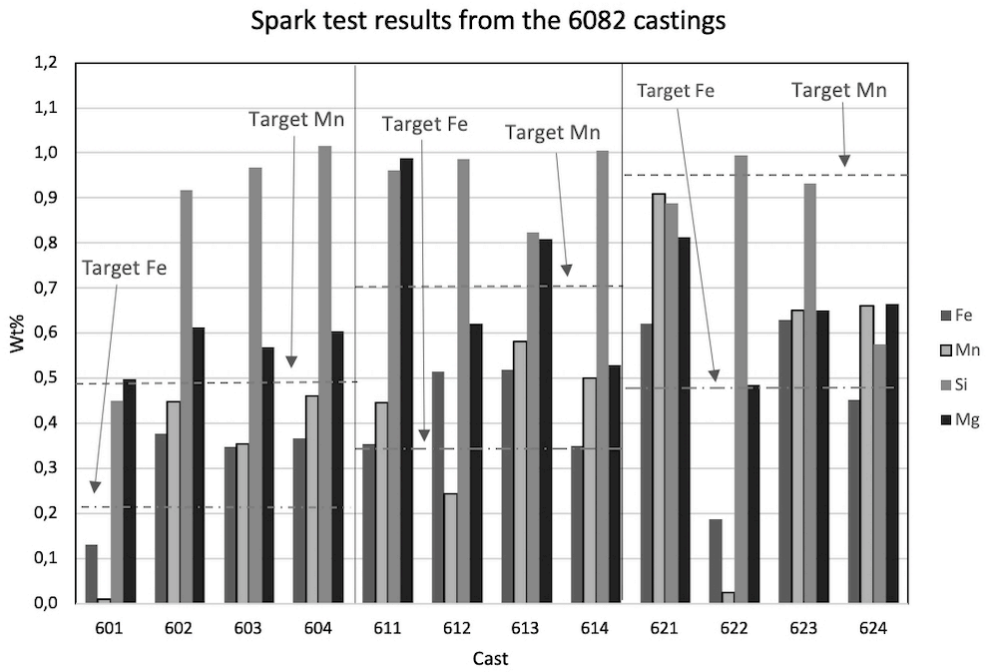

Figure 40: The graph shows the wt% for Fe, Mn, Si and Mg in the different 6082 casts. The target values of Fe and Mn for the different casts are visualized by the stippled lines.

4.2.2 Conductivity testing

To check how much impurities there is in an Al-alloy, conductivity testing can be done. The purer an alloy is, the higher the conductivity measurements will be. Table 15 shows the measurements made on an RSD-sample from each cast. Five readings were taken from each RSD to get a representative average reading.

Table 15: Shows the conductivity measurements done on the 6082 RSD samples, where five spots were taken per sample, measured in [%IACS]

	1	2	3	4	5	Average
601	52,5	53,2	52,3	51,7	53,0	**52,54**
602	37,9	37,6	37,6	37,8	37,7	**37,72**
603	39,1	39,4	39,3	39,4	38,9	**38,92**
604	36,2	35,6	35,7	36,2	35,9	**35,92**
611	32,8	33,8	33,3	33,6	33,3	**33,36**
612	40,8	40,1	40,7	40,8	40,6	**40,60**
613	34,3	34,1	34,1	34,1	34,4	**34,20**
614	37,0	36,6	36,9	35,4	35,6	**36,30**
621	30,3	30,2	30,2	30,3	30,3	**30,26**
622	48,3	48,0	47,7	47,9	47,9	**47,96**
623	34,1	34,0	34,1	33,9	33,9	**34,00**
624	33,9	33,8	34,0	34,0	33,8	**33,90**

If the high values are excluded, the average values drop as the wt% of alloying elements

increase. This indicates less wt% Al, and a higher content of alloying elements, which matches the content of the alloy. Each casts average [%IACS] can be seen in figure 41.

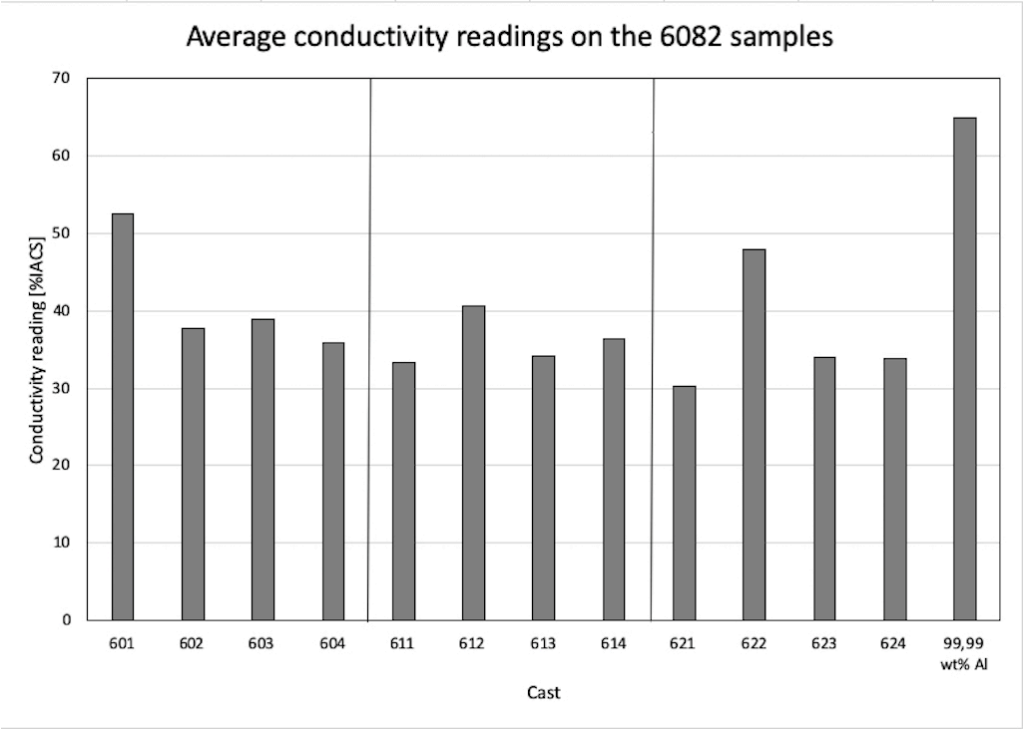

Figure 41: Average conductivity of the samples from 6082 [%IACS].

As seen in table 15 page 55, the samples with the highest conductivity readings are also the samples with the lowest amount of alloying elements present, e.g. 601 and 622. This can be a result of the insufficient dissolution of the various alloying elements.
Based on the collected data, there seems to be no apparent connection between alloying sequence and the values on the conductivity readings, indicating that only the amount of alloying element present in the structure influence the conductivity, not in the sequence that they are added.

4.2.3 Morphology and intermetallic phases

To view the microstructure of the casted samples, SEM pictures were taken. The SEM pictures give valuable information about the size and geometry of the intermetallic phases, as well as the size of grains and grain boundary precipitations.

The temperature is the regulating factor in diffusion, making cooling rate one of the driving variables, and different phases might occur as observed when studying the different phase diagrams. Therefor SEM and EDS should be done on all the samples with different cooling rate. Unfortunately, there was not enough time to do bought sett of samples. SC samples were chosen. Light microscopy images were done on the rapid solidifying samples to compare the different intermetallic phases, as well as the validity of the slow cooled samples as a reference for different the composition of phases. The two samples

appeared to have a high degree of correlation in the morphology of the intermetallic phases.

The results from the spark test show big variation in the compositions of the different parallel alloys. These big variations have to be taken into account when comparing the different samples.

601SC - Al-0,24Fe-0,49Mn-0,95Si-0,68Mg

The rapid solidified cast sample 601 showed a chemical composition of Al-0,13Fe-0,02Mn-0,45Si-0,50Mg (table 12 page 53). This is far below the target composition, as illustrated in figure 40 page 55. The Mn/Fe-ratio is lower than the target. The average conductivity of the rapid solidified sample is 52,54 %IACS (table 15 page 55).

The intermetallic phases in the RSD have similar morphologies to the phases present in the SC sample. This can be seen in figure 94 page 103 Thinly lined intermetallic phases along the grain boundaries with script-like structure can be observed in both samples. The intermetallic phases with needle-morphology are approx. 20μm long.

Around some of the needles, Mg_2Si started to form, and these precipitations can be observed in both samples. Spot 482 seen in figure 53 page 71 is a thin needle of Al-9,43Fe-2,66Si-1,10Mg Atomic%. This is suspected to be a β-needle, based on the morphology and chemical composition. Spot 253 in the figure had similar wt% composition. This suggest that these phases have equal stoichiometric compositions. It should be noted that no Mn readings were detected on the EDS. It can be seen from the spark test in figure 12 page 53, that the Mn content in the sample is low, which explains the lack of Mn in the intermetallic phases.

602SC - Al-0,24Fe-0,49Mn-0,95Si-0,68Mg

The rapid solidified cast sample 602 showed a chemical composition of Al-0,38Fe-0,45Mn-0,92Si-0,61Mg (table 12 page 53). This reading matches the target composition, as illustrated in figure 40 page 55. The average conductivity of the rapid solidified sample is 37,72 %IACS (table 15 page 55).

When comparing the rapid solidifying disc with the slow cooled sample, phases with similar morphology can be observed (figure 95 page 103). The average size of the precipitations seems to be bigger in the SC. From the SEM pictures, one can see clusters of intermetallic phases scattered in the microstructure. There are almost no signs of grain boundaries or grain boundary precipitations. There are some possible Mg_2Si intermetallic phases in the samples. There appears to be a fish bone and script-like intermetallic, with the addition of some intermetallic phases which are grain-like. Two Spots were analyzed with the EDS a seen in figure 42. The results show a composition of Al-6,29Fe-2,08Mn-4,70Si-1,10Mg, giving a $\frac{Mn}{Fe}$-ratio of 0,33. The second spot shows a composition of Al-8,60Fe-2,74Mn-5,77Si-1,24Mg, giving a $\frac{Mn}{Fe}$-ratio of 0,12. The spot is in an area where the cluster has grown bigger, and the intermetallic phase has a more grain like

structure with sharp edges. The ratios and the content of these two phases match the content and ratios seen in the α-phase. Areas of high concentration Si were also found. This leads to the belief that the Si was not properly/equally distributed in the melt creating over-saturated areas of Si.

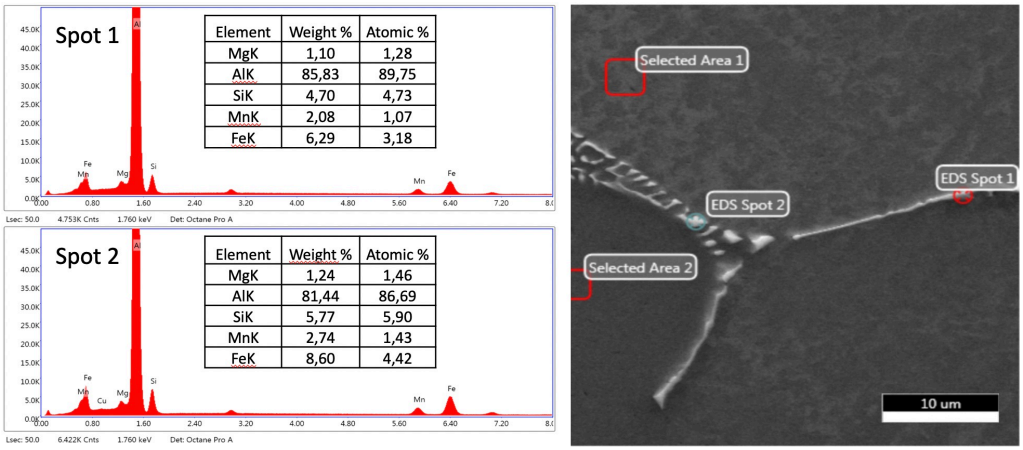

Figure 42: EDS analysis of the script like intermetallic in the slow cooled Al-0,24Fe-0,49Mn-0,955Si-0,68Mg sample 602 where Fe is added before Mn and Mg in the melt.

603SC - Al-0,24Fe-0,49Mn-0,95Si-0,68Mg

The rapid solidified cast sample 603 showed a chemical composition of Al-0,35Fe-0,36Mn-0,97Si-0,57Mg (table 12 page 53). This reading matches the target composition, as illustrated in figure 40 page 55. The average conductivity of the rapid solidified sample is 38,92 %IACS (table 15 page 55).

When comparing the microstructures of the RSD to the SC, one can see intermetallic precipitations with the same morphology, but in the RSD their average size is larger, figure 96 page 104. The intermetallic phases shape and distribution is similar to the ones in sample 602. Analysis of the EDS (figure 117 page 115) shows a composition of the script-like structure to be Al-19,33Fe-4,89Mn-8,99Si-0,83Mg (spot 1) and Al-17,31Fe-5,11Mn-8,43Si-1,15Mg (spot 3). Giving spot 1 a $\frac{Mn}{Fe}$-ratio of 0,25 and spot 2 a $\frac{Mn}{Fe}$-ratio of 0,29, matching the α-$Al_{15}(Fe, Mn)_3Si_2$ in both chemical content and morphology.

604SC - Al-0,24Fe-0,49Mn-0,95Si-0,68Mg

The rapid solidified cast sample 604 showed a chemical composition of Al-0,37Fe-0,46Mn-1,02Si-0,61Mg (table 12 page 53). This reading matches the target composition, as illustrated in figure 40 page 55. The average conductivity of the rapid solidified sample is 35,92 %IACS (table 15 page 55).

When comparing the two samples, little difference can be seen between the rapid solidifying disc and the slow cool. Figure 97 page 104. They both have intermetallic phases with the same morphology and size, in addition to some Mg_2Si. The SEM pictures from the 604SC show, like the 602 and 603, a fishbone-like intermetallic phase. In this sample, it may appear that the cluster of intermetallic precipitations is larger than for sample 602 and 603. From the EDS, one can see two slightly different morphology's. The first area

has a almost Hebrew script (more rounded) with the composition of Al-8,20Fe-3,75Mn-7,53Si-1,15Mg (spot 1) and Al-4,50Fe-2,10Mn-4,73Si-1,04Mg (spot 4). This might be the α-$Al_{15}(Fe, Mn)_3Si_2$ intermetallic phase.

Summary 6082 nominal composition - Al-0,24Fe-0,49Mn-0,95Si-0,68Mg

In sample 604, it seems that the intermetallic phases have collected together more in networks than in sample 602 and 603. The spark test for sample 601 show that it is low in Mn (0,02, target: 0,43) and Si (0,45, target: 0,9), and therefore it has little intermetallic phases present. The SEM-pictures of the microstructures can be seen in figure 43.

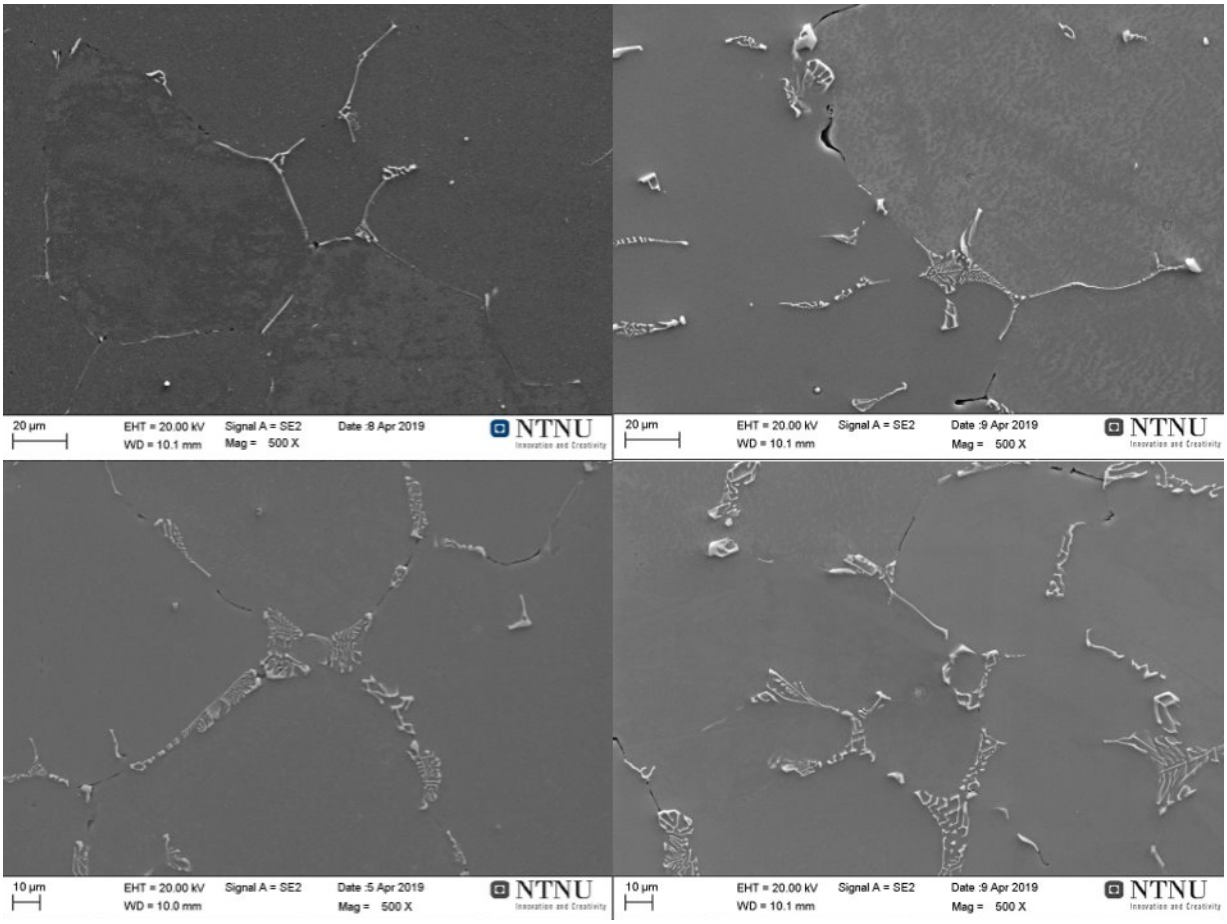

Figure 43: SEM pictures from the parallels on nominal 6082 samples. Top left shows sample 601, top right is 602, bottom left is 603, and bottom right is 604.

611SC, Al-0,36Fe-0,74Mn-0,95Si-0,68Mg

The rapid solidified cast sample 601 showed a chemical composition of Al-0,36Fe-0,45Mn-0,96Si-0,99Mg (table 13 page 53). The Fe and Si content match the target levels, the Mn content is lower than the target, and the Mg content is higher. This is illustrated in figure 40 page 55. The average conductivity of the rapid solidified sample is 33,36 %IACS (table 15 page 55).

Comparing the rapid solidifying disc against the slow cool reveals little to no differences,

figure 98 page 105. The intermetallic phases precipitate mostly along the grain boundaries in what looks like fish bone and script structure. The intermetallic phases have a length of 5-30 µm. The RSD microstructure can be observed in figure 44. Here, the formation of Mg_2Si can also be observed. The cast have quite a bit more intermetallic phases than in the castings with nominal wt% Fe and Mn.
EDS spot analysis (figure 119 page 116) was done on a Mg_2Si phase, showing a composition of Al-2,47Si-1,20Mg (spot 1). The script like phase near the Mg_2Si-phase showed a composition of Al-4,96Fe-2,00Mn-2,39Si-1,23Mg (spot 2). This might be the α-$Al_{15}(Fe, Mn)_3Si_2$-phase with Mg dissolved.

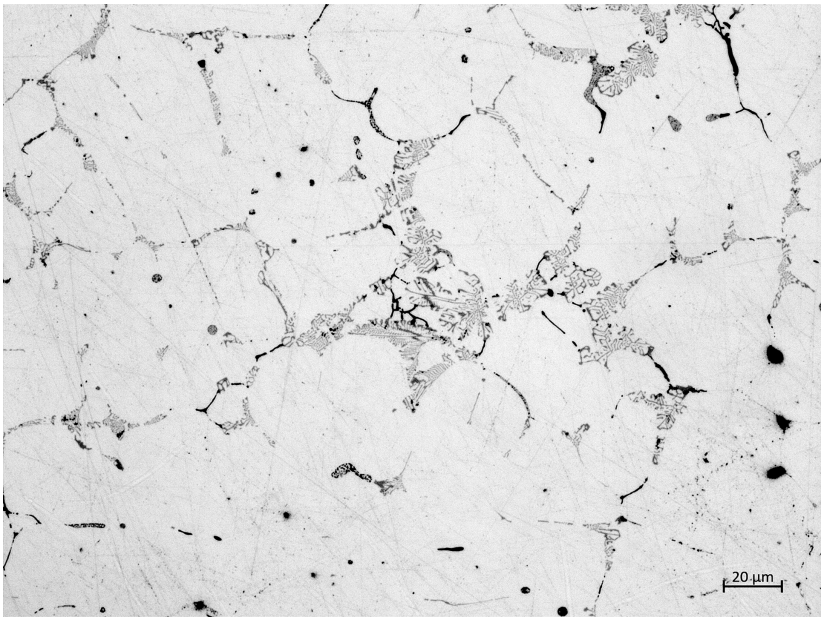

Figure 44: LMI picture of rapid solidifying disc sample 611, 150 wt% Fe and Mn where all alloying elements are added in cold crucible. Showing a possible α-$Al_{15}(Fe, Mn)_3Si_2$ and Mg_2Si.

612 SC, Al-0,36Fe-0,74Mn-0,95Si-0,68Mg

The rapid solidified cast sample 612 showed a chemical composition of Al-0,36Fe-0,45Mn-0,96Si-0,99Mg (table 13 page 53). The Fe and Si content match the target levels, the Mn content is lower than the target, and the Mg content is higher. This is illustrated in figure 40 page 55. The average conductivity of the rapid solidified sample is 33,36 %IACS (table 15 page 55).

Comparing the intermetallic phases present in the rapid solidifying disc sample with the ones in the slow cool sample reveal a difference in morphology, figure 99 page 105. The intermetallic phases in the SC sample are thin lines with areas of script-like precipitations. In the RSD sample, there are large clusters of script-like precipitations with length up to 20 µm. Two EDS analysis (figure 120 page 116) of the intermetallic precipitations shows a composition of Al-9,80Fe-0,96Mn-12,92Si-1,23Mg (spot 1), and Al-17,03Fe-2,39Mn-7,95Si-1,06Mg atomic% (spot 3). A possible α- or π-phase.

613SC, Al-0,36Fe-0,74Mn-0,95Si-0,68Mg

The rapid solidified cast sample 613 showed a chemical composition of Al-0,52Fe-0,58Mn-0,83Si-0,81Mg (table 13 page 53). The Mn and Si content is lower than the target, and the Fe and Mg content is higher. This is illustrated in figure 40 page 55. The average conductivity of the rapid solidified sample is 34,20 %IACS (table 15 page 55).

Both the SEM pictures of the slow cooled sample and the light microscope images from the rapid solidifying disc shows large clusters of script-like intermetallic phases and Mg_2Si along the grain boundaries, figure 100 page 106. An LMI of these precipitations can be seen in figure 45, where the intermetallic phases vary in length between 1 - 20 µm. The width of the script-like intermetallic precipitations varies from 5µm along grains up to clusters reaching 50 µm in diameter located in intersections of several grains.

The EDS analysis was done on two spots at the end of the script like intermetallic. The first analysis was done on a bulky part of the precipitation, showing a composition of Al-18,66Fe-5,87Mn-8,91Si-0,73Mg (spot 1). The second analysis was done on a spot like intermetallic on the end of what appears to be a script formation. The spot had an atomic composition of Al-10,43Fe-4,15Mn-6,39Si-1,08Mg (spot 2). Both morphology and composition that could match of α-$Al_{15}(Fe, Mn)_3Si_2$.

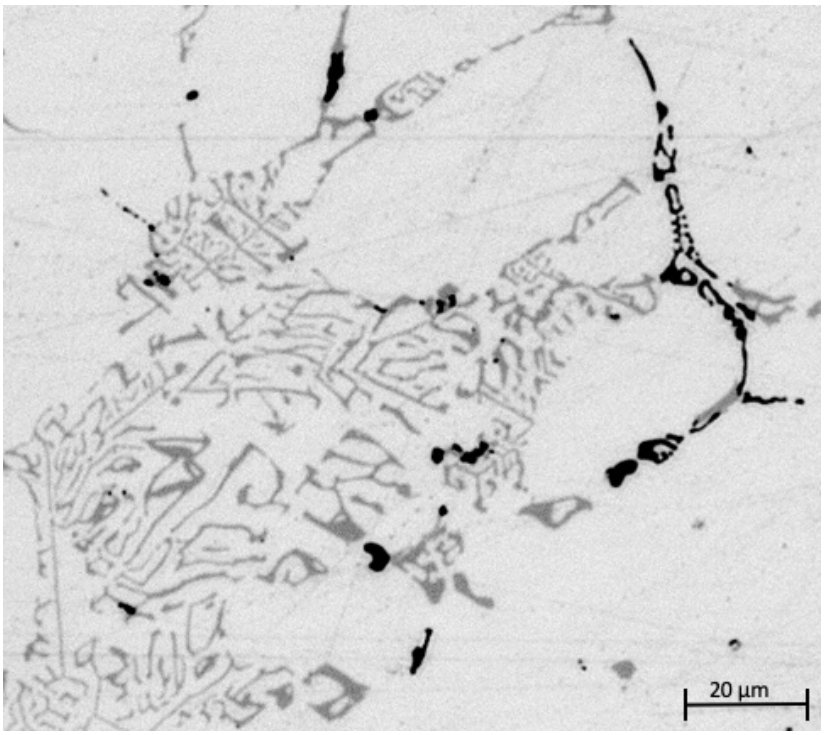

Figure 45: Script-like intermetallic phases in the rapid solidified Al-0,36Fe-0,74Mn-0,95-0,68Mg sample (613). The difference in colour and thickness of the two script-like precipitations might indicate different compositions.

614SC, Al-0,36Fe-0,74Mn-0,95Si-0,68Mg

The rapid solidified cast sample 614 showed a chemical composition of Al-0,35Fe-0,50Mn-1,00Si-0,53Mg (table 13 page 53). The Fe content matches the targeted values, the Mn and Mg content is lower than the target, and the Si content is higher. This is illustrated in figure 40 page 55. The average conductivity of the rapid solidified sample is 36,30 %IACS (table 15 page 55).

There seems to be little difference between the intermetallic phases present in the rapid solidifying disc and the slow cool sample, figure 101 page 106. Both samples have areas with large script-like precipitations and Mg_2Si phases. More massive clusters form at the intersection of several grains up to 30 µm in width. The EDS analysis (figure 122 page 117) of the possible Mg_2Si show a composition of Al-18,10Si-10,73Mg (spot 1).The script like structure was found to have a composition of Al-1,32Fe-0,87Mn-2,58Si (spot 2). There is always an uncertainty in the EDS scans, as lighter elements reflect less than heavier elements.

Summary 150 wt% Fe and Mn 6082 - Al-0,36Fe-0,74Mn-0,95Si-0,68Mg

The intermetallic phases present in sample 612 appear to be thinner than the phases present in sample 611. The clusters of intermetallic phases seem to be smaller in sample 614 and 612 than in sample 613. Sample 611 seems to have less cluster formation near intersections, but have wider script-like areas than the other samples. The Mg_2Si is present in all samples, and there seems to be no difference in size or where it appears. The microstructure of the different samples can be observed in figure 46.

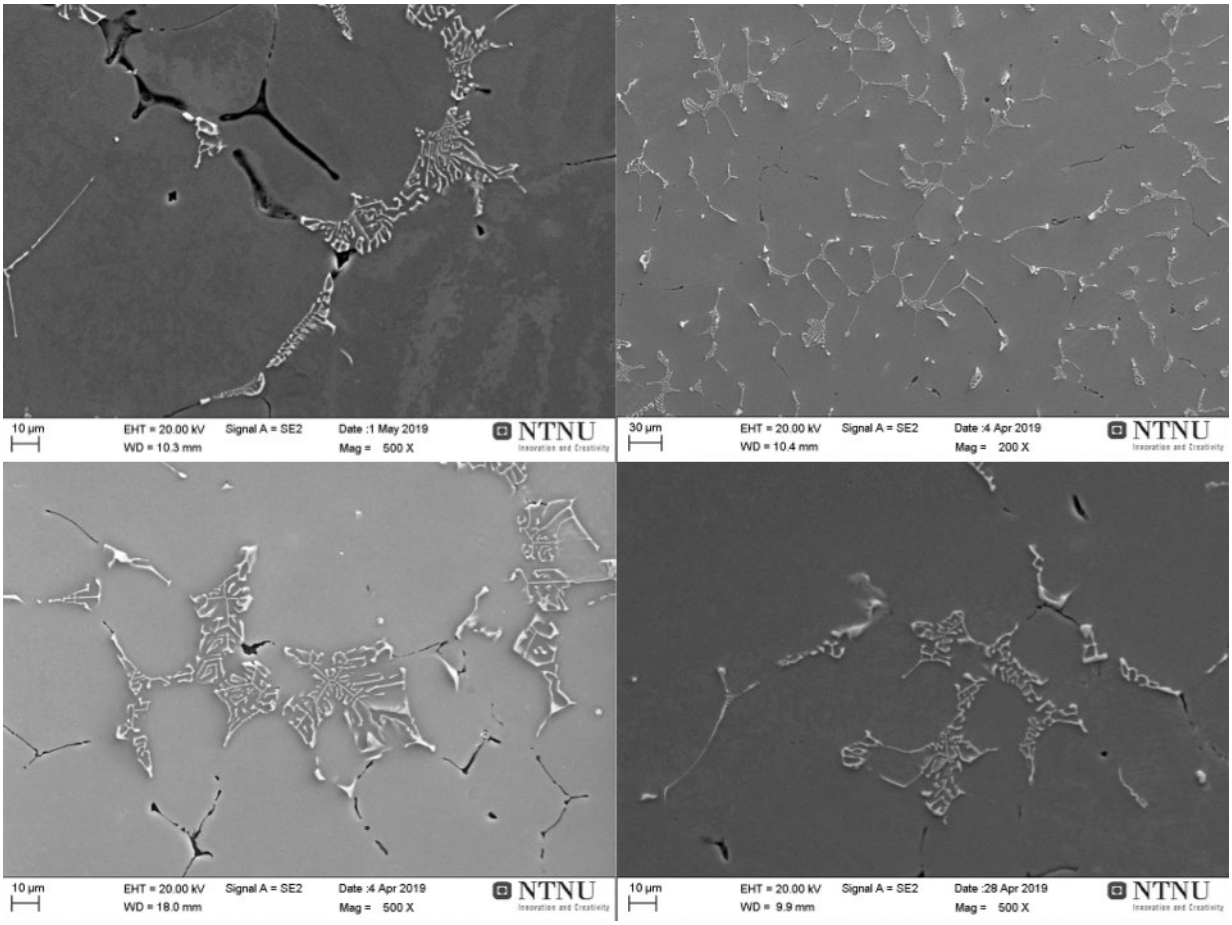

Figure 46: SEM pictures from the 6082 parallels containing 150 wt% Fe and Mn. Top left shows sample 611, top right is 612, bottom left is 613, and bottom right is 614.

621 SC, Al-0,48Fe-0,98Mn-0,95Si-0,68Mg

The rapid solidified cast sample 621 showed a chemical composition of Al-0,62Fe-0,91Mn-0,89Si-0,81Mg (table 14 page 54). The Fe and Mg content is higher than the targeted values, while the Mn and Si content matches the targeted values. This is illustrated in figure 40 page 55. The average conductivity of the rapid solidified sample is 30,26 %IACS (table 15 page 55).

Both the morphology and the size of the intermetallic phases present in the rapid solidifying disc and the slow cooled sample are similar, figure 102 page 105. In the RSD there seem to be more intermetallic phases than there are in the SC, as the precipitations appear more frequent in the RSD. EDS analysis from the sample can be seen in figure 123. Spot 2 was taken on a thin intermetallic line and shows a composition of Al-6,96Fe-5,10Mn-4,65Si-1,18Mg, giving a $\frac{Mn}{Fe}$-ratio of 0,7. Spot 3 was taken on a bulkier part of the phase and had a composition of Al-12,53Fe-7,69Mn-7,40Si-1,05Mg, resulting in a $\frac{Mn}{Fe}$-ratio of 0,6. Both of these ratios match those of α-$Al_{15}(Fe,Mn)_3Si_2$.

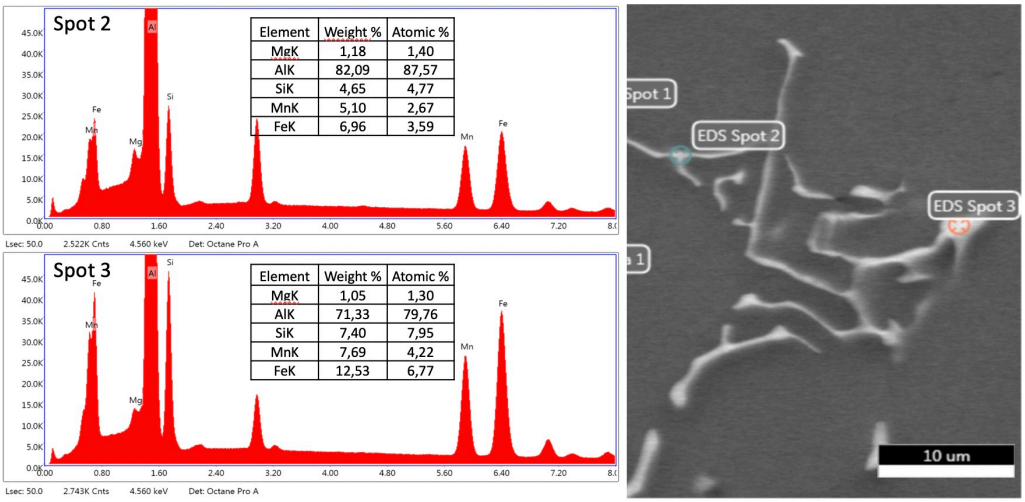

Figure 47: EDS analysis of the script-like intermetallic phase in the slow cooled Al-0,48Fe-0,98Mn-0,955Si-0,68Mg sample (621).

622SC - Al-0,48Fe-0,98Mn-0,95Si-0,68Mg

The rapid solidified cast sample 622 showed a chemical composition of Al-0,19Fe-0,03Mn-1,00Si-0,49Mg (table 14 page 54). This is far below the target composition as illustrated in figure 40 page 55. The average conductivity of the rapid solidified sample is 47,96 %IACS (table 15 page 55).

The microstructure of the cast can be seen in figure 48. In the slow cooled sample (b), all intermetallic phases have formed as thin needles or possible Mg_2Si. The needle-like intermetallic precipitations clearly form along the grain boundaries, but smaller nail like intermetallic phases form in some areas in what appears to be random directions. In the rapid solidified sample, there appears to a phase that grown out of the needle. This might be the π-$Al_8FeMg_3Si_6$ intermetallic phase. More images from the sample can be seen in figure 103 page 107.

The EDS analysis(figure 124 page 65) shows an composition of the needle to be Al-13,10Fe-11,16Si (spot 1), and the possible Mg_2Si to be Al-2,69Fe-20,12Si-15,96Mg. It should be noted that Mg shows a visible peak in the spectrum, but did not print in the results. The Mg_2Si scan was done near a nail-like intermetallic phase, probably influencing the reading of Fe. The needle-like phases are what to appear to be β-needles, and in the figure, what seems to be π-phase can be seen emerging from the needle. The π-phase often grows out from a β-phase, but can also emerge from the Al-matrix.

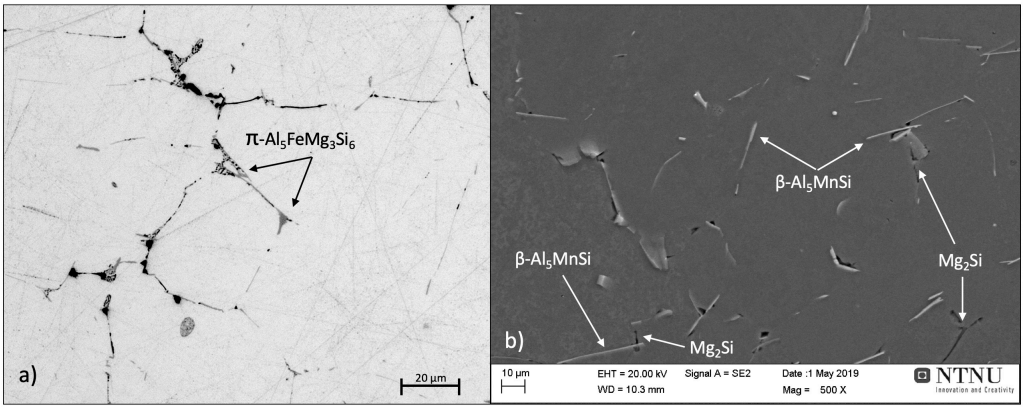

Figure 48: a) LMI of a rapid solidifying disc, showing a possible π-$Al_8FeMg_3Si_6$ intermetallic phase. b) SEM-picture of slow cool showing a possible Mg_2Si- and β-Al_5FeSi phase.

623 SC, Al-0,48Fe-0,98Mn-0,95Si-0,68Mg

The rapid solidified cast sample 623 showed a chemical composition of Al-0,63Fe-0,65Mn-0,93Si-0,65Mg (table 14 page 54). The Fe content is higher than the targeted values, while the Mn is lower. The Si and Mg content match the targeted values. This is illustrated in figure 40 page 55. The average conductivity of the rapid solidified sample is 34,00 %IACS (table 15 page 55).

The intermetallic phases present in the rapid solidifying disc appear to be the same as those present in the slow cooled sample, this is because they have the same morphologies and size. Images can be seen in figure 104 page 108. The only noticeable difference is that the precipitations appears more frequent in the RSD. The intermetallic phases have a script-like appearance, and areas of Mg_2Si can be observed. The phases appear both in clusters, but also by themselves. The script-like intermetallic phase varies in thickness from 5 to 10 µm, and the cluster formations up to a width of 50 µm.

624 SC, Al-0,48Fe-0,98Mn-0,95Si-0,68Mg

The rapid solidified cast sample 624 showed a chemical composition of Al-0,45Fe-0,66Mn-0,58Si-0,67Mg (table 14 page 54). The Fe and Mg content match the targeted values, while the Mn and Si is lower. This is illustrated in figure 40 page 55. The average conductivity of the rapid solidified sample is 33,90 %IACS (table 15 page 55).

Form figure 105, page 108, the sample from the rapid solidifying disc and the sample of the slow cool shows areas of script-like intermetallic phases, areas with clusters of script-like intermetallic phases, and Mg_2Si precipitations. In the SC from SEM, large concentrations of Mg_2Si can be seen (fig. 49). The EDS analysis (figure 125 page 119) shows a composition of the possible α-phase to be Al-13,65Fe-5,56Mn-6,72Si (spot 2) and Al-12,91Fe-6,28Mn-7,66Si (spot 3). The spectre shows a peak for Mg but no reading in the results.

Summary 200 wt% Fe and Mn 6082 - Al-0,48Fe-0,98Mn-0,95Si-0,68Mg

Samples 621, 623, and 624 have the same intermetallic phases, while 622 has a different microstructure. The difference in microstructure might be a result of the low Mn values present, as can be seen from the spark test in table 14. When the Mn is not present in the system, Fe can form needle-like structures with Si. In sample 624 there were areas with concentrated Mg_2Si precipitations, whereas in samples 621 and 623 they were more evenly distributed. The microstructure of the different samples can be observed in figure 49.

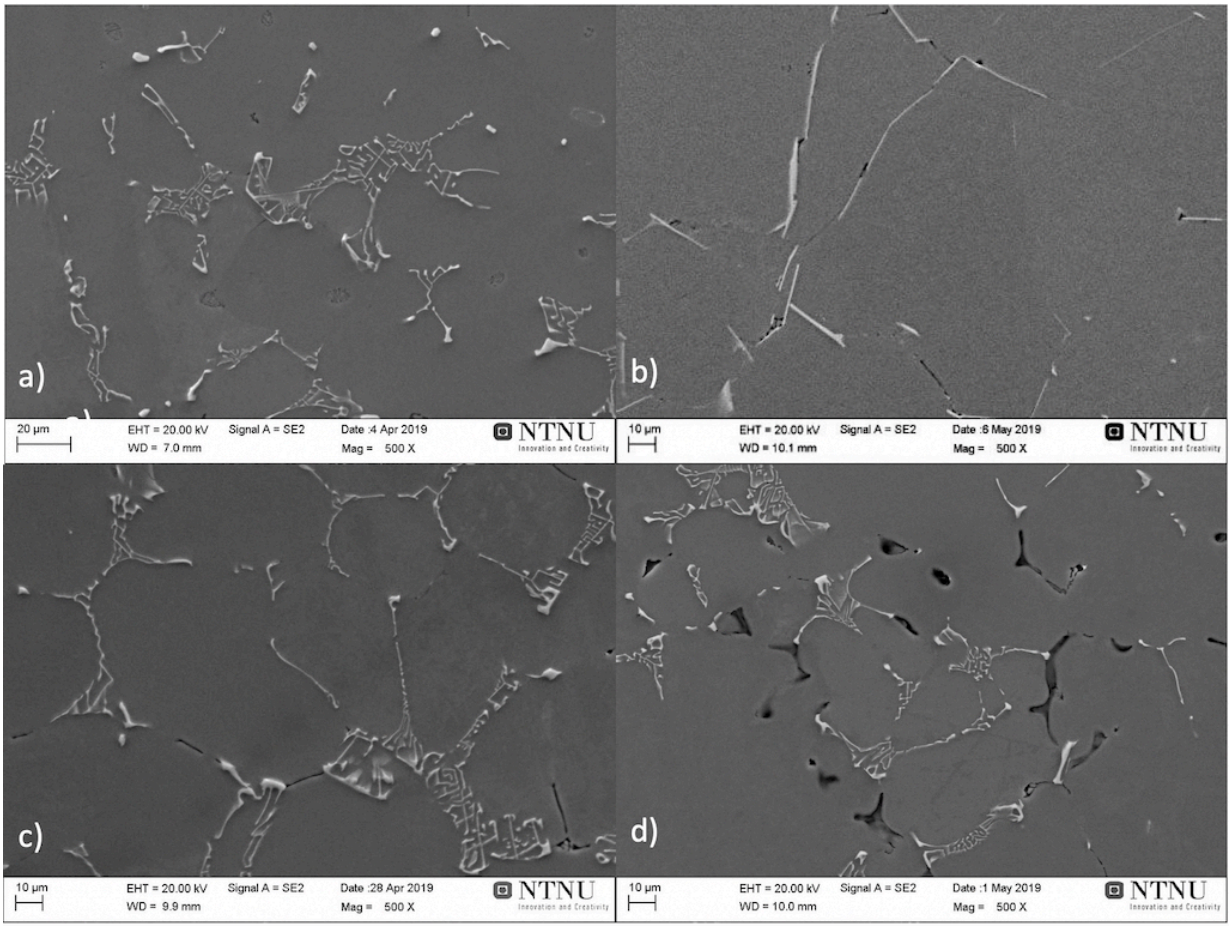

Figure 49: SEM pictures from the 6082 parallels containing 200 wt% Fe and Mn; a) shows sample 621,b) is 622,c) is 623,d) is 624.

4.2.4 Tensile testing 6082

The stress-strain curves from all the casts can be found in appendix A. The average yield strength and tensile strength can be seen in figure 50.

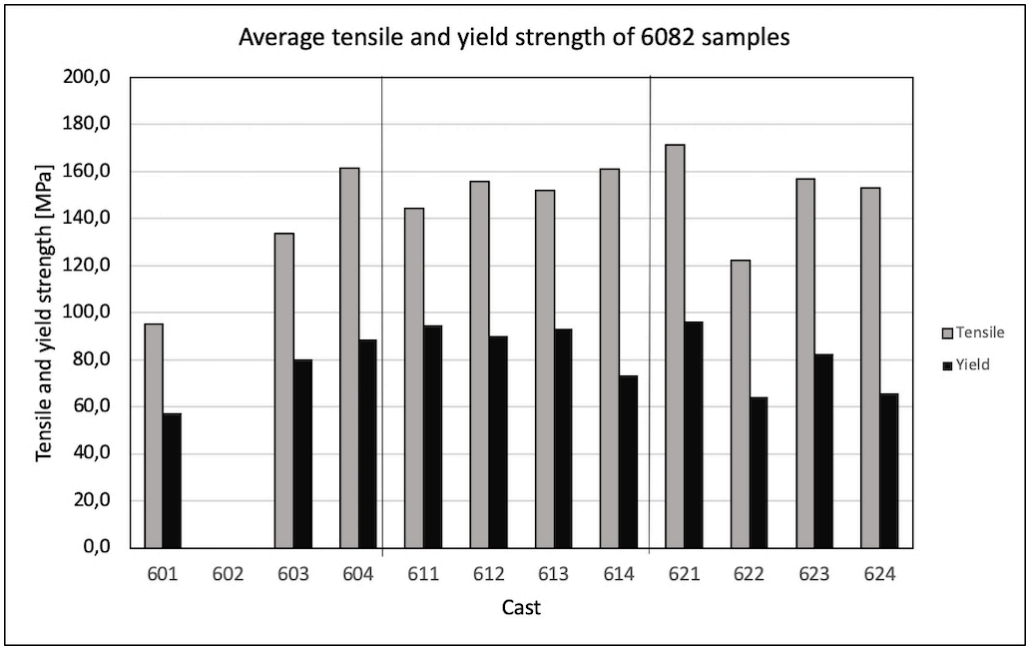

Figure 50: Shows the average yield and tensile strength from the 6082 casts. Five specimens were taken from each cast to get a representative result.

The results from the tensile tests done on the 6082 series show a more brittle aluminium than the 3103 series.

The difference in the average σ_y between the nominal and 200 wt% samples is 1,78 MPa, a difference of 2,3%. The difference between nominal composition and 150 wt% was the largest, 12,4 MPa, resulting in a difference of 14,1%.

The 150 and 200 wt% samples have similar average σ_{TS} values, 153,3 MPa and 150,9 MPa respectively. The nominal samples had an average σ_{TS} of 130,1 MPa, making it 15,1% lower than the 150 wt% castings.

The average elongation values for the different sets are 2,6% for nominal composition, 2,36% for 150 wt%, and 3,03% for 200 wt%. This is a difference of 21,3% between the 150 wt% samples which have the lowest elongation, and the 200 wt% samples, which have the highest. It is interesting to note the different elongation behaviour in the 6082 alloy compared to the 3103 alloy. The 3103 alloy had a clear decrease in elongation as larger amouts of Fe and Mn was added. This can not be observed in the 6082 alloy.

4.2.5 Thermodynamic modeling 6082

For the calculations in FactSage, the Al-XFe-YMn-0,68Mg-0,68Si was chosen for modelling the 6082 phase diagrams. The levels of background elements were kept constant at 0,095 wt% Si and 0,68wt% Mg. Several iterations of the diagram were calculated from Fe [0, 100]g/g to Fe [0, 5]g/g. The modelled Al-Fe phase diagram of the nominal 6082 alloy can be seen in figure 51.

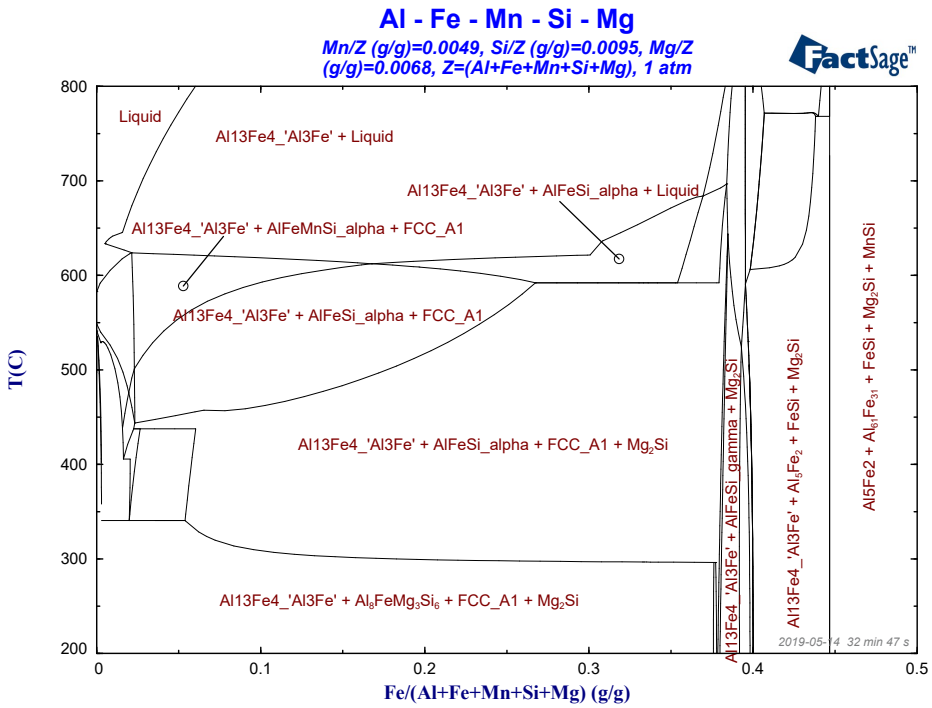

Figure 51: The FactSage calculated binary Phase diagram for a 6082 alloy. There are several phase lines that are not drawn in the diagram.

The diagram has oblivious flaws in the drawing of the diagram in the low Fe wt% part of the diagram, where lines are missing. This can be seen in figure 52.

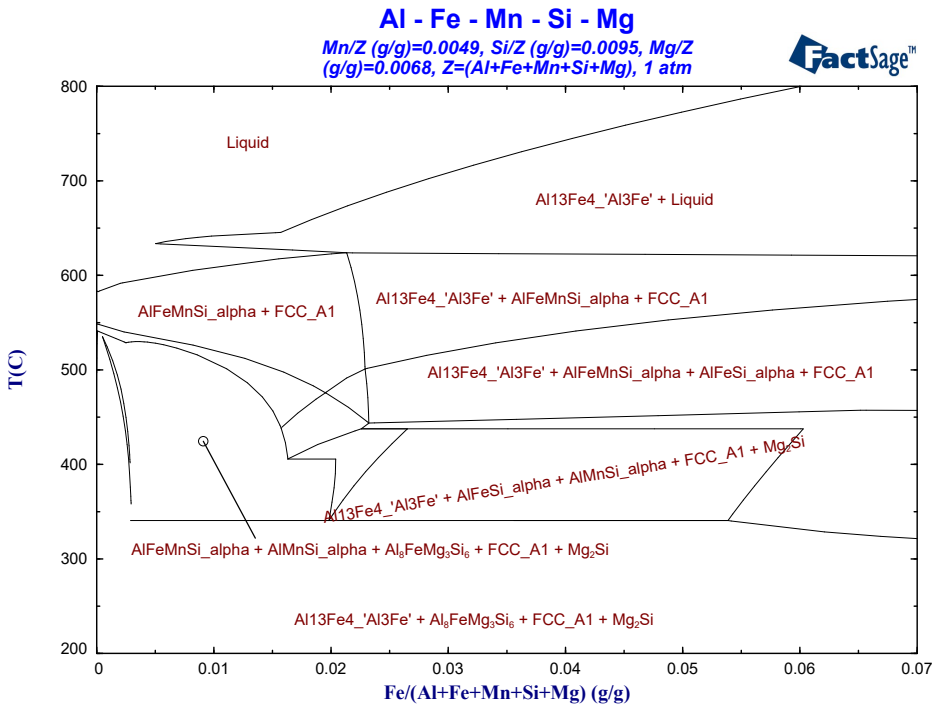

Figure 52: The FactSage calculated binary Phase diagram for a 6082 alloy.

Al_3Fe has a low solubility of Mn (4-5%) [52]. From the diagram, one can see that above 340°C this leads to the formation of different α-phases under 6wt% Fe.

Table 16: Shows the receipt for the calculation of the Al-0,49Mn-0,95Si-0,68Mg-[0, 0.5]Fe 6082 alloy. The result is as printed out by FactSage Phase Diagram module.

	Stable Phases	
1	FTlite-Liqu Liquid	metal
2	FTlite-Al13 Al13Fe4_'Al3Fe'	mC102 C2/m Al-rich Al-Fe phase with solubility for Mn and Zn.
3	FTlite-oC24 Al5Fe2	oC24 Cmcm Phase at ca. 71.5 at.% Al in Al-Fe. Solubility for Mn and Zn.
4	FTlite-AFMS AlFeMnSi_alpha	Al-Fe-Mn-Si quaternary solution
5	FTlite-Tau5 AlFeSi_alpha	(Tau 5) Hexagonal. Looks usually like chinese script or rod-like in Al-Fe-Si alloys approx. Stoichiometry Al7Fe2Si
6	FTlite-Tau2 AlFeSi_gamma	(Tau 2) Monoclinic approx. stoichiometry Al3FeSi
7	FTlite-AlM1 AlMnSi_alpha	Cubic cP138 Pm-3 approx. stoichiometry Al9Mn2Si with solubility of Fe
8	FTlite-Diam Diamond_A4	Prototype_C-diamond-A4 cF8 Fd-3m (227) C, Ge, alpha-Sn and Si are stable
9	FTlite-FCC FCC_A1	Prototype_Cu-A1 cF4 Fm-3m (225) C, N, B and H interstitial
10	compound Al5Fe2(s)	pure substance Al5Fe2_Cmcm_oC24(s)
11	compound Al61Fe31(s)	pure substance Al61Fe31_Al2Fe_aP18_P(s)
12	compound Al8FeMg3Si6(s)	pure substance Al8FeMg3Si6_Pi-phase_(s)
13	compound FeSi(s)	pure substance FeSi_B20_cP8_P213(s)
14	compound Mg2Si(s)	pure substance Mg2Si_cF12-Fm(3)m(s)
15	compound MnSi(s)	pure substance MnSi_cP8_P2(1)3_FeSi(s)

From table 16 one can see the formation of the α-AlFeSi script and α-AlFeMnSi. A problem with the results is the lack of computational information about each phase in the

stable phase diagram. From the stable phase receipt, there is no mention of the β-Al_5FeSi phase, which seems to correlate with the experimental findings. Phase 12 in table 16 is the π-$Al_8FeMg_3Si_6$ and phase 13 the Mg_2Si-phase. This indicates that the Mg levels in the alloy is high enough for the β-Al_5FeSi to completely transform to the less harmful π-phase. A reoccurring problem in the calculations was the existence of several binary and ternary products that, according to the literature, should not exist in equilibrium, or phases that are only theoretically found. Some of these phases were located in the «pure solids» package. The excluding of packages from the calculations is not preferable as it might hinder the program in calculating intermediate and stable phases. Table 7 page 14 was used to correlate the validity of the different phases in calculated. The list of stable phases can be seen in the table 16.

4.3 Intermetallic composition

4.3.1 α-$Al_{15}(Fe, Mn)_3Si_2$

What appears to be α-$Al_{15}(Fe, Mn)_3Si_2$ were found in all of the 6082 castings except from the 622 cast. The EDS analysis of the different script-like intermetallic phases shows big variations in the composition of Fe and Mn in the phases. This match the findings of the European research program studying this, as they found that this phase had a broad homogeneity range, as seen in figure 9 on page 13 [7]. The phases would often form together, as large clusters in the microstructure.

Increasing Mn levels in the phase seems to give a more block-like structure, as seen in figure 42 page 58 between spot 1 and spot 2 from cast 621.

In the different 3103 casts, there were found what could be α-$Al_{15}(Fe, Mn)_3Si_2$ in the slow cooled samples from cast 303, 313, 321, 322, and 324. There were found script-like intermetallic phases in all the castings in 3103, but EDS analysis showed that most of these phases most likely are $Al_6(Fe, Mn)$. These two phases are hard to distinguish without doing EDS, as they can have similar morphologies.

4.3.2 β-Al_5FeSi

The β-Al_5FeSi has a solubility of Mn of max 0,8 wt% [34].

The 601 slow cooled sample showed a morphology that might be β-Al_5FeSi. The EDS analysis is shown in figure 53.

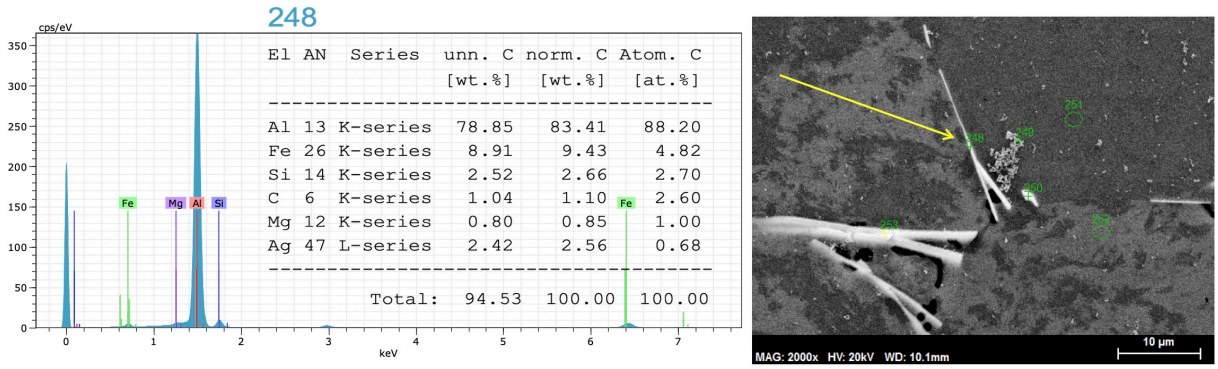

Figure 53: Possible β-Al_5FeSi in the 601 slow cooled sample, showing a composition of Al-9,43Fe-2,66Si [wt%].

The orientations of the nearby intermetallic phases suggest that this might be a β-Al_5FeSi as they often grow in large networks with similar orientation [2]. There appear to be cracks in the larger prisms.
In the 622 Slow cooled sample (fig. 48) there is what appears to be needles close connected to Mg_2Si intermetallic phases. The addition of Mg and Mn should promote the formation of the π-$Al_8FeMg_3Si_6$. In the 622 there seems to be a lack of Mn in the sample as figure 40 page 55 clearly illustrates. There is also low levels of Fe in the sample, which might explain the relatively small size of the β-Al_5FeSi and the formation of Mg_2Si in areas around the needle.

The effect of Mn as a suppressor of the β-Al_5FeSi intermetallic phase seems to be good, as it is not seen in other samples with high amounts of Fe.

4.3.3 Al_6(Fe, Mn)

It was observed considerable amounts of what appears to be Al_6(Fe, Mn) in the casts with 150 and 200 wt% Fe and Mn in the 3103 alloy. The intermetallic phase precipitated in very different morphologies and (Fe, Mn) combinations. In these samples it was found large amounts of primary Al_6(Fe, Mn). Cracking of the phase has been observed on several different samples. In the slow cooled samples, the phase was found in all the 150% Fe and Mn casts and one 200% cast. Light microscope images of the phase can be seen in figure 54.

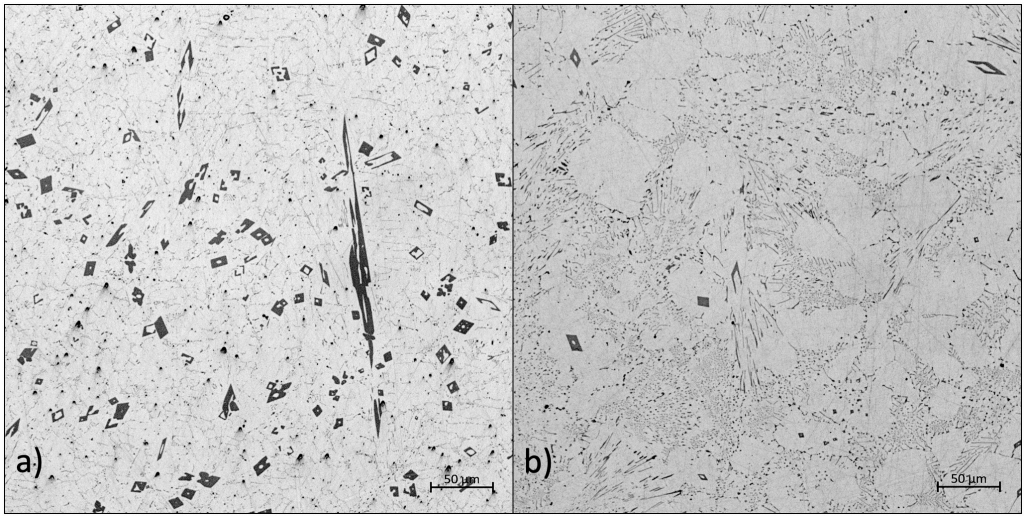

Figure 54: LMI pictures of primary $Al_6(Fe, Mn)$ in the RSD sample from a) 312 cast and b) 322.

In the RSD samples, the phase was found in all 31X samples as well as the 322 and 324 samples. In the 322 and 324 cast there was a large difference between the RSD and SC samples. Figure 54 shows the difference between the amount of primary $Al_6(Fe, Mn)$ in the 312 and 322 RSD samples. Figure 55 show the SC from the same two. There is a large difference from the 322 RSD to the SC, but not for the 312 samples. The casting procedure was equal on both sets of samples.

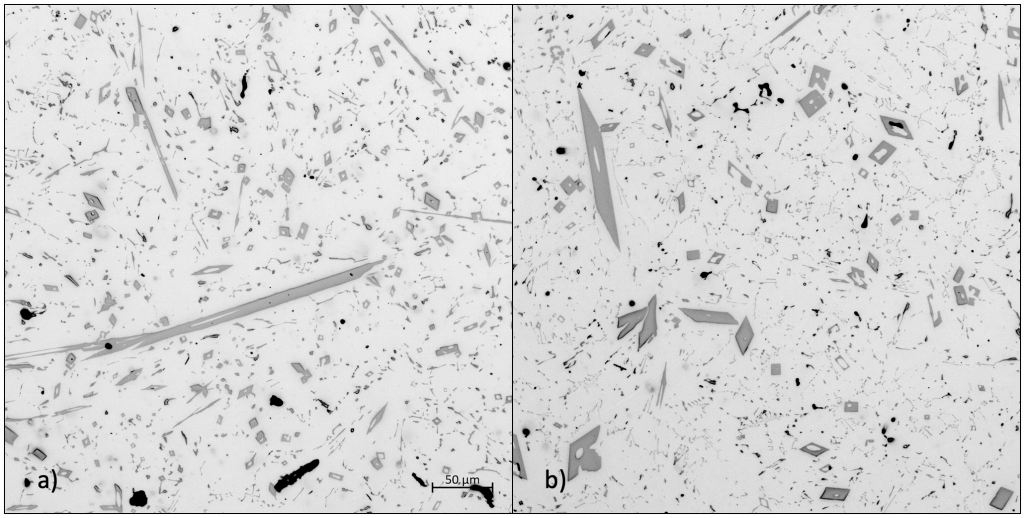

Figure 55: LMI pictures of primary $Al_6(Fe, Mn)$ in the SC sample from a) 312 cast and b) 322.

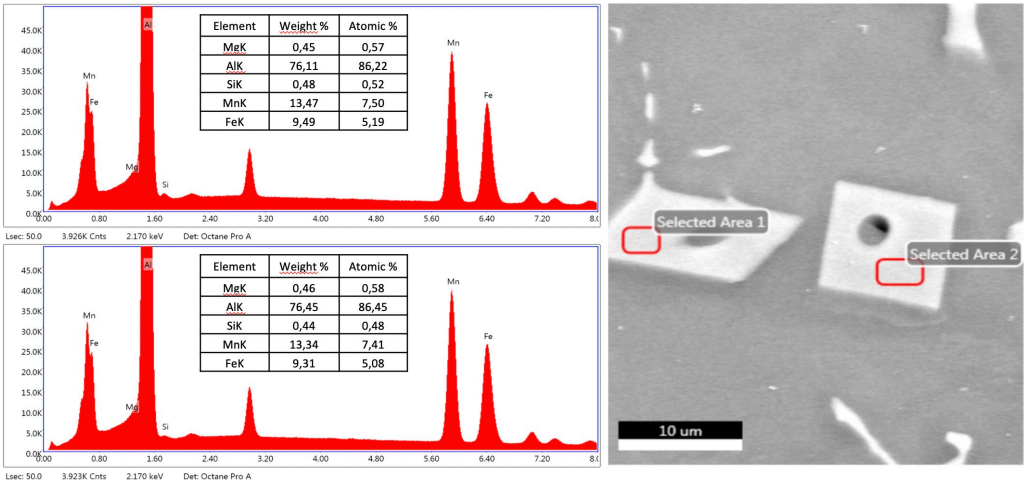

Figure 56: EDS analysis (EDAX TEAM) on the 312 SC sample of the primary Al_6(Fe, Mn)

When comparing the different EDS analysis of the primary Al_6(Fe, Mn), it was found that the $\frac{Mn}{Fe}$ ratio was between 1,2 and 1,7, with an average of 1,4. The $\frac{Fe+Mn}{Si}$ ratio was found to be >20. The low Si solubility is in agreement with figure 9 on page 13. The solid state of Al_6(Fe, Mn) only can be found in the Al_6Mn rich corner with low amounts of Si present.

In the calculated phase diagrams of the 3103 150% in FactSage, figure 37 page 50, one can not see the development of the primary-Al_6(Fe, Mn) phase. There is a formation of primary Al_6Fe and primary Al_6Mn in the temperature area between [630, 640]°C for Fe [0,04, 25]wt%. In the FTlite database, the metastable Al_6(Fe, Mn) is a prototype phase named Al_6Mn_D2h. It was therefore excluded in the calculations for the 3103 phase diagrams.
Calculations were run in the Equilibrium module for the different Al-Fe-Mn-Mg-Si systems in the 3103 cast from 750 to 200 °C. The results showed no formation of Al6Mn_D2h (Al6(Fe, Mn)).

4.4 Casting

4.4.1 Parallels

There is not enough reproducibility between the different parallels to draw any conclusions on the sequence of alloying elements. The varying amount of alloy compositions might be a result of the different parallel parameters, however the difference in the trials due to broken down equipment introduces many new variables.

There does not seem to be a big difference in the chemical composition of the intermetallic phases phases as a function of the parallel. However this has not been thoroughly investigated in this thesis due to limited time.

4.4.2 Cooling rate

The cooling rate for the rapid solidified disc was not measured. For the slow cooled samples, a cooling rate of 0,1 K/s was measured between 300 and 200°C. This is not representational for the cooling rate between 700 and 300°C.

4.4.3 Additives

For the trails, Fe and Mn were supplied by Hydro. The 80Al-20Mn alloy was first supplied as the source for Mn. These were found not to dissolve properly in the melt, and were in some of the trails found at the bottom of the crucible when emptying the remaining melt. After this was reported to Hydro, a new source of Mn in grain form containing 20% flux was received. The new Mn source seemed to dissolve better in the melt during casting but did increase the amount of dross created in the melt. This is not evident in the spark test results, as seen in figure 57. Further, there seem like the Mn levels in the alloy is in general lower than the target value. This might be due to the formation to dross. The dross from the different trials has not been analyzed. There is not observed any correlations between the dissolution of the additives and the different parallels.

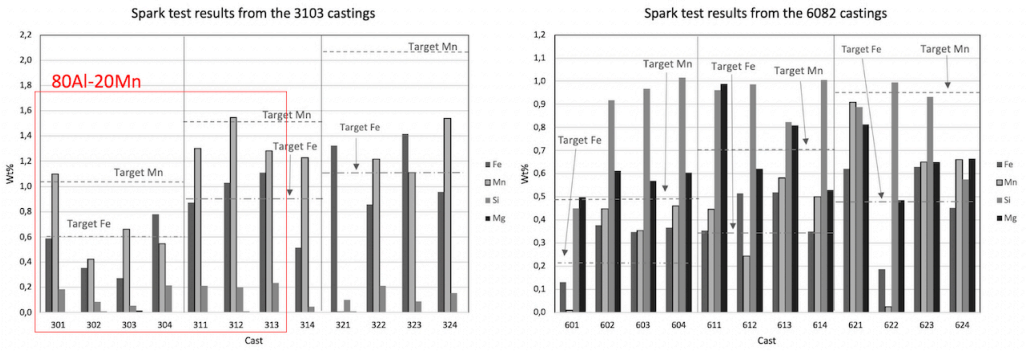

Figure 57: Values from the spark test results. The casting where 80Al-20Mn as an Mn source was used are framed in the red box.

For parallel 2, 3 and 4 the Mn and Fe were to be added cold in the hot melt. Using the grain form 80Fe/Mn-20Flux, the additives were challenging to add. In the industry, these additives are thrown into the oven in lager briquette shaped packages wrapped in Al-foil. This was reproducible on the small scale the trials were conducted. The density of the re-packaging was to low, and if the wrap package was held under the surface of the melt, the force that would be needed would crush the briquettes into powder form. Therefore the large chunks of Mn were selected and honed down to the correct weight according to the weight-calculator. The small additives were then released into the melt near the stirring rod after the slag was cleared from the surface of the melt. This appeared during the trials to create the least amount of dross.

4.4.4 Stirring

For some of the samples (302 and 303), stirring in the melt was done by degassing the melt from the bottom of the crucible. This was found to generate an insufficient amount of flow in the melt as to properly dissolve the additives.

A stainless steel rod with a flat faced propeller was coated with Boron nitrate and connected to a low powered motor. This proved to create a sufficient flow of melt in the crucible.

4.4.5 Degassing

For the first casting a stainless steel degassing rod was used in the melt. The rod was coated with boron nitrate to prevent dissolving in the melt. Due to the limited space in the crucible, there was probably contact between the degassing rod and the stirrer propeller, exposing stainless steel.

A new degassing tool was made from a alumina rod, a ceramic foam-filter and fibrefrax. This held up for the rest of the trails.

4.4.6 Tensile samples

When the first castings were conducted, the copper-moulds used to generate the tensile samples was not acquired yet. The leftover Al-melt from each castings were poured into a cylindrical copper-mould, so it could be stored away as a billet if needed for additional sample-taking. The billets from cast: 301, 302, and 303 were re-melted and used to generate tensile samples for the corresponding alloy. The fact that the alloys were re-melted and casted into tensile samples may have effected their properties relative to the other samples that weren't re-melted. The copper-mould to take the samples was heated up to 600°C to keep the parameters the same for all samples.

Some of the tensile castings from the 200 wt% 6082 broke when separating them from the copper mould. They were very brittle, and can be observed in figure 58. This was probably because of the increased number of intermetallic phases, increasing the amount of casting defects, making the metal more brittle.

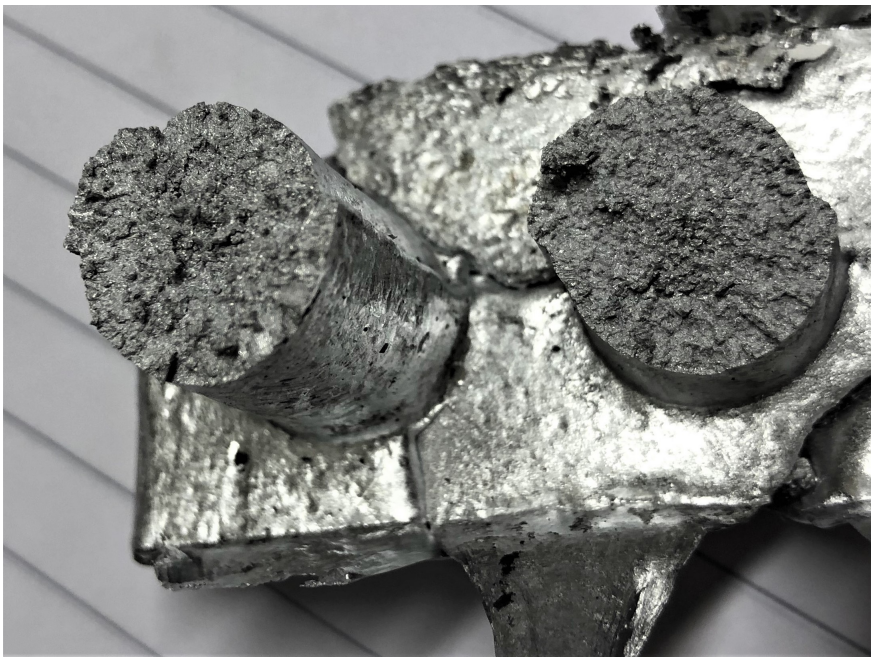

Figure 58: When casting samples for tensile testing, some of the 6082 casts were brittle and could almost be broken by hand.

4.5 Thermodynamic calculations

For the modelling of the phase diagrams, the use of both the Phase diagram and the Equilibrium module were used to calculate the different alloys. For the results shown in the report, there has not been done any adjustments in the data of the FTlite database. The database includes several prototype ternary phases. To what degree these phases occur in real systems is unclear, as there are no experimental findings in the literature.

In the phase diagram module, there is a problem of printing the results in the phase diagram. This has been observed on several different iterations of four phases, or more, on both the binary and ternary diagrams. The program starts do draw phase lines and then deletes them in the final print. The phases can still be distinguished by reading out the different compositions on spots, but it would require a lot of work to manually draw up the line as this would need to be done pixel by pixel. There is no way of getting the code for the print out to see where the error occurs, or where the line should be. Therefore all the phase lines should be considered at best as guidelines. The computation time for the binary diagrams varied from 5 to 30 min depending on the amount of prototypes that were included in the calculations. Once the diagram has been calculated, there seems to be no way of saving the results and open it up later.

The visualization of four-component systems in a binary diagram with temperature and varying compositions is a huge simplification. A better approach would be making ternary diagrams with the addition of the fourth component in the background, allowing calculations with different background levels creating a pyramid. The different pyramids would then need to be correlated with each other and the existing literature.

Late during the thesis, the equilibrium mode was tried for some calculations. The module gives the opportunity to calculate different compositions and the phases that will form and uses the same databases. The results here are possible to save and extract. Several different iterations have to be done to give a good image of the systems. However, one is able to read the calculations and compositions in a much easier way. This mode was unfortunately found to late to be able to utilize properly in the thesis.

Further work: Further work should be put into the calculations for the different alloys. It would be easier to start with the Equilibrium mode to get data on the calculations and compositions in the system. This could then be used for a more refined calculation in the Phase diagram module.

5 Conclusion and further work

The use of spark test results seems to give reasonable indications of the chemical composition of the sample. The Mn values were consistently lower than the targeted values.

Conductivity readings can be used to determine the relative amount of the intermetallic phases and other impurities in different samples from the same alloy. The samples that gave high conductivity readings were also found to be the samples that had the lowest values in the spark test. The samples giving the highest conductivity measurements were also the samples with the least amount of precipitation.

The increase of Mn in (Fe, Mn)-based intermetallic phases leads to a more block-like structure of the precipitations.
The morphology of the intermetallic phases seems to change significantly with only small variations of the composition. Chemical analysis tools should therefor be used to determine the composition of the phases before casting the metal. This is most noticeable in what appears to be the Al_6(Fe, Mn) intermetallic phase. Further work should be done on the formation of the intermetallic phase in the 3103 alloy.

Results from the tensile testing show that an increase in Fe and Mn content in the 3103 alloy leads to a more brittle alloy structure, lowering the σ_y and %EL while increasing the σ_{TS}. The increase of Fe and Mn increased the amount of intermetallic phases, resulting in more casting defects. The 6082 alloy was found to be more brittle and less ductile than the 3103 alloy. The increase of Fe and Mn additions on the 6082 alloy did not lead to a decrease in the elongation as in alloy 3103.

The use of FactSage for modelling the possible intermetallic phases in the 3103 and 6082 alloys might be possible. The Phase diagram module has obviously problems when calculating four or more elements in a binary diagram with varying temperature and composition. For modelling with four elements, a more reasonable approach might be to calculate different ternary diagrams with one background element at fixed temperatures. A range of relevant temperature specific diagrams could then be generated to build a "pyramid" of the phases evolving. The use of Equilibrium module might be a better starting ground for such an approach.

Bibliography

[1] Liu, Z.-K. & Chang, Y. A. 1999. Thermodynamic assessment of the al-fe-si system. *Metallurgical and materials transactions.*, 30(4), 1081–1095.

[2] Taylor, J. A. 2012. Iron-containing intermetallic phases in al-si based casting alloys. *Procedia Materials Science*, 1, 19 – 33. 11th International Congress on Metallurgy Materials SAM/CONAMET 2011. URL: http://www.sciencedirect.com/science/article/pii/S2211812812000053, doi:https://doi.org/10.1016/j.mspro.2012.06.004.

[3] Zolotorevsky, V. S., Belov, N. A., & Glazoff, M. V. 2007. Chapter one - alloying elements and dopants: Phase diagrams. In *Casting Aluminum Alloys*, Zolotorevsky, V. S., Belov, N. A., & Glazoff, M. V., eds, 1 – 93. Elsevier, Amsterdam. URL: http://www.sciencedirect.com/science/article/pii/B9780080453705500031, doi:https://doi.org/10.1016/B978-008045370-5.50003-1.

[4] Zhu, X., Blake, P., & Ji, S. 2018. The formation mechanism of al6(fe, mn) in die-cast al–mg alloys. *CrystEngComm*, 20, 3839–3848. URL: http://dx.doi.org/10.1039/C8CE00675J, doi:10.1039/C8CE00675J.

[5] Liu, Y., Luo, L., Han, C., Ou, L., Wang, J., & Liu, C. 2016. Effect of fe, si and cooling rate on the formation of fe- and mn-rich intermetallics in al-5mg-0.8mn alloy. *Journal Of Materials Science Technology*, 32(4), 305–312.

[6] Taylor, J. A. 2016. The effect of iron in al-si casting alloys. *Cooperative Research Centre for Cast Metals Manufacturing*.

[7] Mondolfo, L. F. 2013. *Aluminum alloys : structure and properties*. Butterworths, London.

[8] RAZAZ, G. & CARLBERG, T. 2019. On the dissolution process of manganese and iron in molten aluminum. *METALLURGICAL AND MATERIALS TRANSACTIONS*, (50).

[9] Callister, C. & Rethwisch, D. 2014. *Materials Science and Engineering*. Wiley, 9th edition.

[10] Figure of a schematic stress-strain curve. https://upload.wikimedia.org/wikipedia/commons/thumb/1/15/StressStrainWEB.svg/800px-StressStrainWEB.svg.png. (Visited 10:48 23st May 2019).

[11] Product figure of struers cutting machine. http://www.aimil.com/products/labotom-15. (Visited 10:26 23th May 2019).

[12] Struers tegramin; preparation system for high-quality specimen preparation. https://www.struers.com/en/Products/Grinding-and-Polishing/Grinding-and-polishing-equipment/Tegramin. (Visited 10:50 23th May 2019).

[13] O. S. I. Fayomi, A. P. I. Popoola, N. E. U. 2017. Effect of alloying element on the integrity and functionality on aluminium-based alloy. *Aluminium alloys*, (13), 244–261.

[14] Received by hydro employee, dr. shahid akhtar. (Received 23th January 2019).

[15] Primary aluminium production. http://www.world-aluminium.org/statistics/#data. (Visited 11:17 23th May 2019).

[16] Aluminum alloys 101. https://www.aluminum.org/resources/industry-standards/aluminum-alloys-101. (Visited 11:06 23th May 2019).

[17] R. S. Rana, R. P. & Da, S. 2012. Reviews on the influences of alloying elements on the microstructure and mechanical properties of aluminum alloys and aluminum alloy composites. *International Journal of Scientific and Research Publications*, 2(6), 1–7.

[18] The differences between heat-treatable and non-heat-treatable aluminum alloys. http://www.alcotec.com/us/en/education/knowledge/qa/The-Differences-Between-Heat-Treatable-and-Non-Heat-Treatable-Aluminum-Alloys.cfm. (Visited 25th February 2019).

[19] B. G. Dietrich, H. Becker, M. S. A. K. A. L. G. W. 2017. Intermetallic sludge formation in fe containingsecondary al–si alloys influenced by cr and mn aspreparative tool for metal melt filtration. *Advanced engineering materials*, 1(19), 1–7.

[20] IBRAHIM, M. F. 2015. Effects of be, sr, fe and mg interactions on the microstructure and mechanical properties of aluminum based aeronautical alloys. 1, 425–439.

[21] Liu, Z.-K. & Chang, Y. A. Apr 1999. Thermodynamic assessment of the al-fe-si system. *Metallurgical and Materials Transactions A*, 30(4), 1081–1095. URL: https://doi.org/10.1007/s11661-999-0160-3, doi:10.1007/s11661-999-0160-3.

[22] Dinnis, C. M., Taylor, J. A., & Dahle, A. K. 2005. As-cast morphology of iron-intermetallics in al–si foundry alloys. *Scripta Materialia*, 53(8), 955 – 958. URL: http://www.sciencedirect.com/science/article/pii/S1359646205003787, doi:https://doi.org/10.1016/j.scriptamat.2005.06.028.

[23] Davis, J. 2001. *Alloying understanding the basics*. S.l.], 1st ed edition. URL: http://portal.igpublish.com/iglibrary/search/ASMIB0000051.html.

[24] Drits, M., Bochvar, N., Kadaner, E., et al. 1977. Diagrammy sostoyaniya sistem na osnove alyuminiya i mag niya: Spravochnoe izdanie (phase diagrams of the aluminum based and magnesium based alloys: Hand book).

[25] Philips, H. 1959. Annotated equilibrium diagrams of some aluminum alloy systems. In *Monogr. No. 25*. Inst. of Metals London.

[26] Belov, N. A., Eskin, D. G., & Aksenov, A. 2014. *Iron in aluminium alloys: impurity and alloying element*. CRC Press.

[27] Q., R. 1992. G. petzow and g. effenberg (eds.): Ternary alloys, a comprehensive compendium of evaluated constitutional data and phase diagrams, vch weinheim. 5, 250–264.

[28] G., G. 1992. G. petzow and g. effenberg (eds.): Ternary alloys, a comprehensive compendium of evaluated constitutional data and phase diagrams, vch weinheim. 5, 394–438.

[29] Zaharov a.m., gul'din i.t., arnol'd a.a., matsenko yu.a. izv. an sssr, metally (no. 3)(1988). 178–181.

[30] Zaharov, A. 1980. Promyshlennye splavy cvetnyh metallov.

[31] Yuong, Du, J. S. F. W. e. a. Metall. trans. a, vol. 35a (2004).

[32] Zaharov a.m., gul'din i.t., arnol'd a.a., matsenko yu.a. izv. an sssr, metally (no. 2)(1988). 90–94.

[33] Zaharov a.m., gul'din i.t., arnol'd a.a., matsenko yu.a. v sb. metallovedenie i obrabotka tsvetnyh splavov, nauka, moscow (1992). 6–17.

[34] Zaharov a.m., gul'din i.t., arnol'd a.a., matsenko yu.a. izv. an sssr, metally (no. 4) (1989). 214–218.

[35] E. Karakösea, M. K. 2009. Effect of solidification rate on the microstructure and microhardness of a melt-spun al–8si–1sb alloy. *Journal of Alloys and Compounds*, (479), 203–236.

[36] A. Verma, S. Kumar, P. G. K. O. 2013. Influence of cooling rate on the fe intermetallic formation in an aa6063 al alloy. *Journal of Alloys and Compounds*, (555), 274–282.

[37] M. Ashby, D. J. 1996. *Engineering Materials 1 An Introduction to their properties and application*. Butterworth, 2nd edition.

[38] Frost, H. J. & Thompson, C. V. 1996. Computer simulation of grain growth. *Current Opinion in Solid State and Materials Science*, 1(3), 361 – 368. URL: http://www.sciencedirect.com/science/article/pii/S135902869680026X, doi:https://doi.org/10.1016/S1359-0286(96)80026-X.

[39] Wakai, F., Enomoto, N., & Ogawa, H. 2000. Three-dimensional microstructural evolution in ideal grain growth—general statistics. *Acta Materialia*, 48(6), 1297 – 1311. URL: http://www.sciencedirect.com/science/article/pii/S135964549900405X, doi:https://doi.org/10.1016/S1359-6454(99)00405-X.

[40] Weygand, D., Bréchet, Y., & Lépinoux, J. 1998. A vertex dynamics simulation of grain growth in two dimensions. *Philosophical Magazine B*, 78(4), 329–352. URL: https://doi.org/10.1080/13642819808206731, doi:10.1080/13642819808206731.

[41] Kamachali, R. Oct 2012. Grain boundary motion in polycrystalline materials. *CALPHAD*.

[42] Factsagetm - frequently asked questions - faq. http://www.crct.polymtl.ca/fact/facthelp/faq.htm#1.1. (Visited 10:45 23th May 2019).

[43] Bale, C. Oct 2009. Factsage thermochemical software and databases - recent developments. *CALPHAD*, 33, 295–311. URL: https://doi.org/10.1016/j.calphad.2008.09.009, doi:10.1016/j.calphad.2008.09.009.

[44] Mallik, A. K. 1986. Computer calculations of phase diagrams. *Bulletin of materials science*, 8(2), 107–121.

[45] Magnusson, T. & Arnberg, L. Oct 2001. Density and solidification shrinkage of hypoeutectic aluminum-silicon alloys. *Metallurgical and Materials Transactions A*, 32(10), 2605–2613. doi:10.1007/s11661-001-0050-9.

[46] Di Sabatino, M. & Arnberg, L. Oct 2009. Castability of aluminium alloys. *Transactions of the Indian Institute of Metals*, 62(4), 321–325. doi:10.1007/s12666-009-0049-2.

[47] Beckermann, C. 2008. *Macrosegregation*. Metals Handbook.

[48] Xu, H., Han, Q., & Meek, T. T. 2008. Effects of ultrasonic vibration on degassing of aluminum alloys. *Materials Science and Engineering: A*, 473(1), 96 – 104. doi:https://doi.org/10.1016/j.msea.2007.04.040.

[49] Standard test methods for tension testing of metallic materials. https://compass.astm.org/EDIT/html_annot.cgi?E8+16a#s00010. (Visited 10:54 23th May 2019).

[50] The international annealed copper standard. https://www.nde-ed.org/GeneralResources/IACS/IACS.htm. (Visited 11:06 24th May 2019).

[51] Hassanabadi, M. 2015. Grain refinement of commercial ec grade 1070 aluminium alloy for electrical application.

[52] Denholm w.t., esdaile j.d., siviour n.g., wilson b.w. metall. trans. a, vol. 15a (no. 7) (1984). 1311–1317.

A Graphs from tensile testing

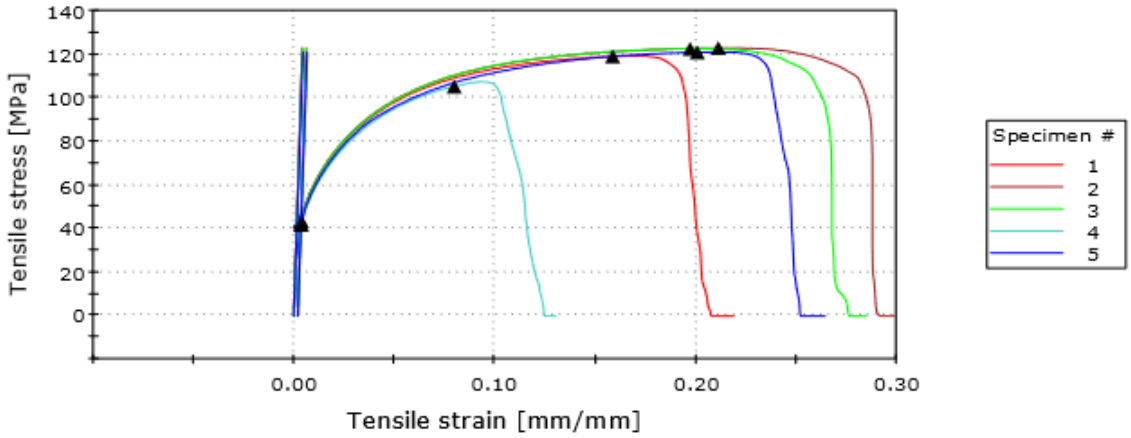

Figure 59: Stress-strain curve for five specimens from cast 301

301	Diameter [mm]	Test rate [mm/min]	Yield [Mpa]	Tensile [Mpa]	Elongation [mm]
1	6,00	5,00	45	119	6,23
2	6,00	5,00	45	123	8,74
3	6,00	5,00	44	123	8,27
4	6,00	5,00	43	107	3,73
5	6,00	5,00	43	122	7,55
Average	**6,00**	**5,00**	**44**	**118,8**	**6,90**

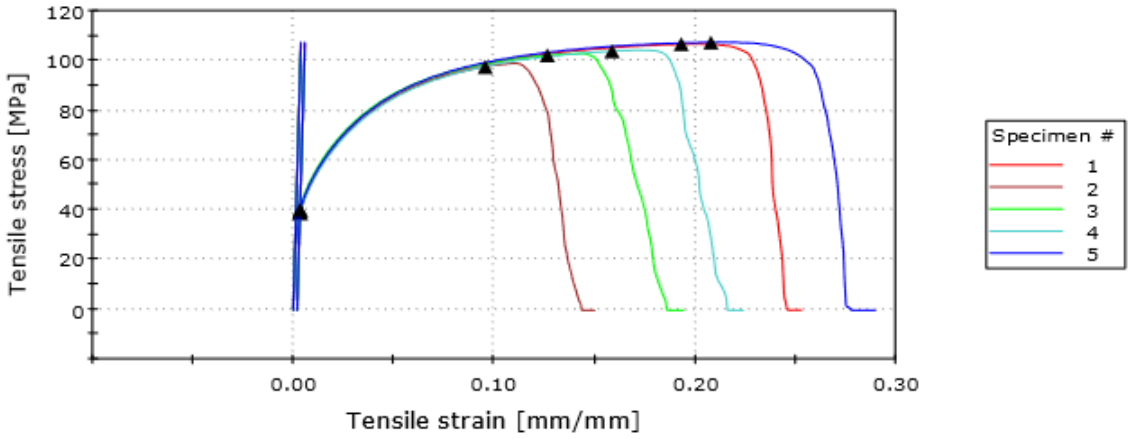

Figure 60: Stress-strain curve for five specimens from cast 302

302	Diameter [mm]	Test rate [mm/min]	Yield [Mpa]	Tensile [Mpa]	Elongation [mm]
1	6,00	5,00	40	107	7,36
2	6,00	5,00	40	99	4,29
3	6,00	5,00	41	103	5,56
4	6,00	5,00	40	104	6,47
5	6,00	5,00	41	107	8,32
Average	**6,00**	**5,00**	**40,4**	**104**	**6,4**

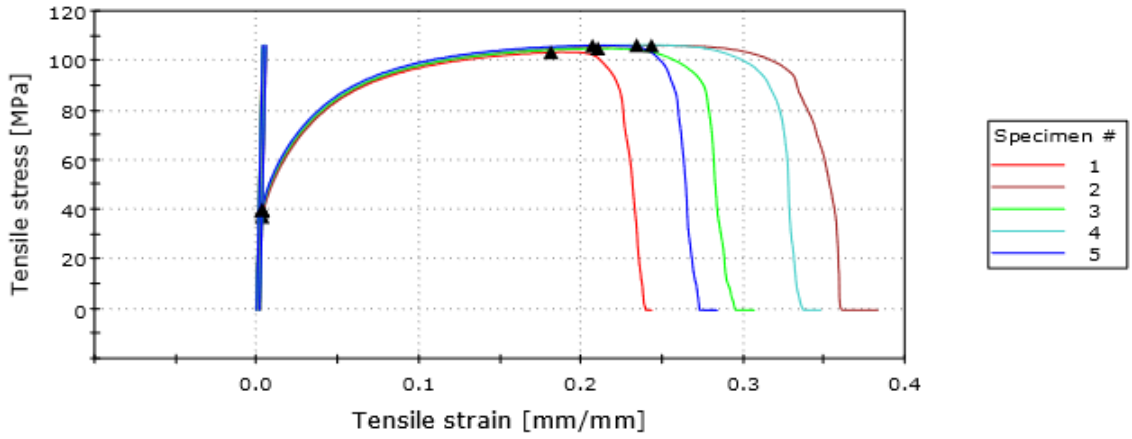

Figure 61: Stress-strain curve for five specimens from cast 303

303	Diameter [mm]	Test rate [mm/min]	Yield [Mpa]	Tensile [Mpa]	Elongation [mm]
1	6,00	5,00	41	103	7,18
2	6,00	5,00	38	106	10,8
3	6,00	5,00	41	105	8,84
4	6,00	5,00	41	106	10,09
5	6,00	5,00	41	106	8,17
Average	**6,00**	**5,00**	**40,4**	**105,2**	**9,02**

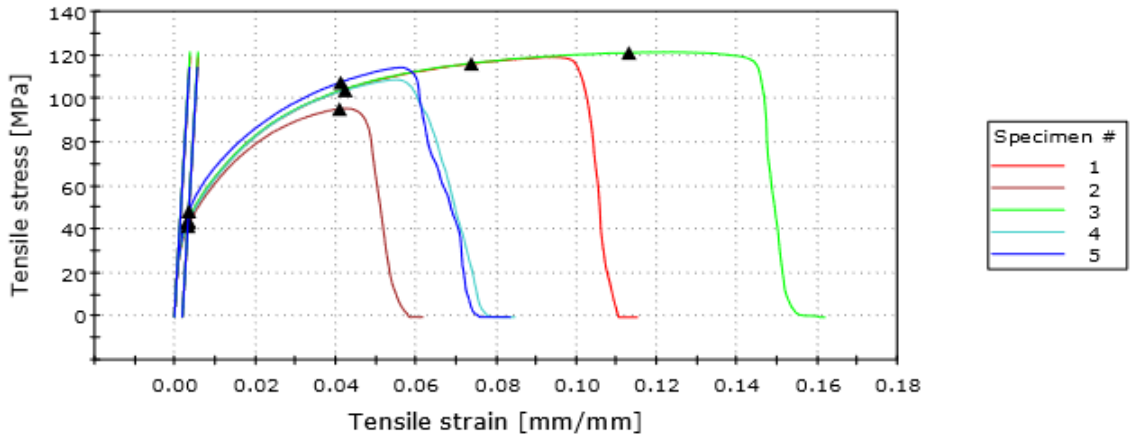

Figure 62: Stress-strain curve for five specimens from cast 313

313	Diameter [mm]	Test rate [mm/min]	Yield [Mpa]	Tensile [Mpa]	Elongation [mm]
1	6,00	5,00	45	119	3,3
2	6,00	5,00	43	96	1,74
3	6,00	5,00	45	121	4,79
4	6,00	5,00	44	109	2,36
5	6,00	5,00	49	114	2,26
Average	**6,00**	**5,00**	**45,2**	**111,8**	**2,89**

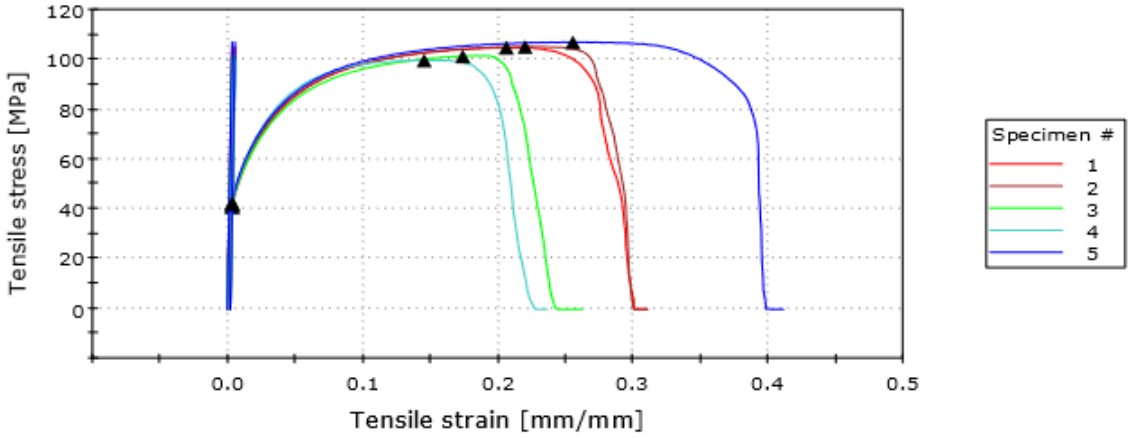

Figure 63: Stress-strain curve for five specimens from cast 314

314	Diameter [mm]	Test rate [mm/min]	Yield [Mpa]	Tensile [Mpa]	Elongation [mm]
1	6,00	5,00	42	105	9,02
2	6,00	5,00	43	105	9
3	6,00	5,00	42	101	7,31
4	6,00	5,00	43	100	6,8
5	6,00	5,00	43	107	11,93
Average	**6,00**	**5,00**	**42,6**	**103,6**	**8,81**

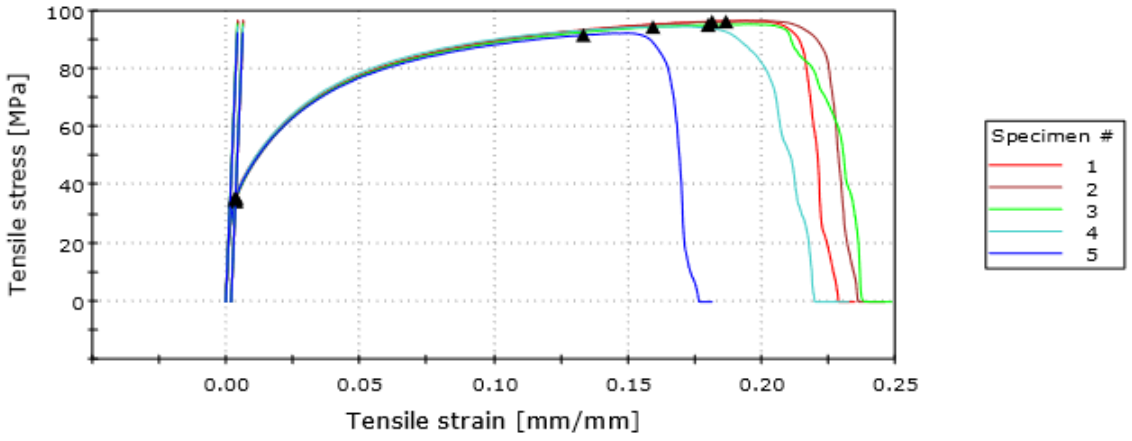

Figure 64: Stress-strain curve for five specimens from cast 321

321	Diameter [mm]	Test rate [mm/min]	Yield [Mpa]	Tensile [Mpa]	Elongation [mm]
1	6,00	5,00	37	96	6,86
2	6,00	5,00	36	97	7,07
3	6,00	5,00	36	95	7,16
4	6,00	5,00	37	95	6,59
5	6,00	5,00	36	92	5,29
Average	**6,00**	**5,00**	**36,4**	**95**	**6,60**

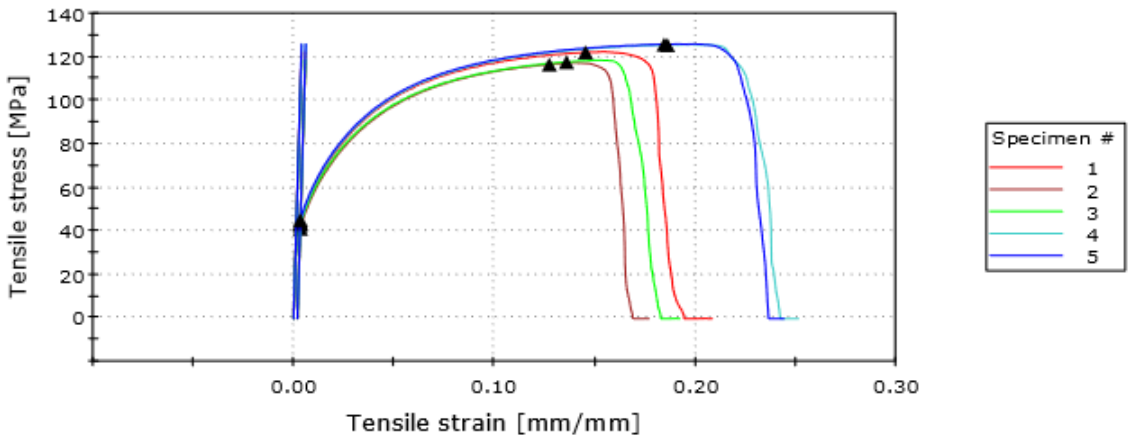

Figure 65: Stress-strain curve for five specimens from cast 322

322	Diameter [mm]	Test rate [mm/min]	Yield [Mpa]	Tensile [Mpa]	Elongation [mm]
1	6,00	5,00	44	122	5,82
2	6,00	5,00	42	117	5,06
3	6,00	5,00	44	118	5,47
4	6,00	5,00	45	126	7,26
5	6,00	5,00	46	126	7,08
Average	**6,00**	**5,00**	**44,2**	**121,8**	**6,14**

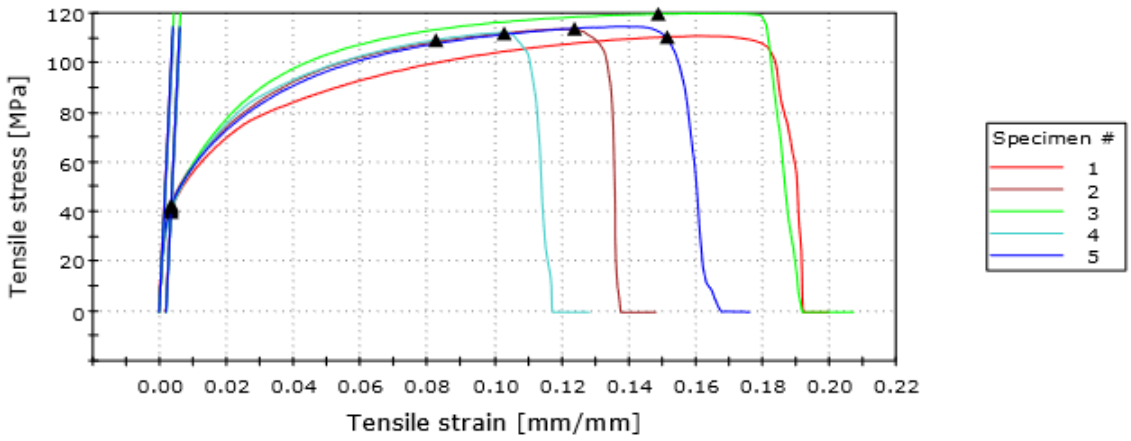

Figure 66: Stress-strain curve for five specimens from cast 323

323	Diameter [mm]	Test rate [mm/min]	Yield [Mpa]	Tensile [Mpa]	Elongation [mm]
1	6,00	5,00	41	111	5,74
2	6,00	5,00	44	114	4,12
3	6,00	5,00	42	121	5,75
4	6,00	5,00	41	112	3,51
5	6,00	5,00	43	115	5,05
Average	**6,00**	**5,00**	**42,2**	**114,6**	**4,83**

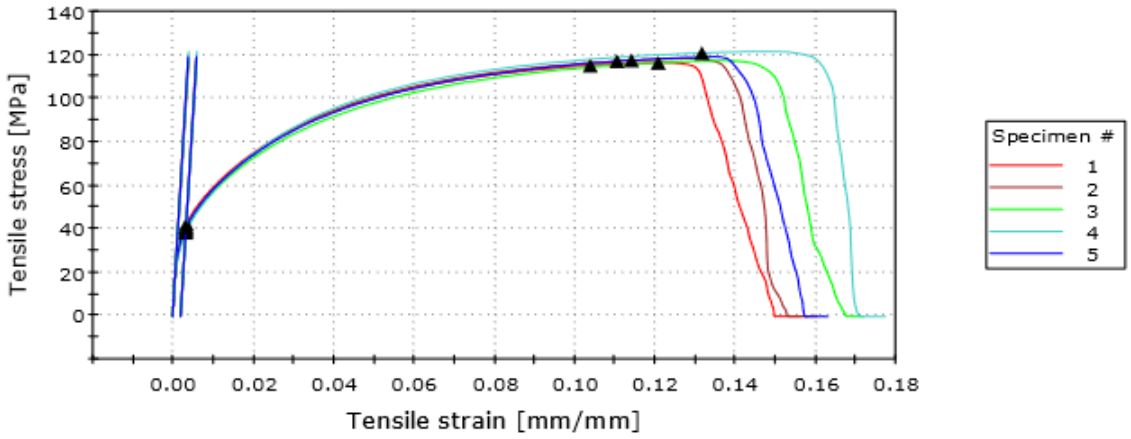

Figure 67: Stress-strain curve for five specimens from cast 324

324	Diameter [mm]	Test rate [mm/min]	Yield [Mpa]	Tensile [Mpa]	Elongation [mm]
1	6,00	5,00	43	117	4,48
2	6,00	5,00	41	118	4,58
3	6,00	5,00	41	117	5,01
4	6,00	5,00	39	121	5,11
5	6,00	5,00	42	119	4,71
Average	**6,00**	**5,00**	**41,2**	**118,4**	**4,78**

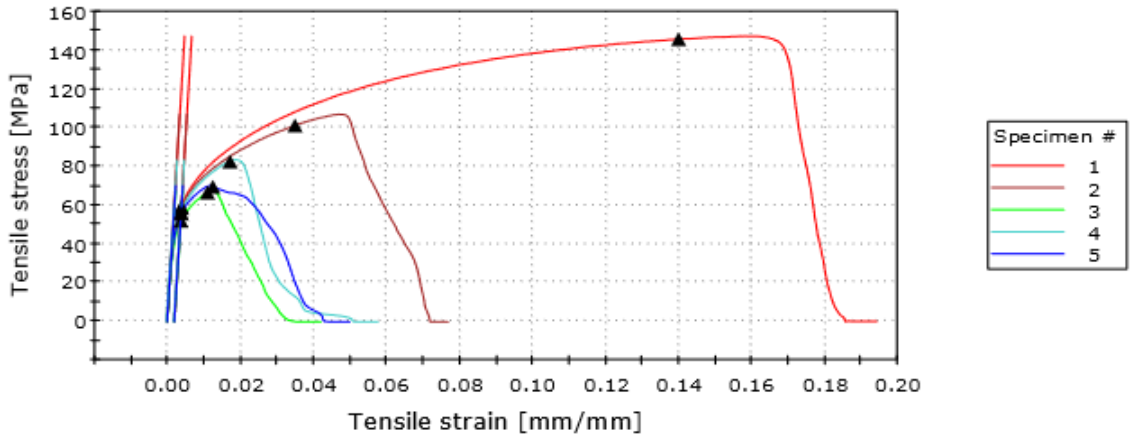

Figure 68: Stress-strain curve for five specimens from cast 601

601	Diameter [mm]	Test rate [mm/min]	Yield [Mpa]	Tensile [Mpa]	Elongation [mm]
1	6,00	5,00	60	147	5,72
2	6,00	5,00	60	107	2,15
3	6,00	5,00	53	68	1,05
4	6,00	5,00	57	83	1,5
5	6,00	5,00	57	71	1,31
Average	**6,00**	**5,00**	**57,4**	**95,2**	**2,35**

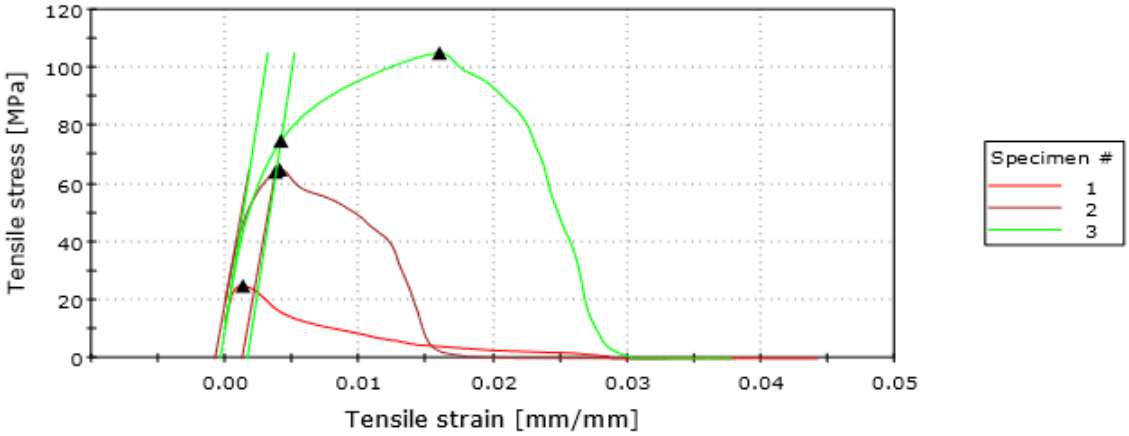

Figure 69: Stress-strain curve for three specimens from cast 602

602	Diameter [mm]	Test rate [mm/min]	Yield [Mpa]	Tensile [Mpa]	Elongation [mm]
1	6,00	5,00	—	—	—
2	6,00	5,00	65	64	0,59
3	6,00	5,00	76	106	0,9
4	6,00	5,00	—	—	—
5	6,00	5,00	—	—	—
Average	**6,00**	**5,00**	**—**	**—**	**—**

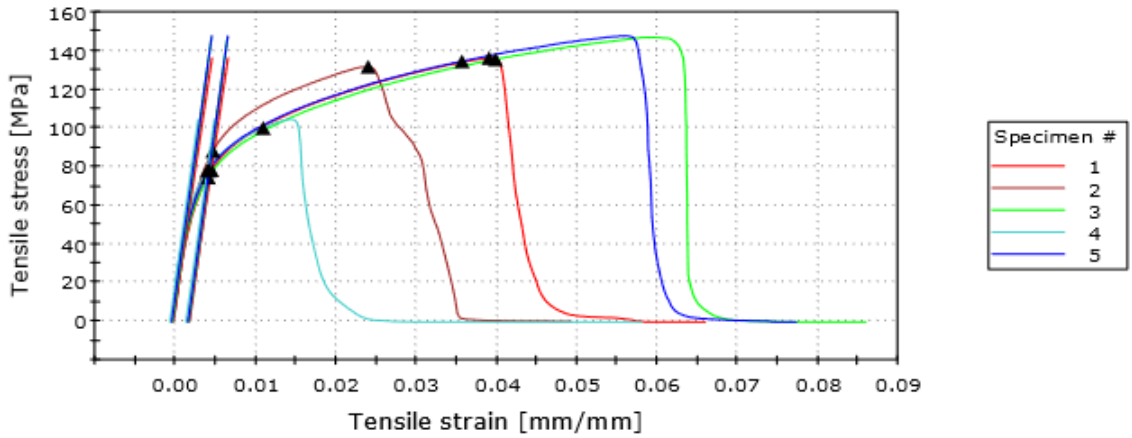

Figure 70: Stress-strain curve for five specimens from cast 603

603	Diameter [mm]	Test rate [mm/min]	Yield [Mpa]	Tensile [Mpa]	Elongation [mm]
1	6,00	5,00	79	136	1,75
2	6,00	5,00	89	132	1,47
3	6,00	5,00	76	148	2,24
4	6,00	5,00	79	105	0,89
5	6,00	5,00	79	147	2,18
Average	**6,00**	**5,00**	**80,4**	**133,6**	**1,71**

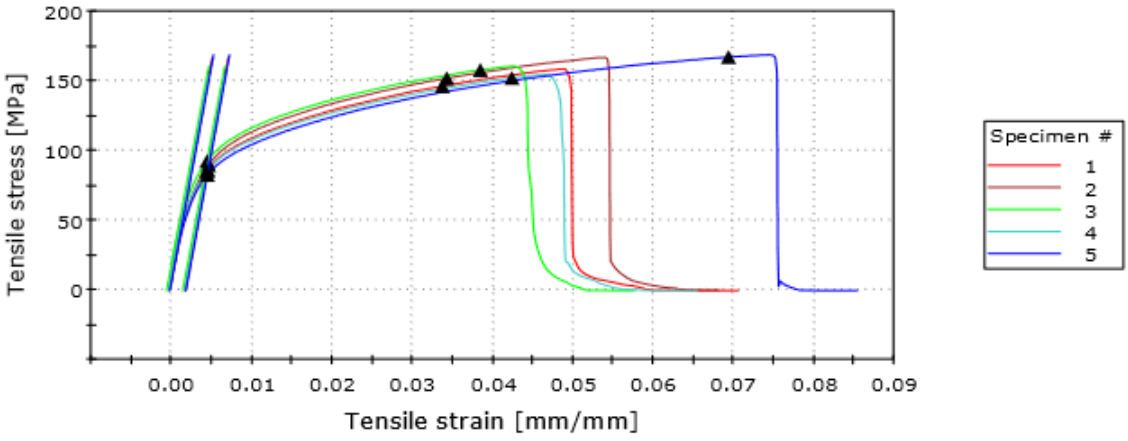

Figure 71: Stress-strain curve for five specimens from cast 604

604	Diameter [mm]	Test rate [mm/min]	Yield [Mpa]	Tensile [Mpa]	Elongation [mm]
1	6,00	5,00	87	158	2,12
2	6,00	5,00	91	167	2,04
3	6,00	5,00	94	160	1,73
4	6,00	5,00	87	154	1,78
5	6,00	5,00	84	169	2,35
Average	**6,00**	**5,00**	**88,6**	**161,6**	**2,00**

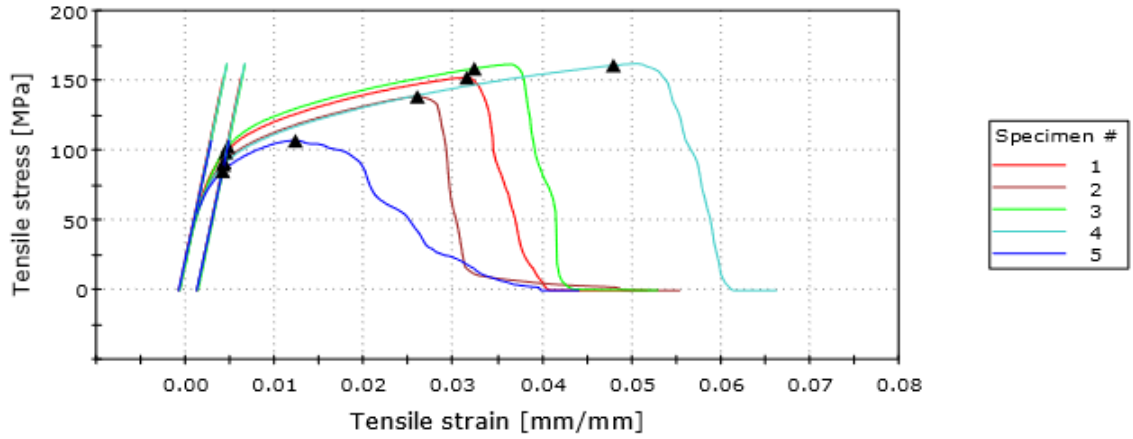

Figure 72: Stress-strain curve for five specimens from cast 611

611	Diameter [mm]	Test rate [mm/min]	Yield [Mpa]	Tensile [Mpa]	Elongation [mm]
1	6,00	5,00	100	152	1,22
2	6,00	5,00	93	139	1,46
3	6,00	5,00	104	161	1,44
4	6,00	5,00	91	162	1,83
5	6,00	5,00	86	107	1,19
Average	**6,00**	**5,00**	**94,8**	**144,2**	**1,43**

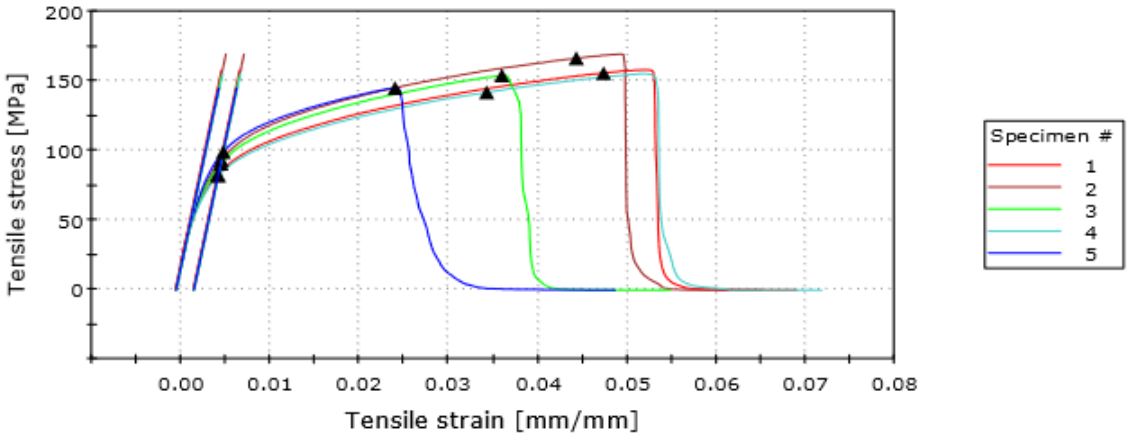

Figure 73: Stress-strain curve for five specimens from cast 612

612	Diameter [mm]	Test rate [mm/min]	Yield [Mpa]	Tensile [Mpa]	Elongation [mm]
1	6,00	5,00	83	157	1,76
2	6,00	5,00	94	169	1,66
3	6,00	5,00	91	153	1,29
4	6,00	5,00	83	155	1,83
5	6,00	5,00	100	145	1,1
Average	**6,00**	**5,00**	**90,2**	**155,8**	**1,53**

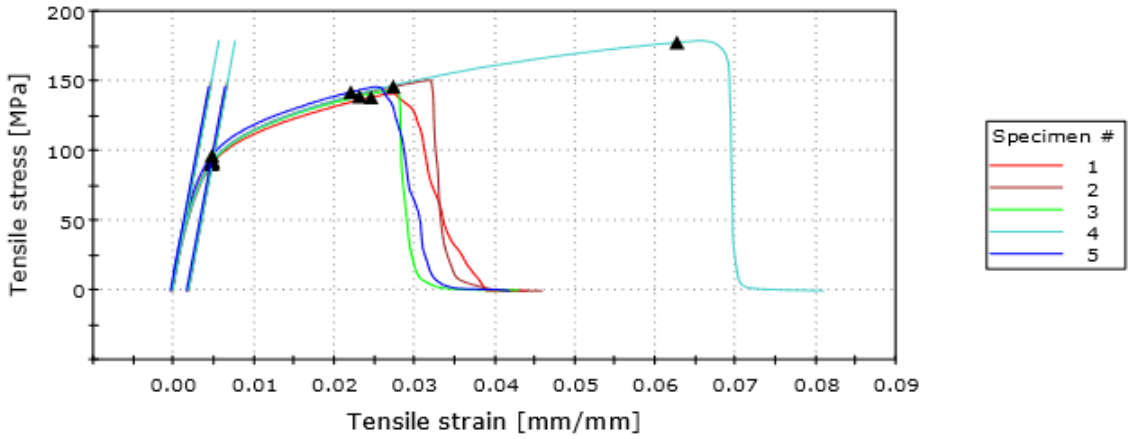

Figure 74: Stress-strain curve for five specimens from cast 613

613	Diameter [mm]	Test rate [mm/min]	Yield [Mpa]	Tensile [Mpa]	Elongation [mm]
1	6,00	5,00	91	141	1,16
2	6,00	5,00	92	151	1,23
3	6,00	5,00	92	144	1,28
4	6,00	5,00	94	178	2,25
5	6,00	5,00	97	146	1,23
Average	**6,00**	**5,00**	**93,2**	**152**	**1,43**

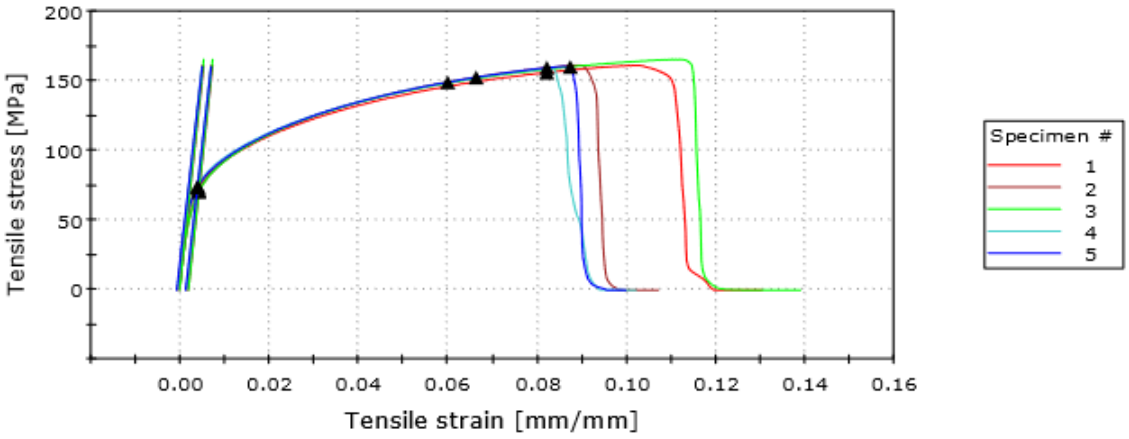

Figure 75: Stress-strain curve for five specimens from cast 614

614	Diameter [mm]	Test rate [mm/min]	Yield [Mpa]	Tensile [Mpa]	Elongation [mm]
1	6,00	5,00	74	161	3,57
2	6,00	5,00	72	161	2,94
3	6,00	5,00	71	165	3,7
4	6,00	5,00	75	158	2,86
5	6,00	5,00	75	160	2,85
Average	**6,00**	**5,00**	**73,4**	**161**	**3,18**

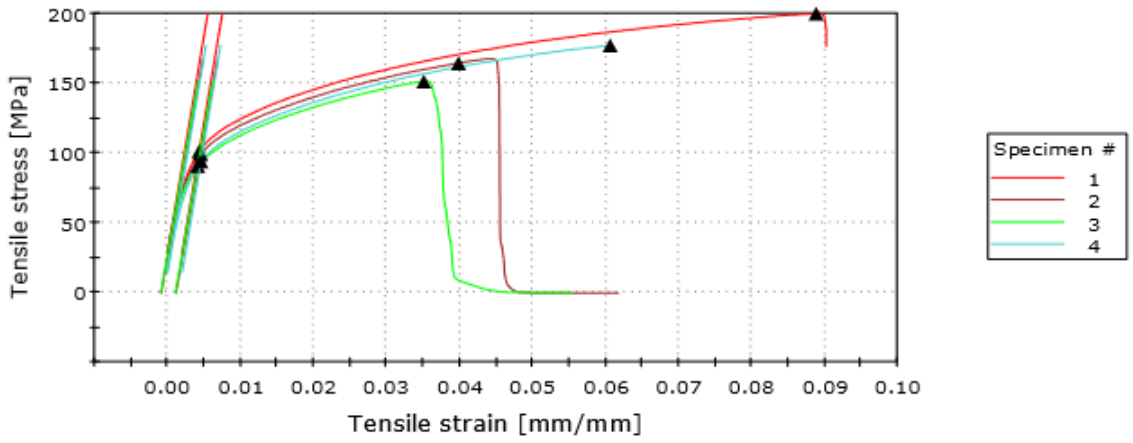

Figure 76: Stress-strain curve for three specimens from cast 621

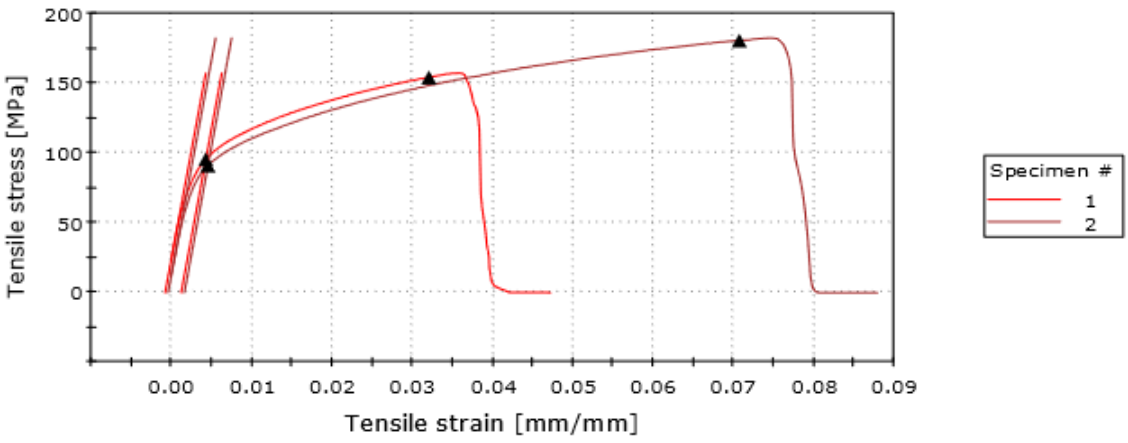

Figure 77: Stress-strain curve for two specimens from cast 621

621	Diameter [mm]	Test rate [mm/min]	Yield [Mpa]	Tensile [Mpa]	Elongation [mm]
1	6,00	5,00	102	200	2,7
2	6,00	5,00	100	167	1,49
3	6,00	5,00	92	151	1,6
4	6,00	5,00	96	157	1,38
5	6,00	5,00	92	182	2,4
Average	**6,00**	**5,00**	**96,4**	**171,4**	**1,91**

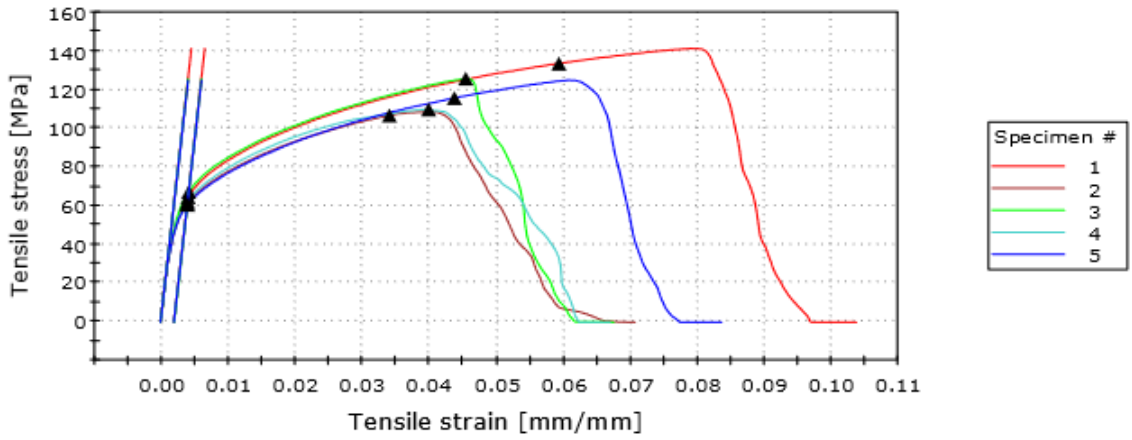

Figure 78: Stress-strain curve for five specimens from cast 622

622	Diameter [mm]	Test rate [mm/min]	Yield [Mpa]	Tensile [Mpa]	Elongation [mm]
1	6,00	5,00	66	141	2,9
2	6,00	5,00	62	109	2,07
3	6,00	5,00	68	126	2
4	6,00	5,00	63	110	1,86
5	6,00	5,00	62	125	2,31
Average	**6,00**	**5,00**	**64,2**	**122,2**	**2,23**

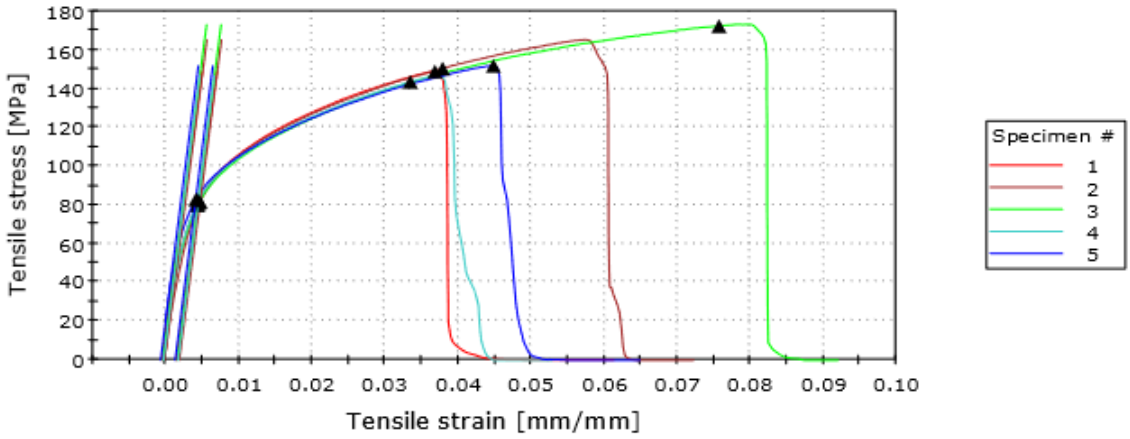

Figure 79: Stress-strain curve for five specimens from cast 623

623	Diameter [mm]	Test rate [mm/min]	Yield [Mpa]	Tensile [Mpa]	Elongation [mm]
1	6,00	5,00	82	149	1,84
2	6,00	5,00	83	165	2
3	6,00	5,00	81	173	2,63
4	6,00	5,00	83	145	1,34
5	6,00	5,00	84	152	1,64
Average	**6,00**	**5,00**	**82,6**	**156,8**	**1,89**

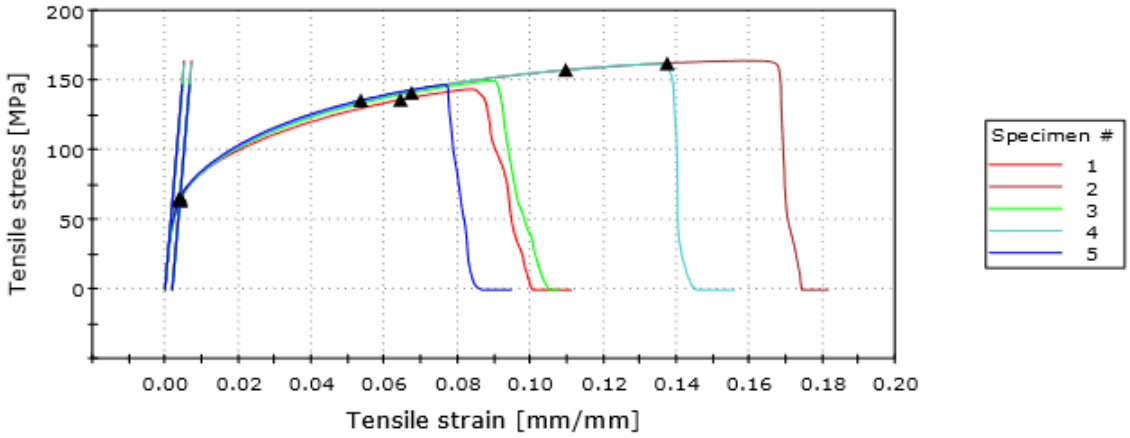

Figure 80: Stress-strain curve for five specimens from cast 624

624	Diameter [mm]	Test rate [mm/min]	Yield [Mpa]	Tensile [Mpa]	Elongation [mm]
1	6,00	5,00	68	144	3
2	6,00	5,00	65	164	5,22
3	6,00	5,00	65	149	3,14
4	6,00	5,00	65	161	4,35
5	6,00	5,00	66	147	2,59
Average	**6,00**	**5,00**	**65,8**	**153**	**3,66**

B Castings

Batch	Al	Fe	Mn	Si	Mg	Cu	Cr	Zn	Ti	Ni	Notes
301	2305,6	14,1	25,5	3,5	0,7	0,2	0,7	0,7	0,5	0,2	No stirring because of problems with the stirrer, holding time of 40 min to compensate for lack of convection
302	2283,9	14,1	25,4	3,5	0,7	0,2	0,7	0,7	0,5	0,2	A lot of slag, ca. 5g of Mn did not dissolve. Still problems with the stirrer, so degassing rod was used as a stirrer. Holding time 20 min
303	2291,0	14,1	25,5	3,5	0,7	0,2	0,7	0,7	0,5	0,2	Still stirring by degassing, holding time 20 min
304	2023,4	12,4	22,3	3,1	0,6	0,2	0,65	0,6	0,4	0,2	New stirrer that works, holding time 20 min
311	2318,5	26,8	38,6	3,5	0,7	0,2	0,7	0,7	0,5	0,2	Problems with dissolving the Mn, a lot of slag. Very dry powder that won't dissolve
312	2378,5	25,4	36,6	3,6	0,7	0,2	0,7	0,7	0,5	0,2	Prewarming the Mn to 650 deg. because it takes so long to dissolve in the Al-melt
313	2392,2	25,8	39,9	3,7	0,7	0,2	0,7	0,7	0,5	0,2	Takes Mn additions 50 min to solve in the Al when cold Mn is added to melt
314	2179,8	23,2	36,3	3,4	0,7	0,2	0,7	0,7	0,4	0,2	Received new Mn with flux from Hydro that is much easier to dissolve. Holding time 20 min
321	2186,3	34,0	49,0	3,4	0,7	0,2	0,7	0,7	0,5	0,2	New Mn dissolves completely and no signs of undissolved Mn in the bottom of the crucible
322	2095,5	32,6	45,3	3,3	0,7	0,2	0,7	0,7	0,4	0,2	
323	2186,4	33,4	48,9	3,4	0,7	0,2	0,7	0,7	0,5	0,2	
324	2253,6	35,3	48,2	3,5	0,7	0,2	0,7	0,7	0,5	0,2	

Batch	Al	Fe	Mn	Si	Mg	Cu	Cr	Zn	Ti	Notes
601	2226,8	5,4	11,2	21,9	15,5	0,9	3,4	1,1	1,1	Melt seems ok, easier to work with than the 3xxx-series.
602	2026,2	5,0	10,2	19,8	14,1	0,8	3,1	1,0	1,0	Not much dross on this cast, but some slag. Very viscous, not so easy to pour.
603	2055,4	5,1	10,3	20,0	14,6	0,8	3,2	1,1	1,0	Added 100-200g blocks of Al instead of 1kg's. When the Mn was added a lot of slag-powder developed. When adding Mg the dross-formation increased.
604	2170,8	5,3	11,0	21,2	15,2	0,9	3,3	1,1	1,0	When pouring the samples for the tensile tests some of the samples broke, seems brittle
611	2149,4	8,0	16,2	21,0	15,1	0,9	3,3	1,1	1,0	Very thick dross, and the metal is hard to pour. Not to much slag at the bottom of the crucible
612	2081,1	7,8	15,8	20,4	14,6	0,8	3,2	1,1	1,1	Some undissolved parts before we added the Fe. Mn additions stuck along the edge of the melt. Mg dissolved quickly, but seemed to increase the amount of dross created in the surface
613	2155,6	8,1	16,3	21,1	15,1	0,9	3,3	1,1	1,1	Same amount of dross as seen in the earlier 6xxx-castings. Hard to pour
614	1980,5	7,4	15,0	19,4	13,8	0,8	3,1	1,0	1,0	Low viscosity, unknown quality of the tensile samples. Several of the tensile castings broke during cleaning
621	2003,0	10,0	20,3	19,7	14,1	0,8	3,1	1,0	1,0	
622	2083,9	10,3	21,1	20,5	14,7	0,8	3,2	1,1	1,0	
623	2049,3	10,2	20,8	20,1	14,4	0,8	3,2	1,1	1,1	Same amount of slag as earlier, total holding time was a bit longer than the goal
624	1933,7	9,6	19,6	19,0	13,6	0,8	3,0	1,0	1,0	More viscous than the other 6xxx-casts from the 150% and 200% Fe and Mn content

C 3103 SEM picture

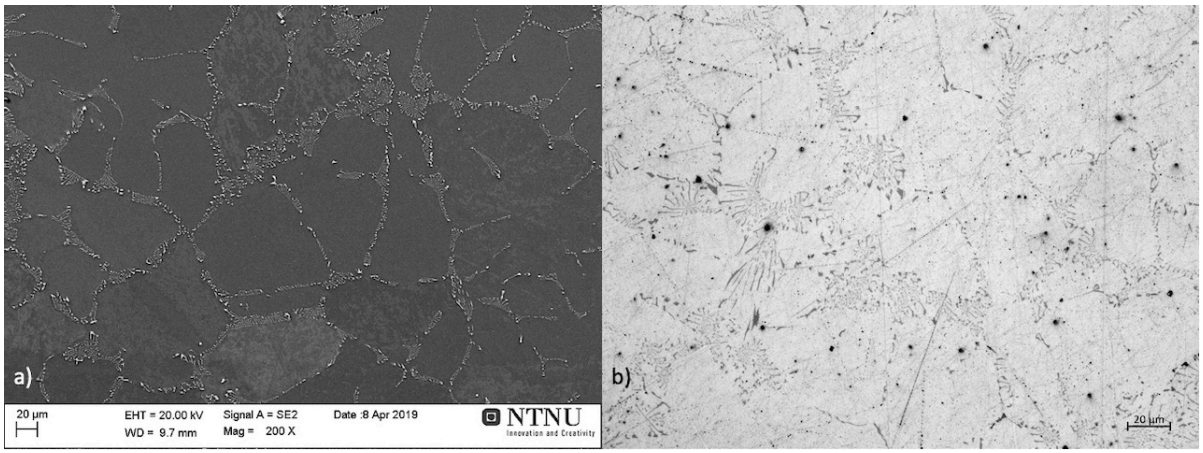

Figure 81: Pictures of the microstructure in cast 301; a) SEM picture of the slow cooled sample and b) LMI of the rapid solidified sample.

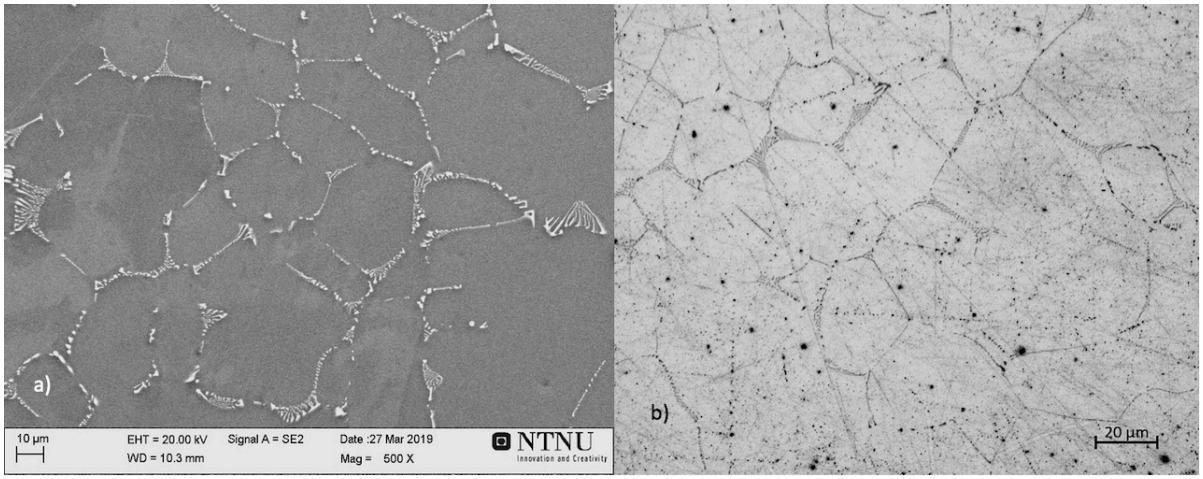

Figure 82: Pictures of the microstructure in cast 302; a) SEM picture of the slow cooled sample and b) LMI of the rapid solidified sample.

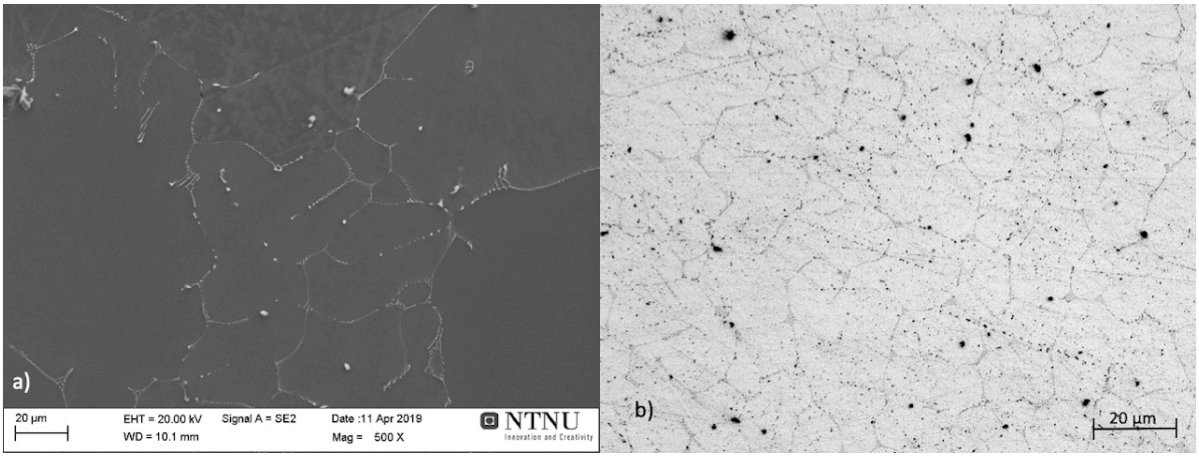

Figure 83: Pictures of the microstructure in cast 303; a) SEM picture of the slow cooled sample and b) LMI of the rapid solidified sample.

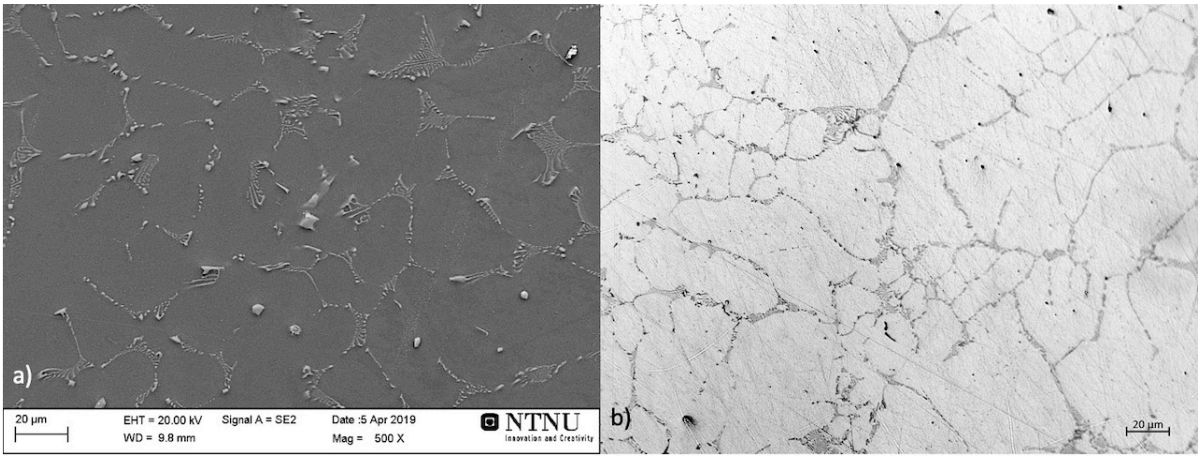

Figure 84: Pictures of the microstructure in cast 304; a) SEM picture of the slow cooled sample and b) LMI of the rapid solidified sample.

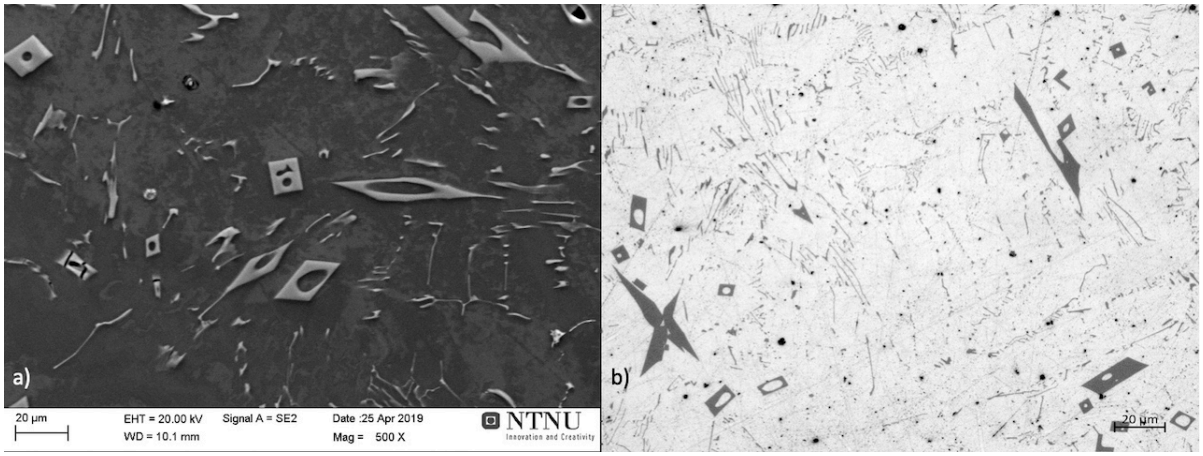

Figure 85: Pictures of the microstructure in cast 311; a) SEM picture of the slow cooled sample and b) LMI of the rapid solidified sample.

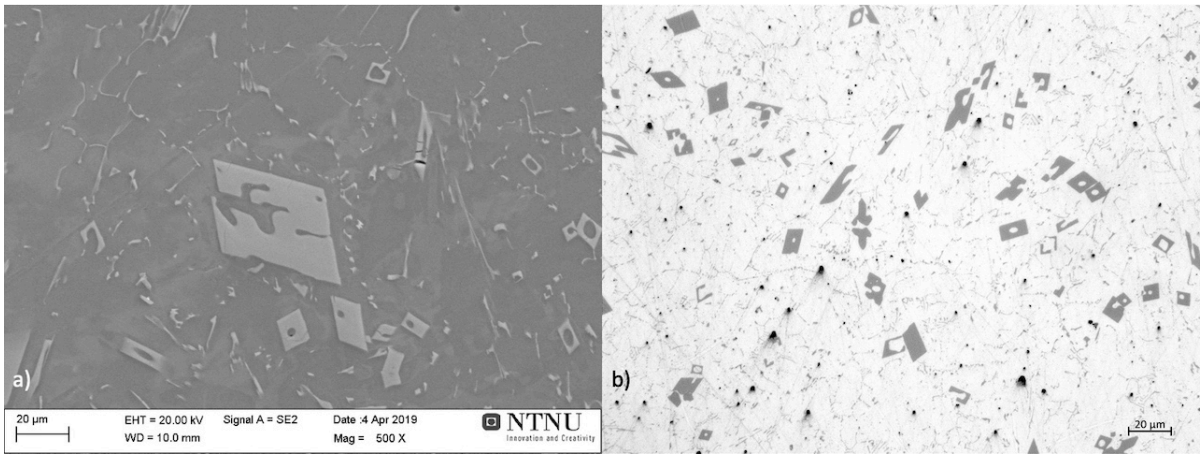

Figure 86: Pictures of the microstructure in cast 312; a) SEM picture of the slow cooled sample and b) LMI of the rapid solidified sample.

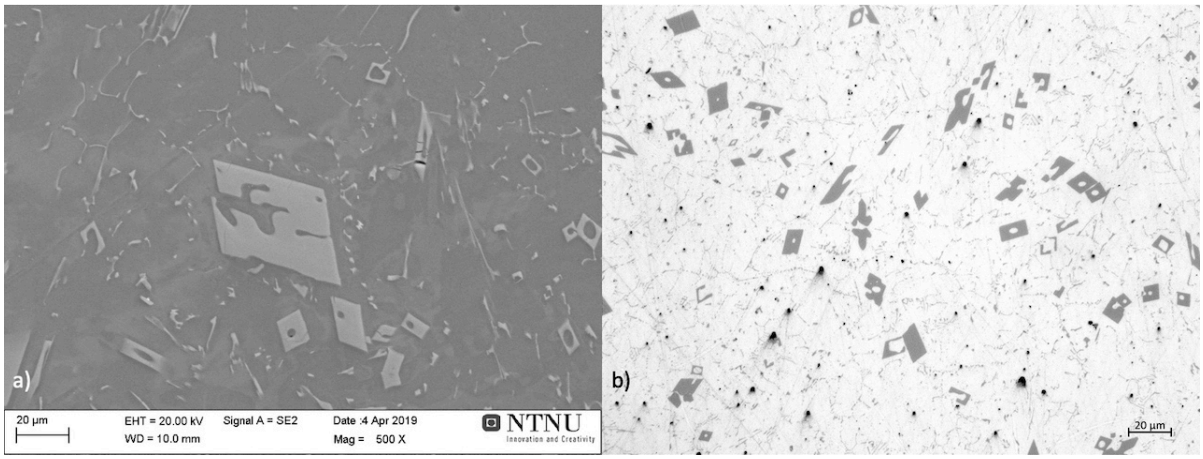

Figure 87: Pictures of the microstructure in cast 312; a) SEM picture of the slow cooled sample and b) LMI of the rapid solidified sample.

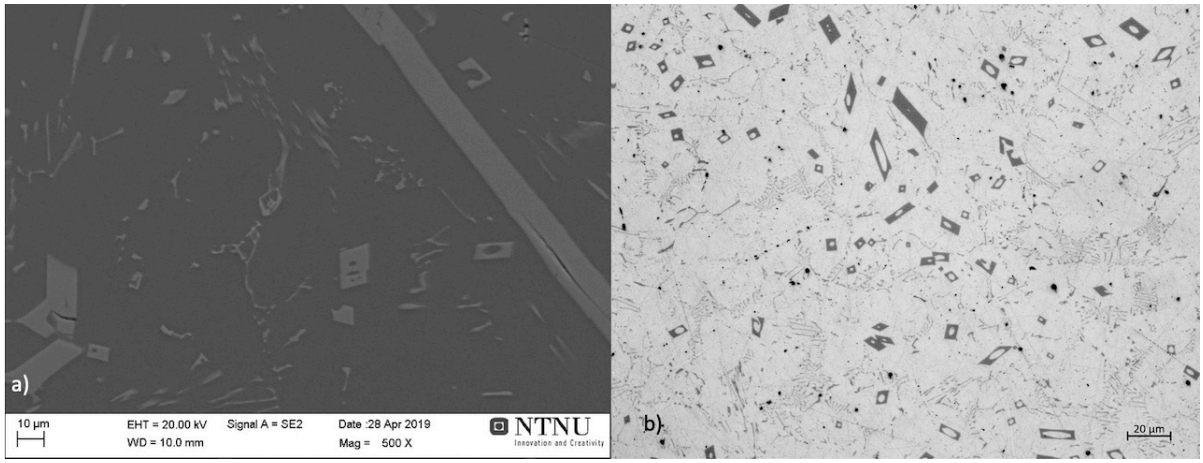

Figure 88: Pictures of the microstructure in cast 313; a) SEM picture of the slow cooled sample and b) LMI of the rapid solidified sample.

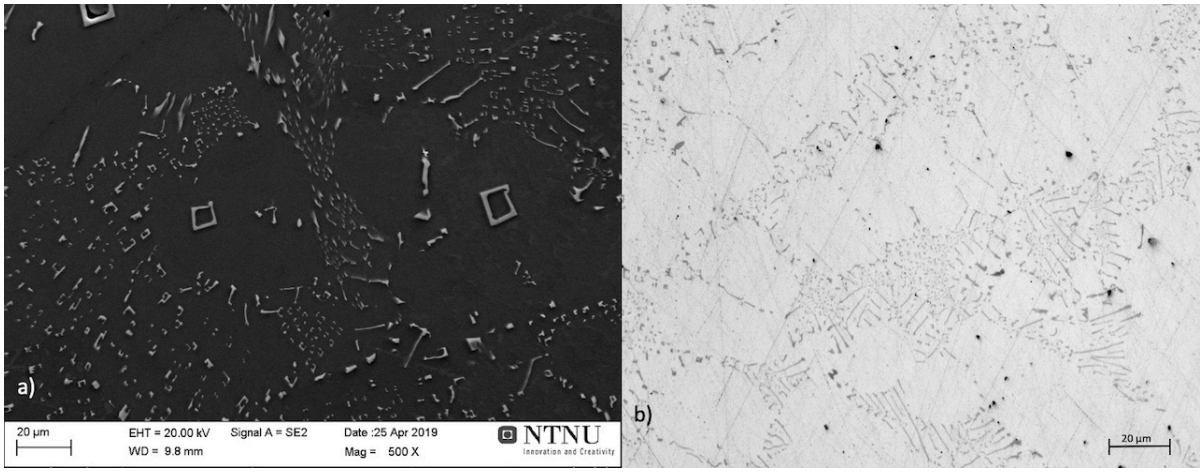

Figure 89: Pictures of the microstructure in cast 314; a) SEM picture of the slow cooled sample and b) LMI of the rapid solidified sample.

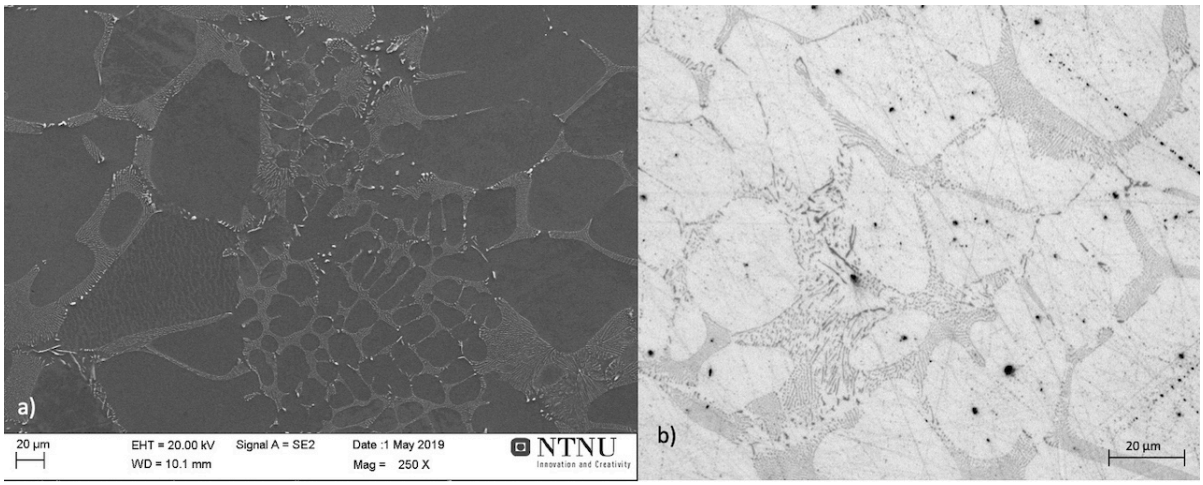

Figure 90: Pictures of the microstructure in cast 321; a) SEM picture of the slow cooled sample and b) LMI of the rapid solidified sample.

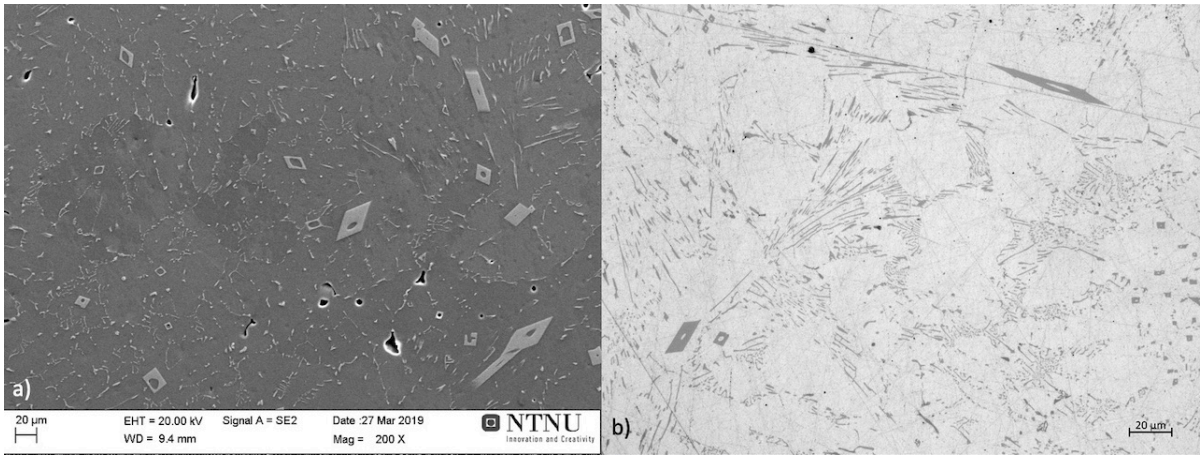

Figure 91: Pictures of the microstructure in cast 322; a) SEM picture of the slow cooled sample and b) LMI of the rapid solidified sample.

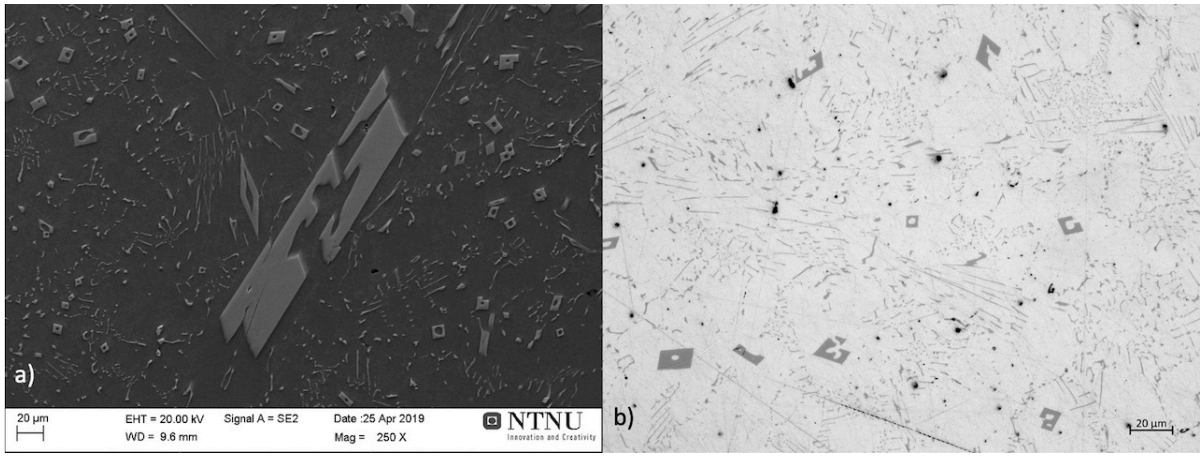

Figure 92: Pictures of the microstructure in cast 323; a) SEM picture of the slow cooled sample and b) LMI of the rapid solidified sample.

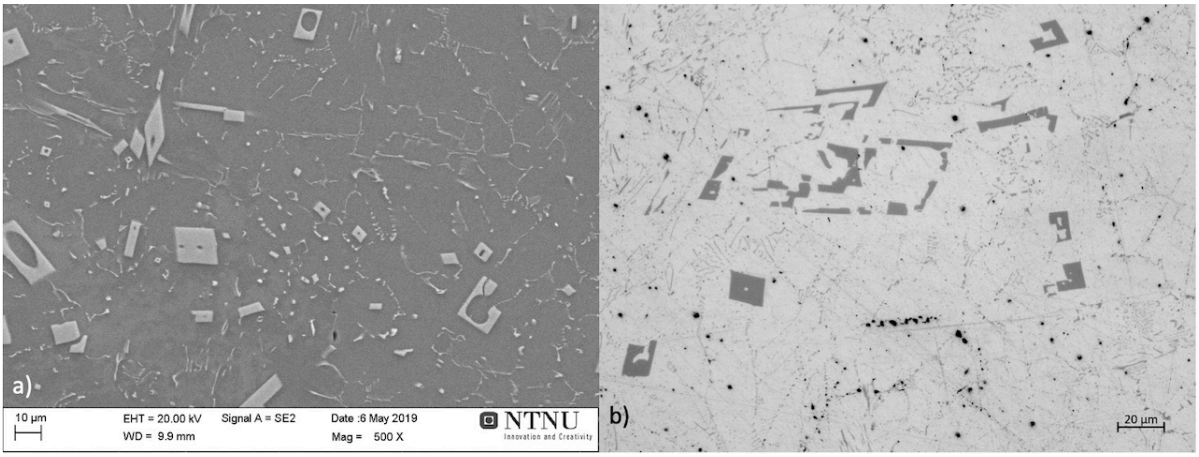

Figure 93: Pictures of the microstructure in cast 324; a) SEM picture of the slow cooled sample and b) LMI of the rapid solidified sample.

D 6082 SEM picture

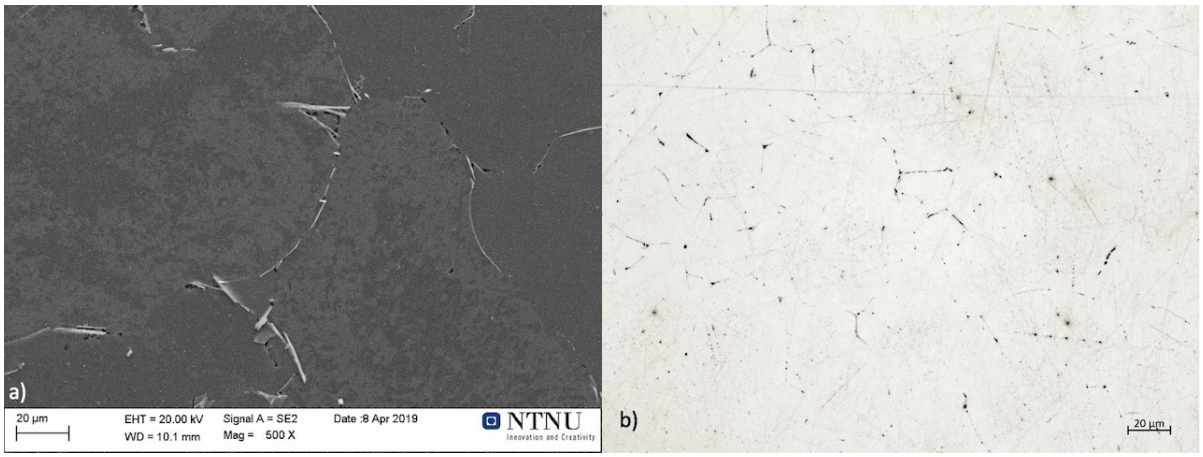

Figure 94: Pictures of the microstructure in cast 601; a) SEM picture of the slow cooled sample and b) LMI of the rapid solidified sample.

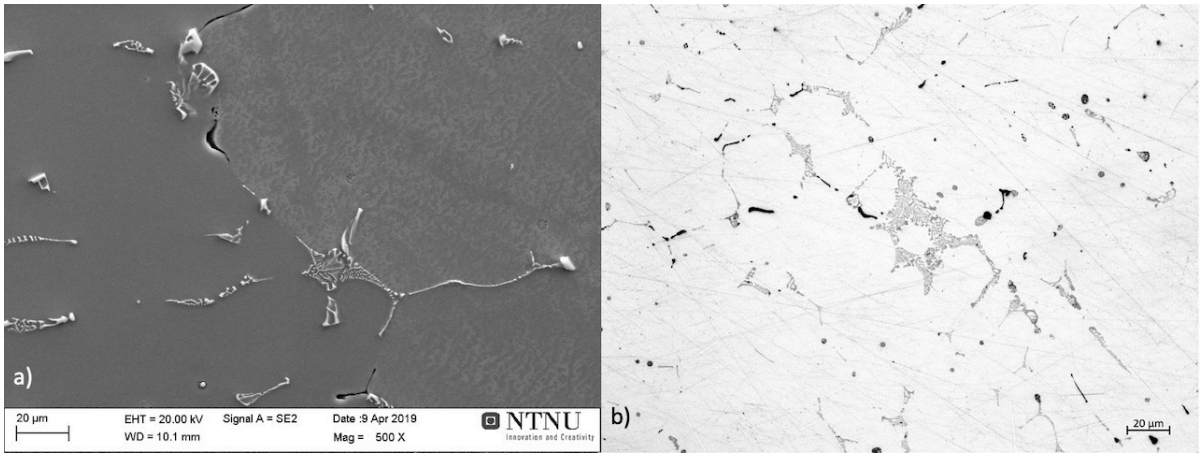

Figure 95: Pictures of the microstructure in cast 602; a) SEM picture of the slow cooled sample and b) LMI of the rapid solidified sample.

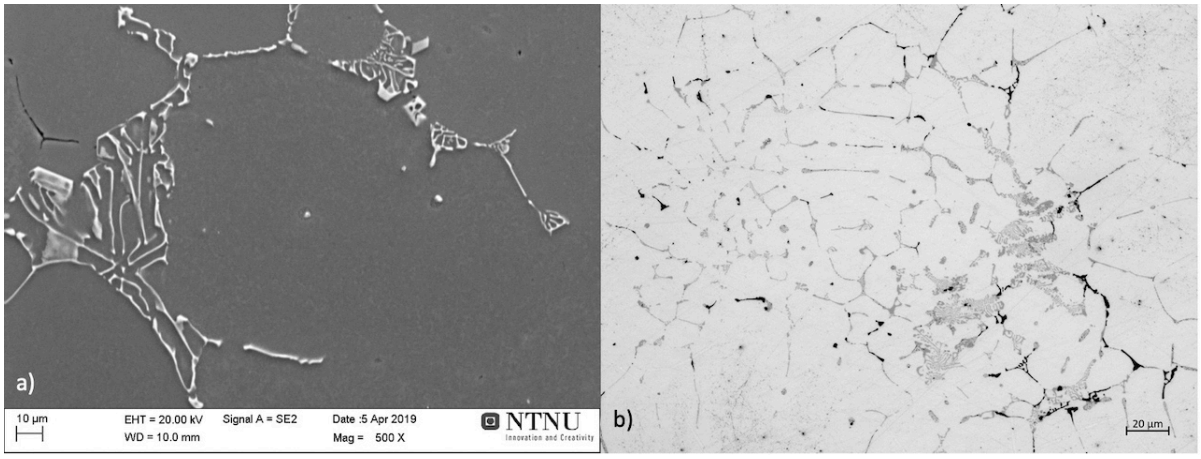

Figure 96: Pictures of the microstructure in cast 603; a) SEM picture of the slow cooled sample and b) LMI of the rapid solidified sample.

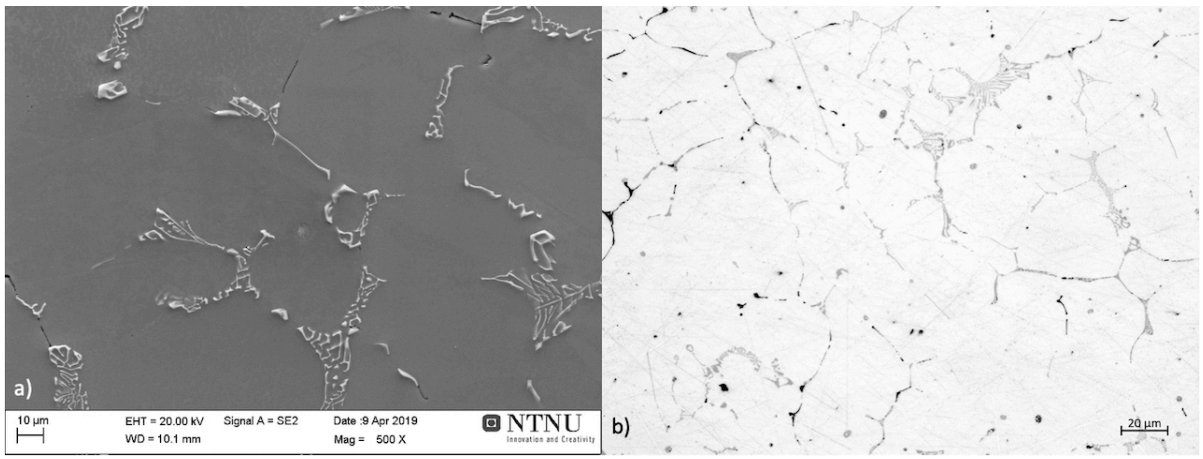

Figure 97: Pictures of the microstructure in cast 604; a) SEM picture of the slow cooled sample and b) LMI of the rapid solidified sample.

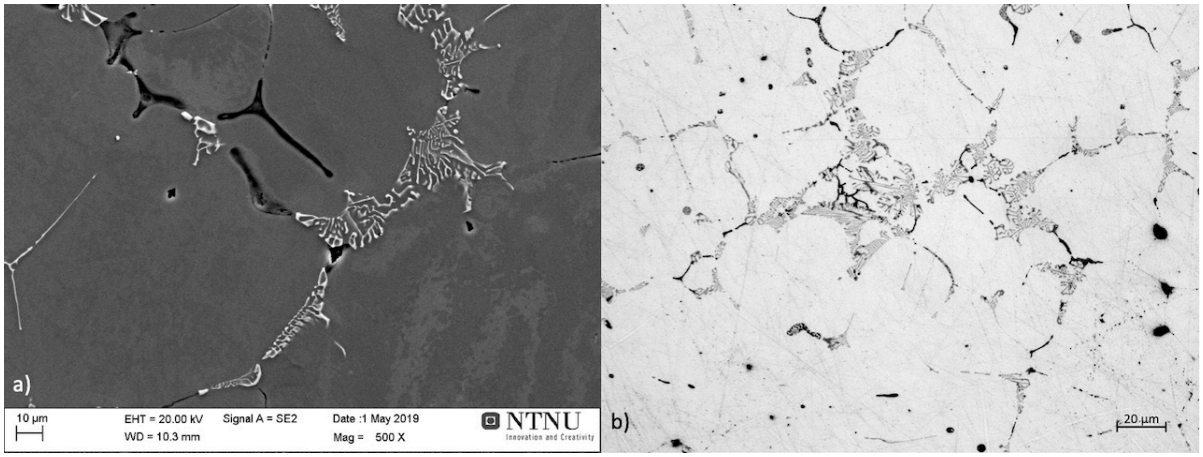

Figure 98: Pictures of the microstructure in cast 611; a) SEM picture of the slow cooled sample and b) LMI of the rapid solidified sample.

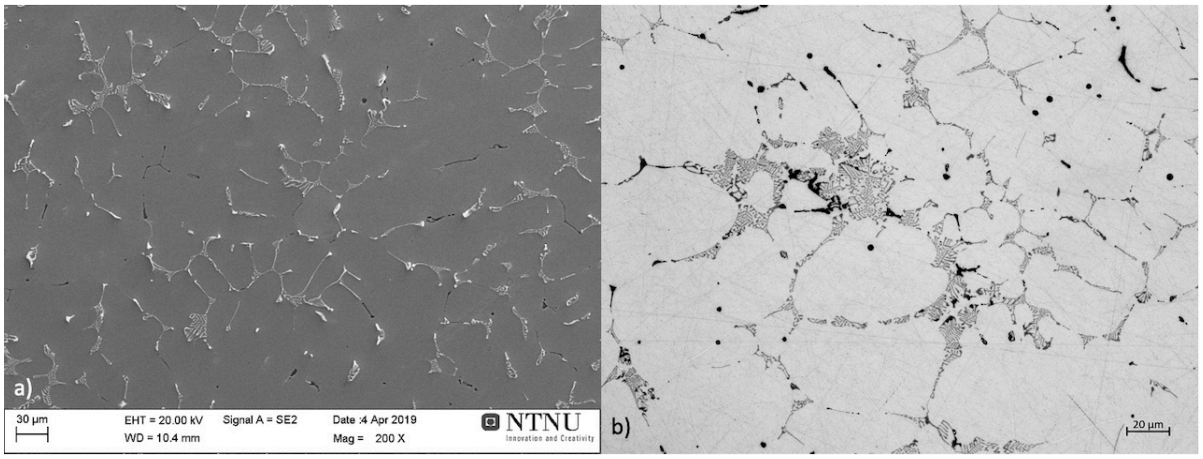

Figure 99: Pictures of the microstructure in cast 612; a) SEM picture of the slow cooled sample and b) LMI of the rapid solidified sample.

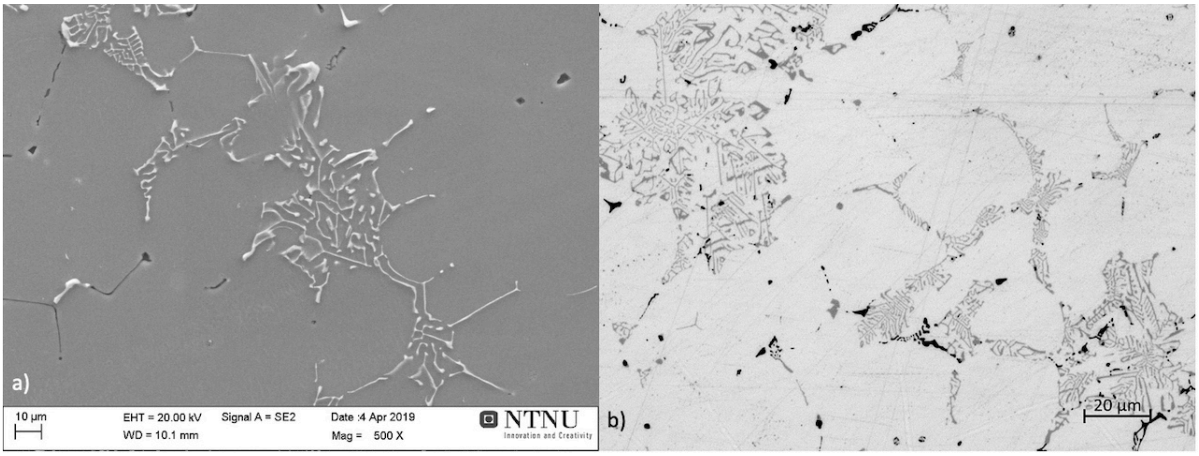

Figure 100: Pictures of the microstructure in cast 613; a) SEM picture of the slow cooled sample and b) LMI of the rapid solidified sample.

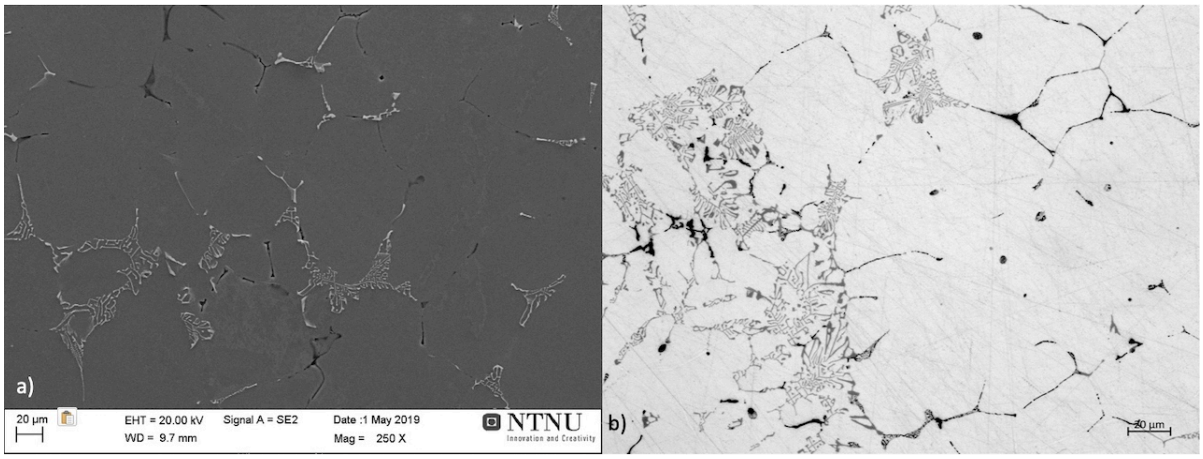

Figure 101: Pictures of the microstructure in cast 614; a) SEM picture of the slow cooled sample and b) LMI of the rapid solidified sample.

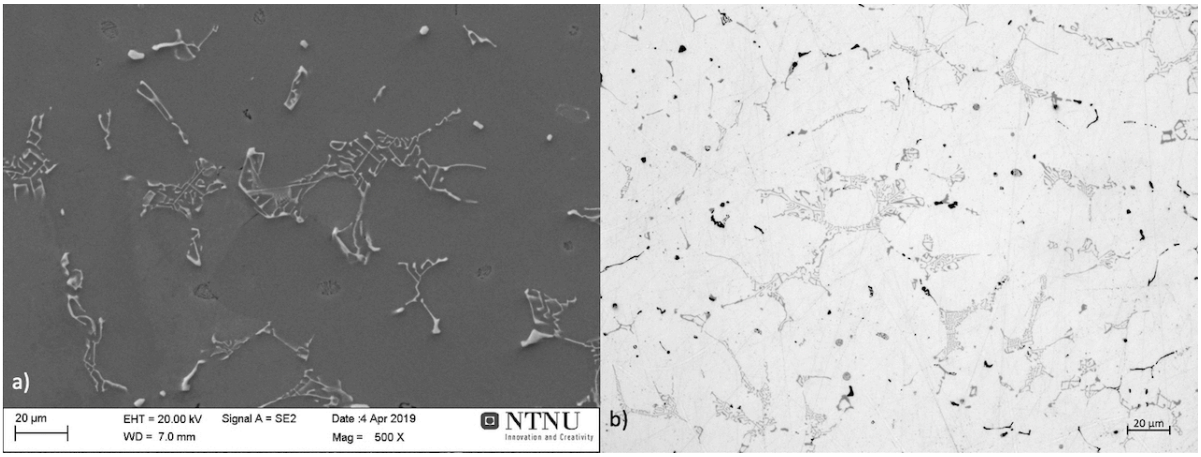

Figure 102: Pictures of the microstructure in cast 621; a) SEM picture of the slow cooled sample and b) LMI of the rapid solidified sample.

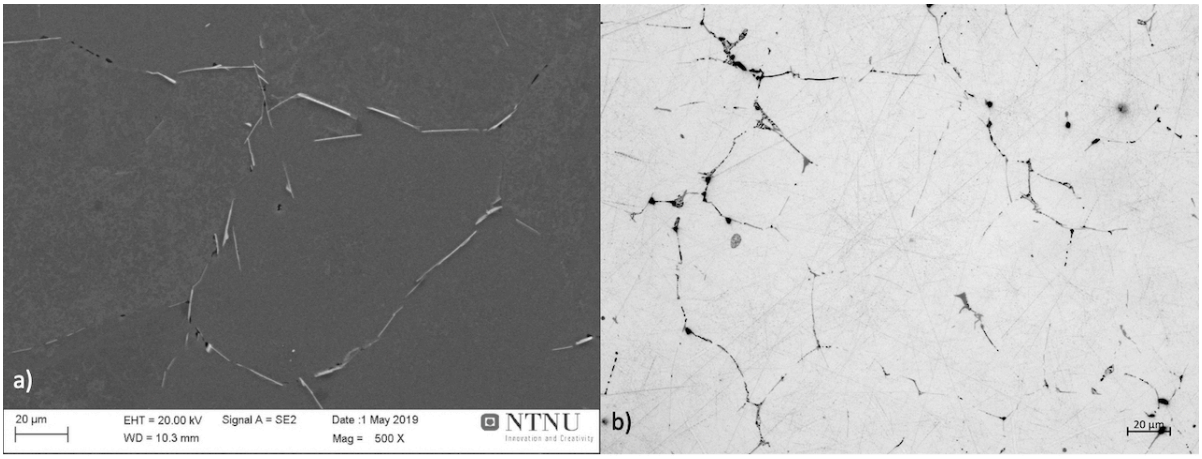

Figure 103: Pictures of the microstructure in cast 622; a) SEM picture of the slow cooled sample and b) LMI of the rapid solidified sample.

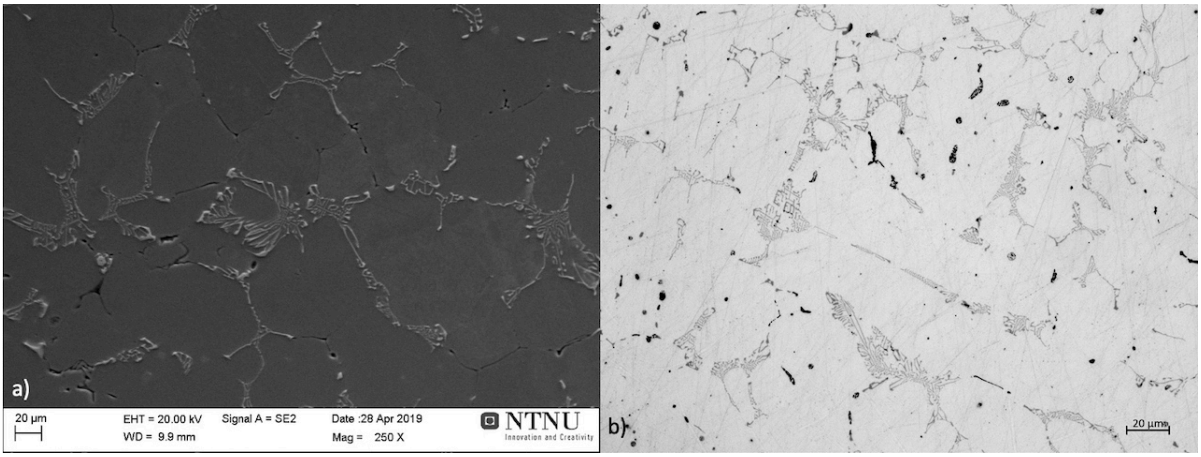

Figure 104: Pictures of the microstructure in cast 623; a) SEM picture of the slow cooled sample and b) LMI of the rapid solidified sample.

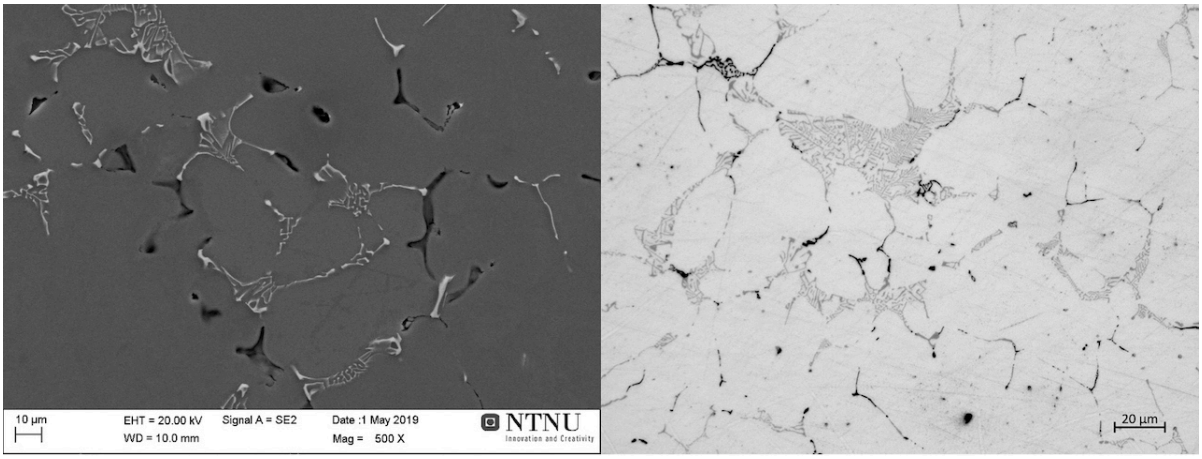

Figure 105: Pictures of the microstructure in cast 624; a) SEM picture of the slow cooled sample and b) LMI of the rapid solidified sample.

E 3103 EDS Analysis

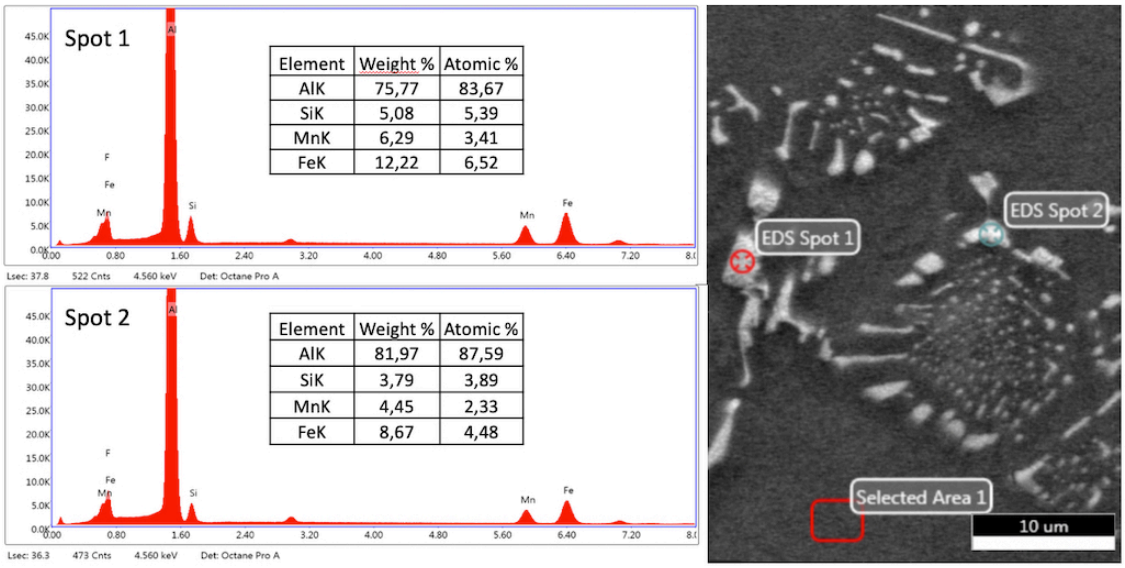

Figure 106: EDS analysis on sample 301, showing a possible α-phase.

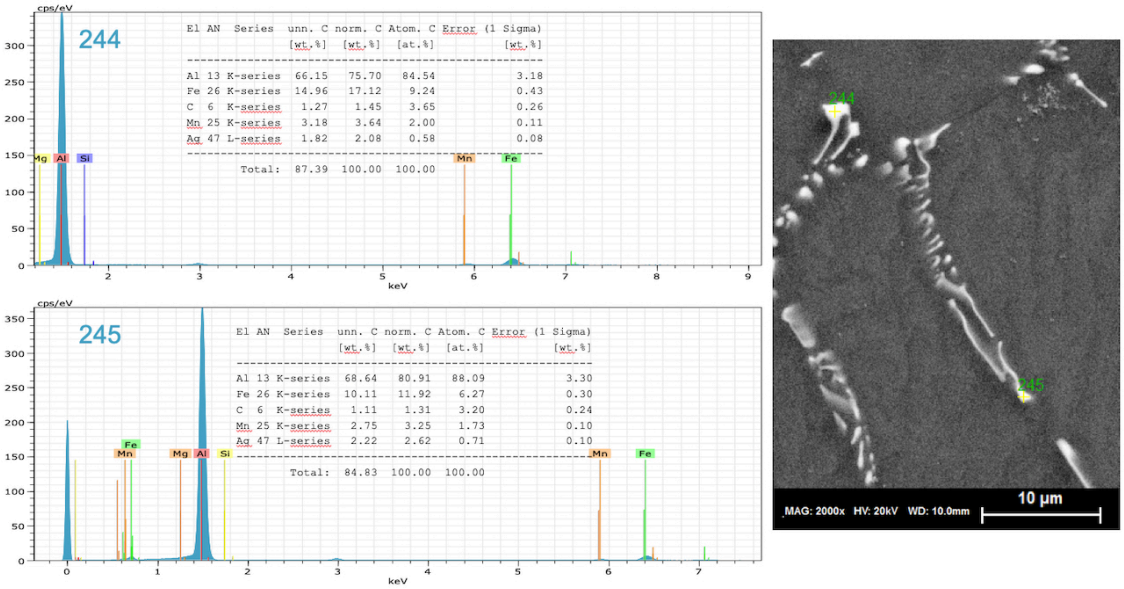

Figure 107: EDS analysis on sample 302, showing a possible $Al_6(Fe, Mn)$-phase.

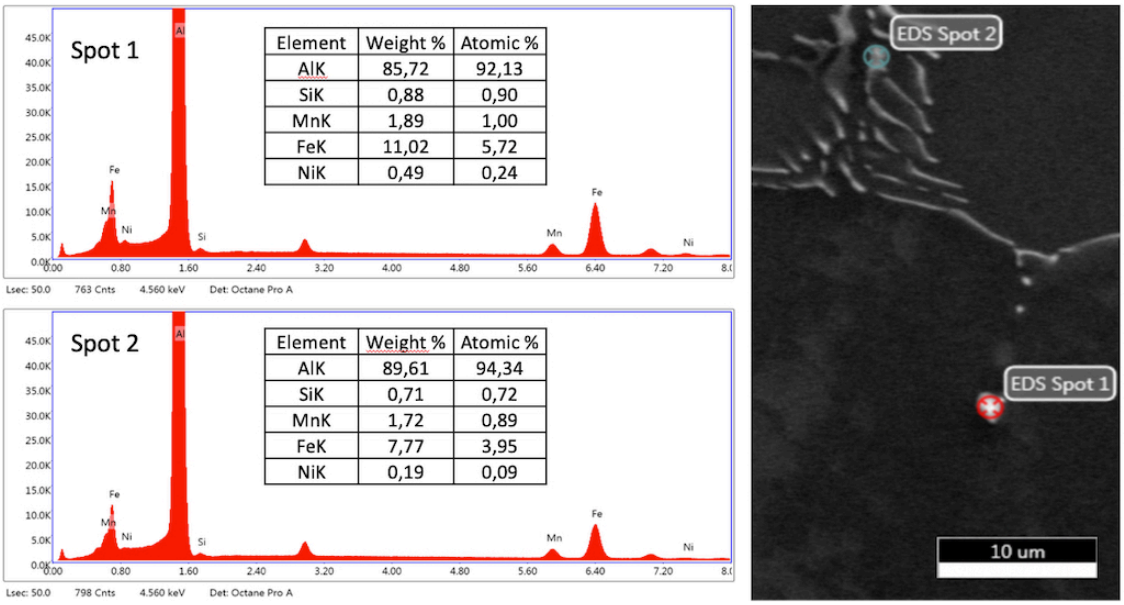

Figure 108: EDS analysis on sample 303, showing a possible $Al_6(Fe, Mn)$-phase.

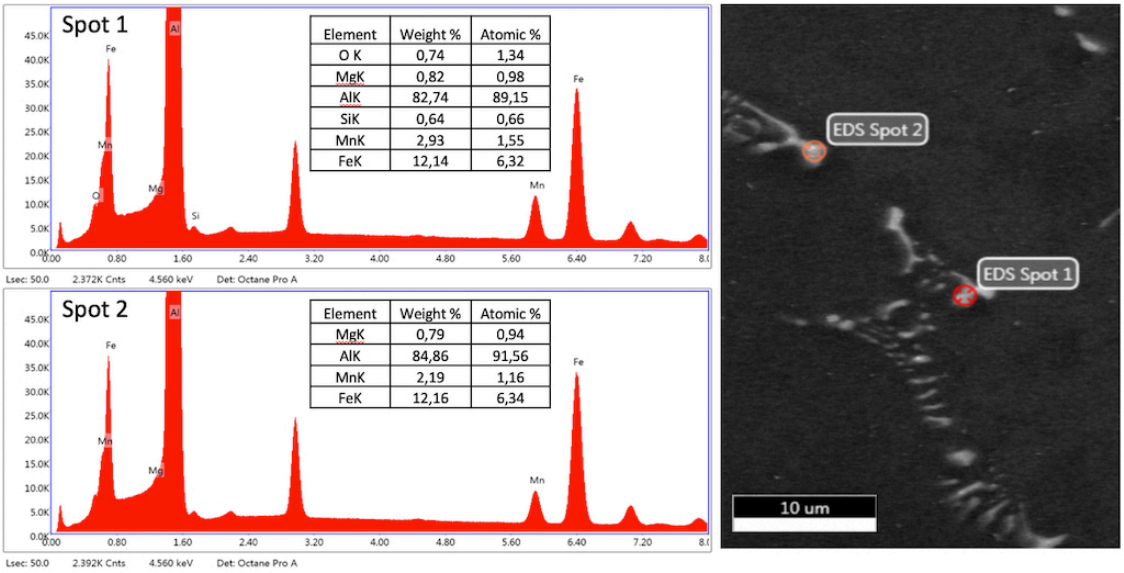

Figure 109: EDS analysis on sample 304, showing a possible $Al_6(Fe, Mn)$-phase.

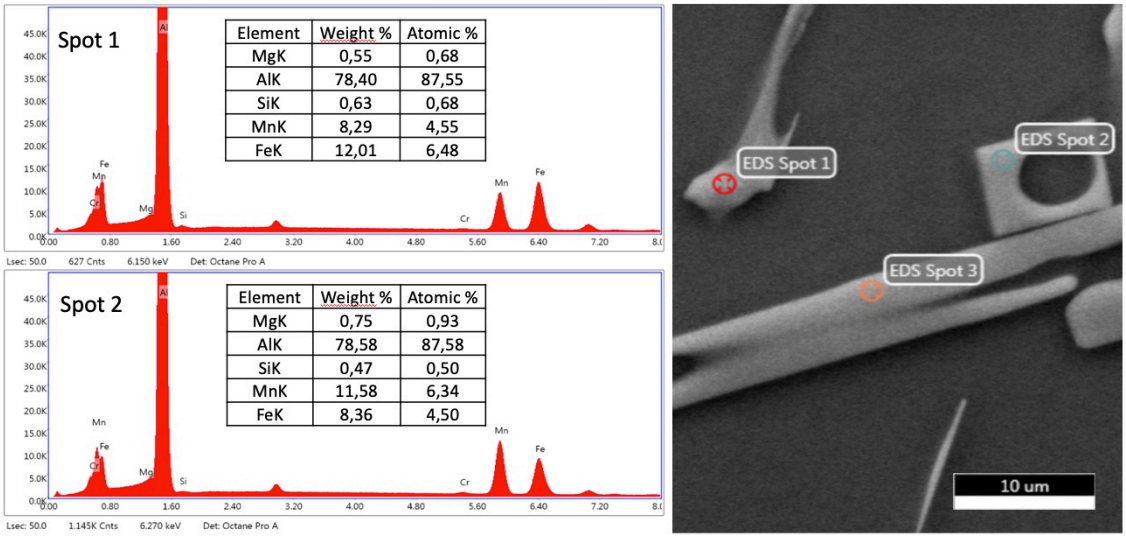

Figure 110: EDS analysis on sample 311, showing a possible $Al_6(Fe, Mn)$-phase.

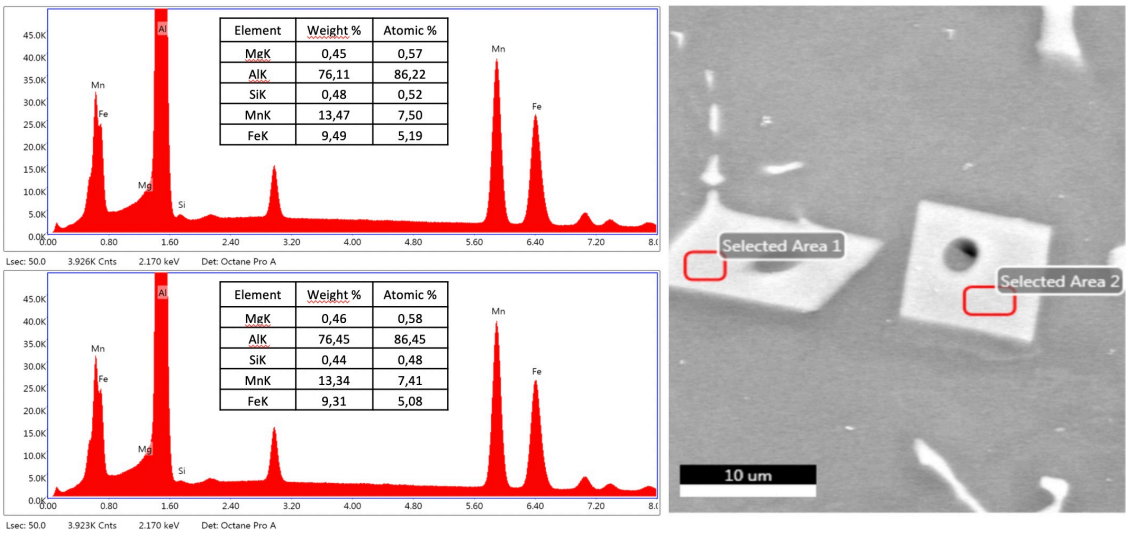

Figure 111: EDS analysis on sample 312, showing a possible $Al_6(Fe, Mn)$-phase.

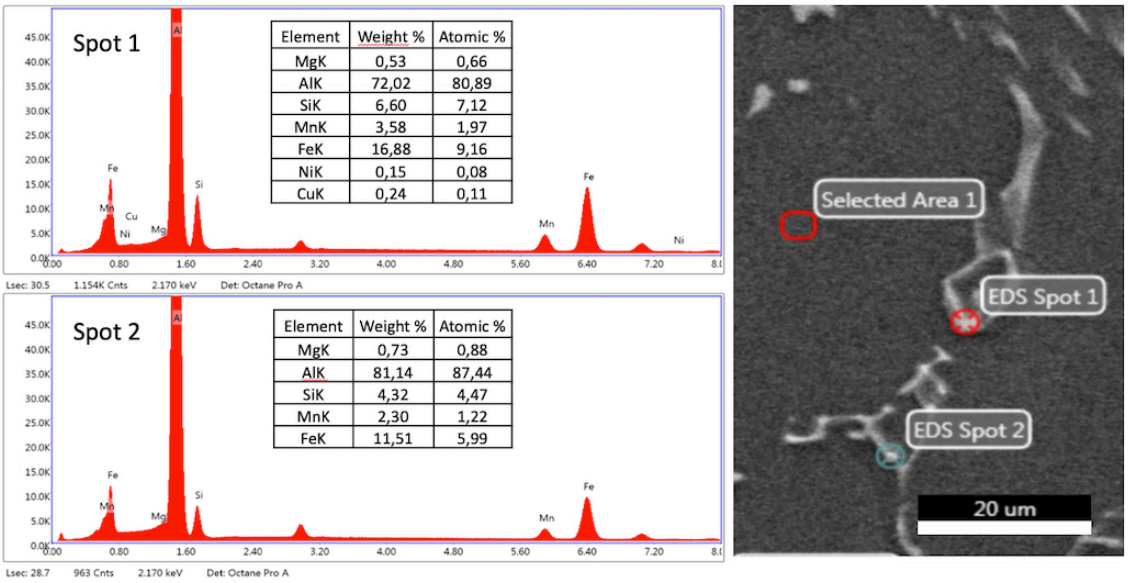

Figure 112: EDS analysis on sample 313, showing a possible $Al_6(Fe, Mn)$-phase.

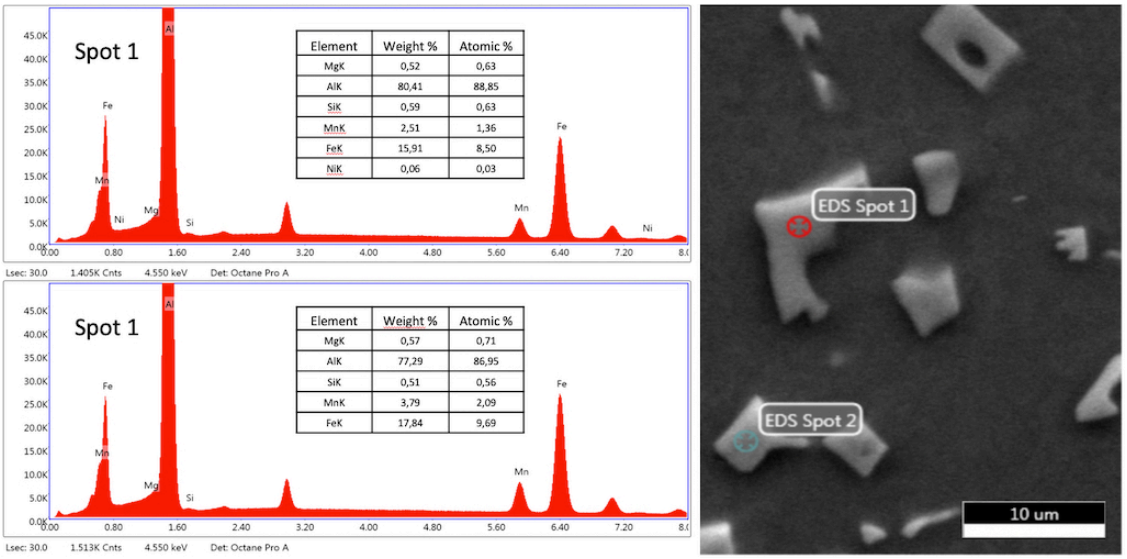

Figure 113: EDS analysis on sample 314, showing a possible $Al_6(Fe, Mn)$-phase.

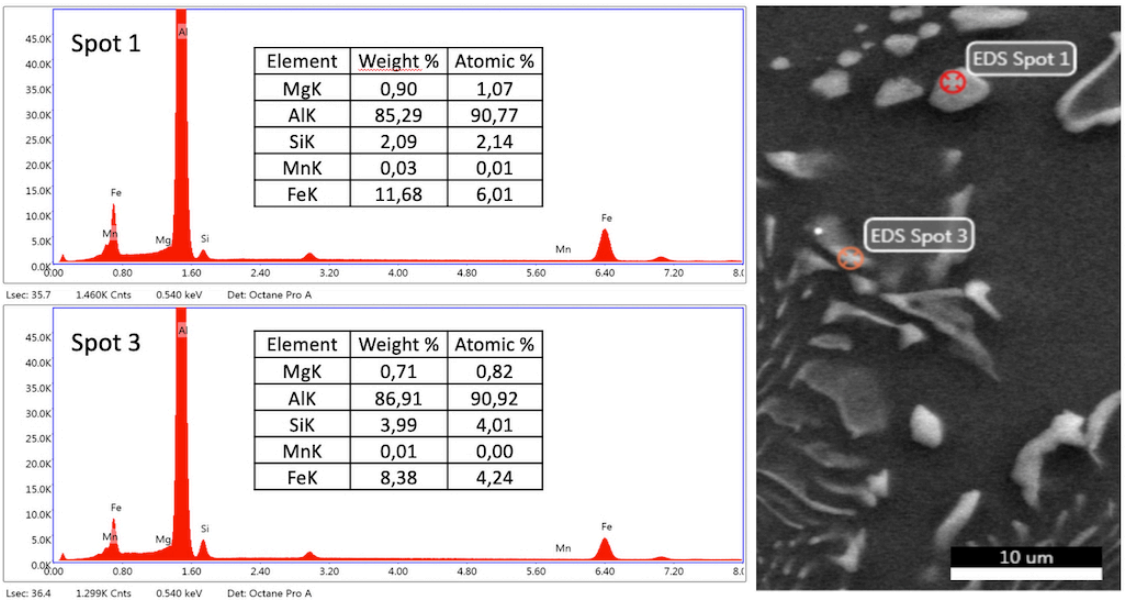

Figure 114: EDS analysis on sample 321, showing a possible α-phase.

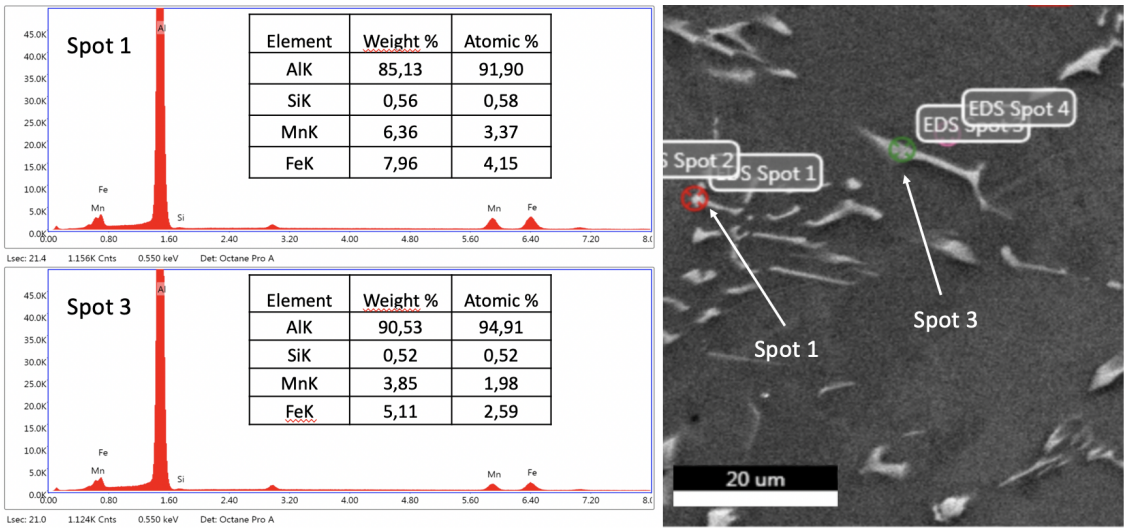

Figure 115: EDS analysis on sample 322, showing a unknown, script-like intermetallic phase.

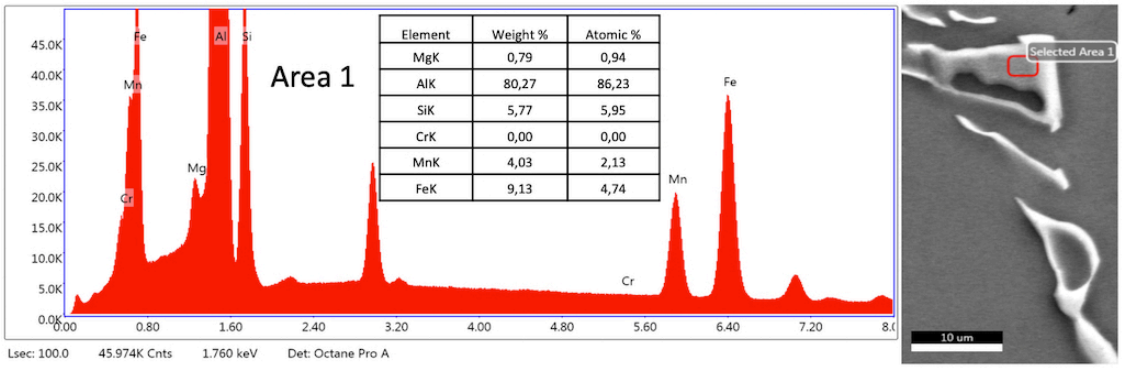

Figure 116: EDS analysis on sample 324, showing a possible α-phase.

F 6082 EDS Analysis

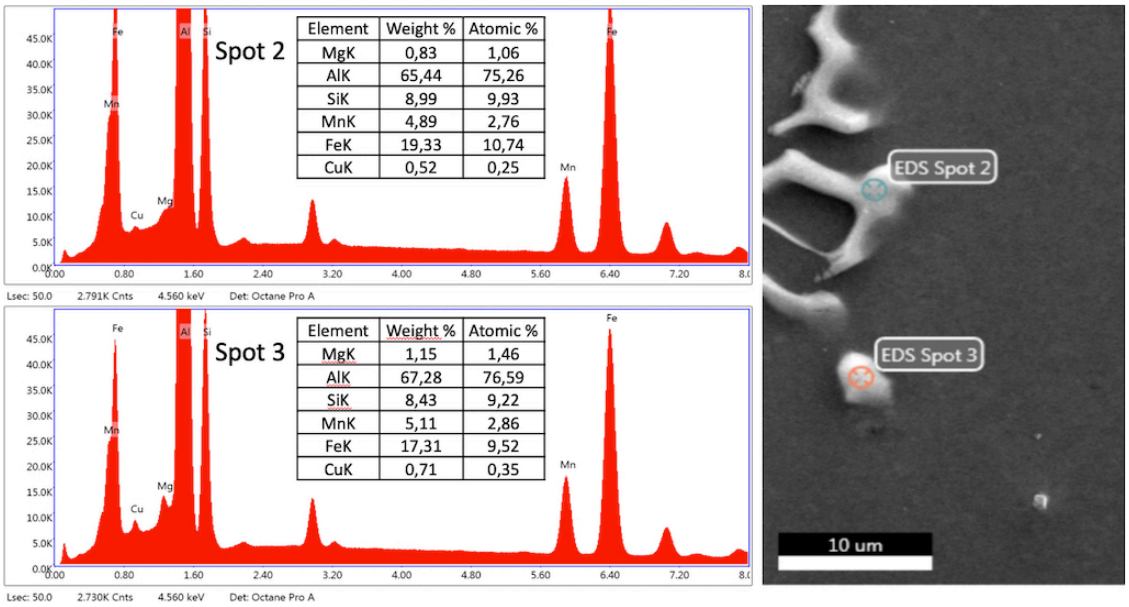

Figure 117: EDS analysis on sample 603, showing a possible α-phase.

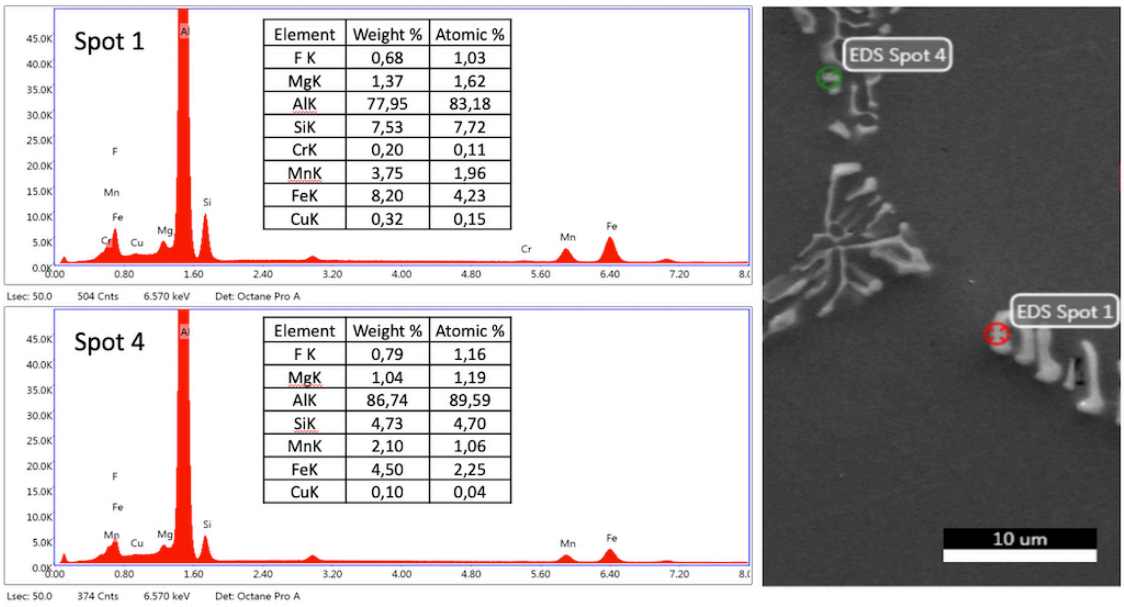

Figure 118: EDS analysis on sample 604, showing a possible α-phase.

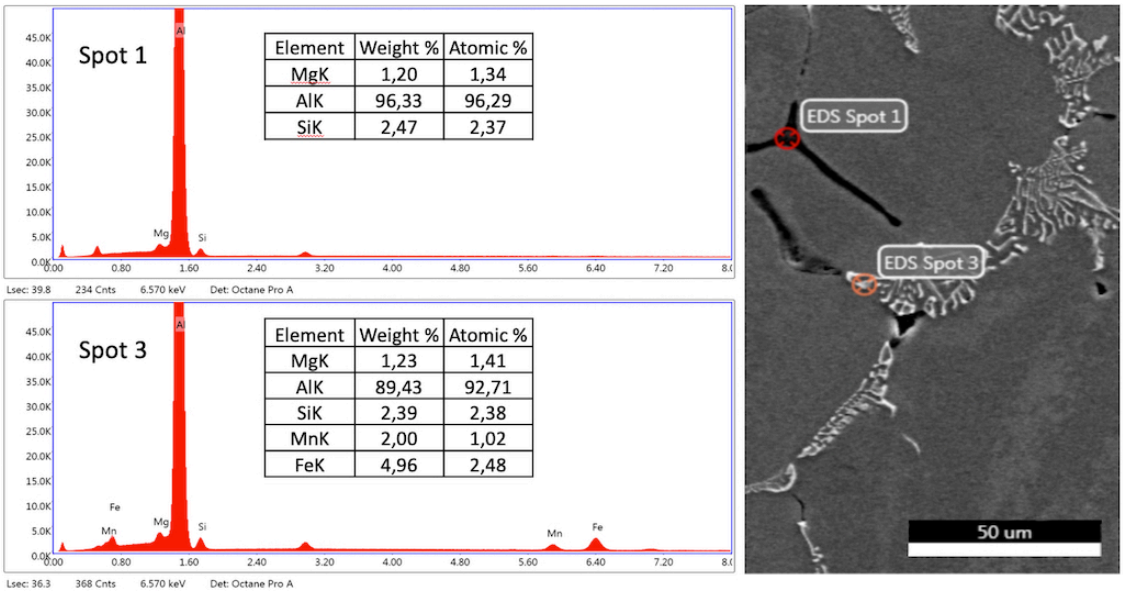

Figure 119: EDS analysis on sample 611, showing both a Mg_2Si phase, but also a possible α-phase.

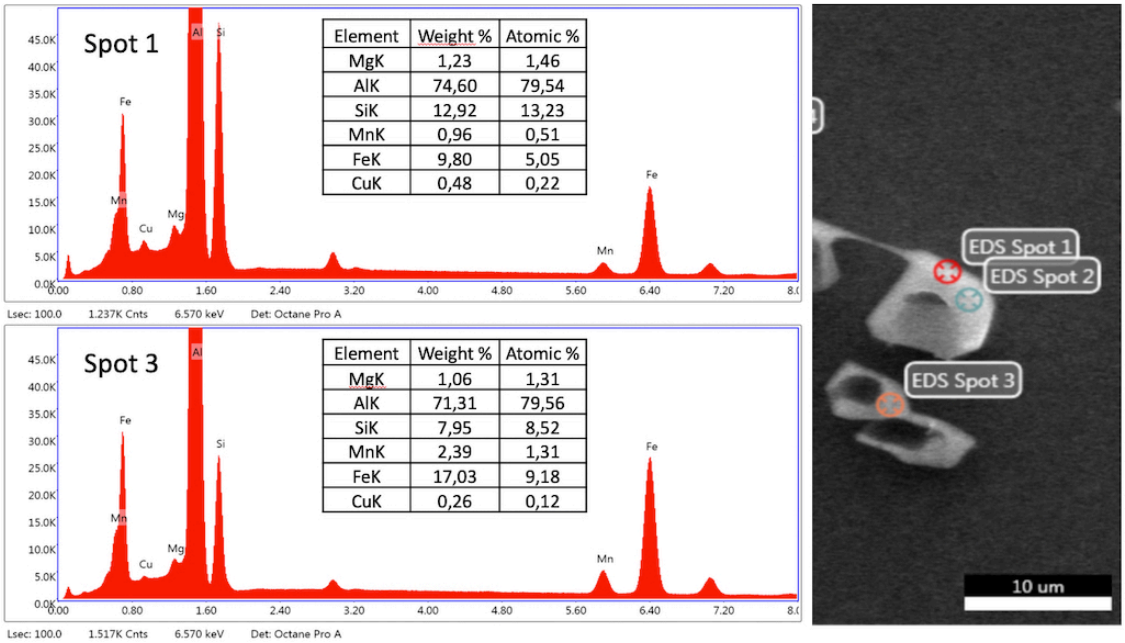

Figure 120: EDS analysis on sample 612, showing a possible α-phase.

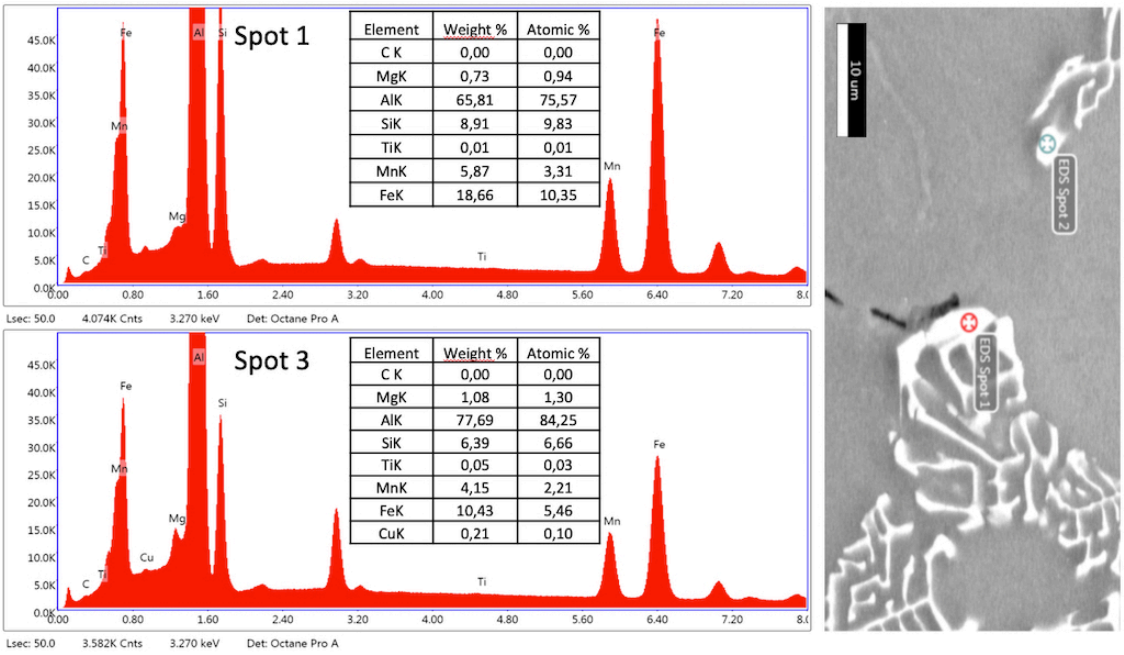

Figure 121: EDS analysis on sample 613, showing a possible α-phase.

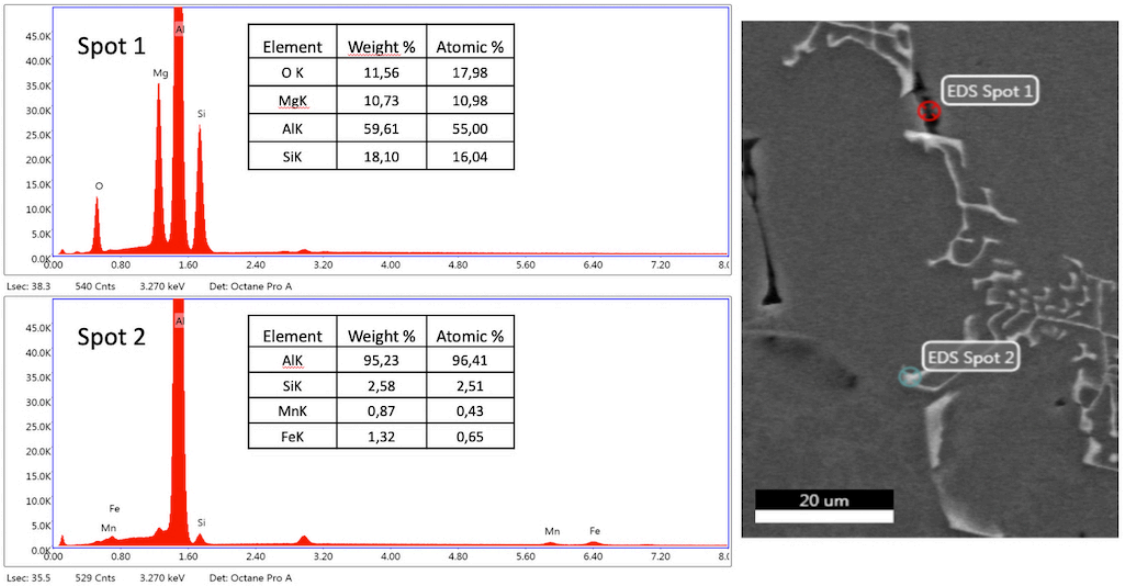

Figure 122: EDS analysis on sample 614, showing both a Mg_2Si phase, but also a possible AlFeMnSi-phase.

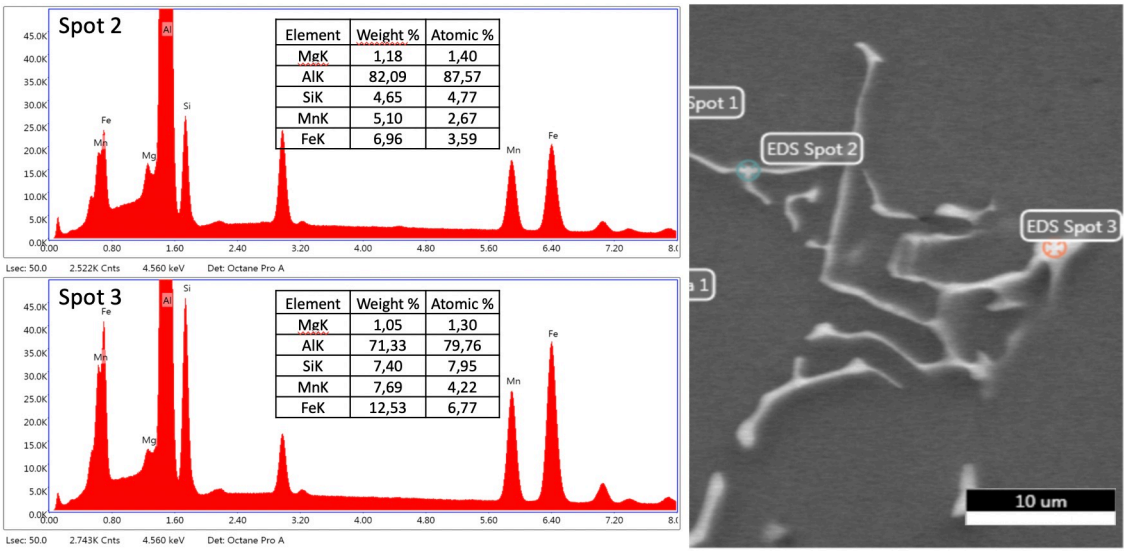

Figure 123: EDS analysis on sample 621, showing a script-like intermetallic phase.

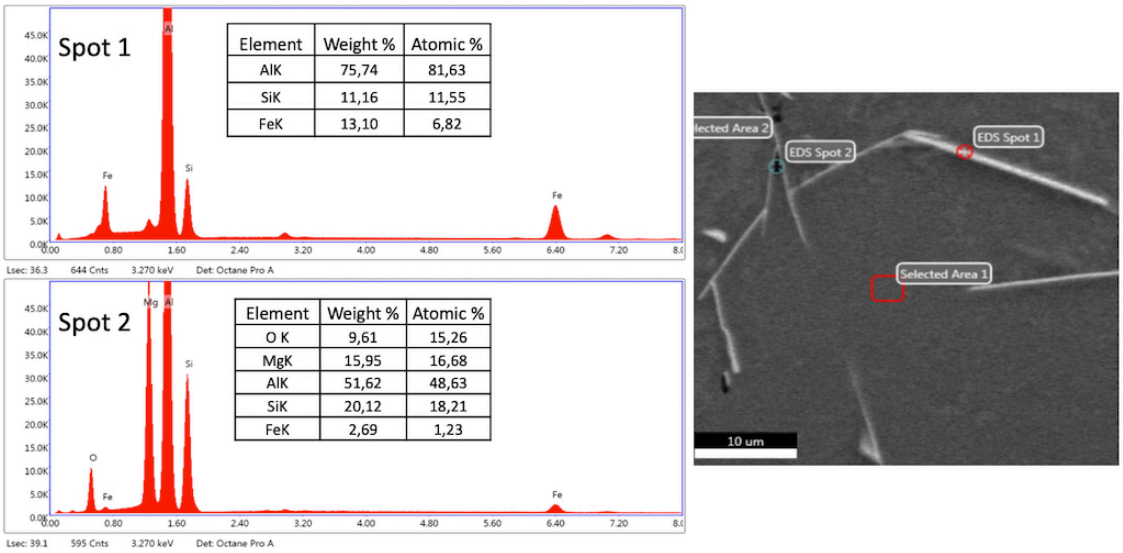

Figure 124: EDS analysis on sample 622, showing both a Mg_2Si phase, but also a possible β-phase.

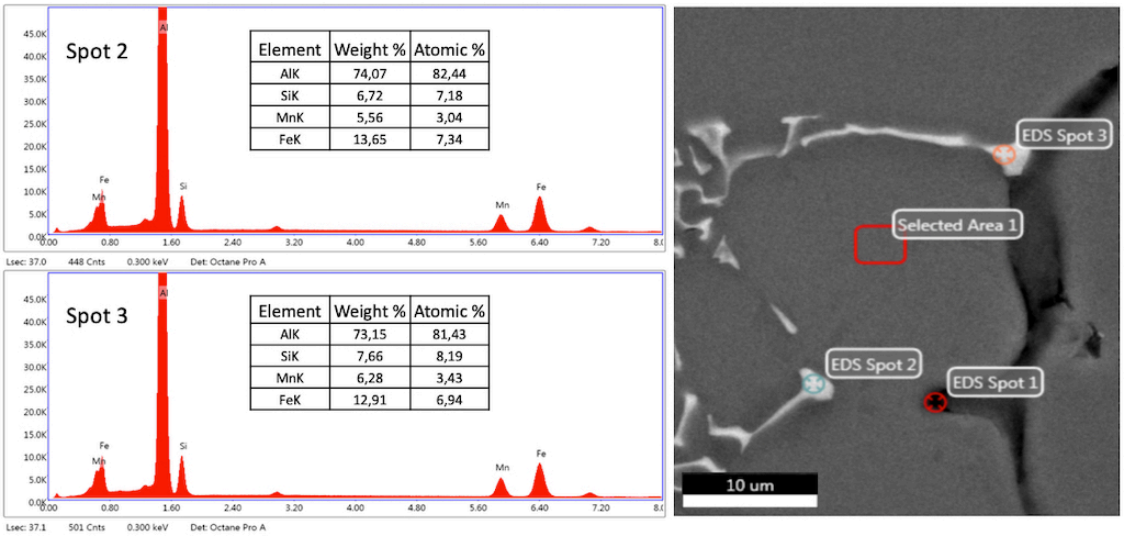

Figure 125: EDS analysis on sample 624, showing a α-AlFeMnSi phase.

G Timesheet

Table 17: Hours per person per week

Member/Week	2	3	4	5	6	7	8	9	10	11	12	13	14	15	16	17	18	19	20	21	SUM
Kjetil-André Sponland	6	7	22,5	19	26	33	33,5	23	31	39	46,5	18	35	29	0	36,5	67	36	55,5	76	639,5
Sebastian Grorud	6	5	22,5	19,5	26	35	32,5	23	16	34	48,5	23	31	30	0	38,5	70	36	54	77	627,5

H Popular Science Article

Challenges of recycling aluminium

Kjetil A. Sponland[1] **and Sebastian B. Grorud**[1]

[1]Undergraduates at Department of Material Science, NTNU

Quantitative speaking, aluminium is by far the most used light metal. It is also the metal with the largest area of application. Aluminium is used in everyday items such as drinking cans, to ship hulls, and all the way up to spacecraft parts. What makes aluminium so attractive, is how we can tailor it's properties after it's area of application by adding other periodic elements to it. These additions can enhance everything from corrosion resistance to machinability. The downside of having a metal used in these enormous quantities, is how to recycle it. Luckily for us, aluminium is pretty straight forward to recycle, and requires little work when other metals and materials are removed. The problems arises when other elements are added together with the aluminium in the melting process. If a computer or a phone is being recycled, and all of the steel screws are not removed, this can cause unwanted defects in the aluminium called defects.

Aluminium | Recycling | Impurities

Fig. 1. Al-furnace in a aluminium recycling plant (1).

Introduction. Aluminium does not exist in its pure form in nature, but as various ores containing oxygen. The main source of today's Al comes from the sedimentary rock bauxite, which contains mixtures of gibbsite ($Al(OH)_3$), diaspore (AlO(OH)), and boehmite (γ-AlO(OH)) (2). Aluminium was first extracted from these ores in 1825 by the Danish chemist and physicist, Hans-Christian Ørsted. Because of the difficulties in reproducing Ørsteds experiments, the credit of isolating aluminium often goes to the German chemist Friedrich Wöhler, who worked with Ørsted. The first time aluminium was synthesized electrolytically was in 1854, when the German chemists Robert Wilhelm Bunsen developed a small scale model to synthesize it. Unfortunately for them, it did not become the industry standard, due to the inefficient electrical supply at the time. It wasn't until 1889 that the two scientists Charles Hall and Paul Heroult discovered the Hall-Heroult process that is still used today to produce aluminium (3).

Recycling.

The aluminium sent for recycling need to be as clean as possible, It is therefore cleaned at the treatment plant before added to the furnace for reprocessing. When the aluminium melts, all the coatings/ink/glue melts and burns off. This can in theory be done an infinite amount of times, creating exactly the same aluminium from the primary process. In reality this is not true, as impurities from various sources will enter the metal that causes unwanted results.

> In 2009, Europe recycled 64% of all aluminium drink cans. In 2019 this number had increased to 73,6% (4)(5).

To manufacture 1 ton of aluminium from primary sources require 155 000 MJ of energy, manufacturing 1 ton of aluminium from scrap requires only 6909 MJ, a decrease of 95,5% (6). It is obvious that creating aluminium from already processed sources will be much cheaper. Another savings from recycling aluminium is the cut in CO_x production. Recycling aluminium does not require the mining of bauxite or the separation of Al from O, which reduces the emissions of greenhouse gases by considerable amounts.

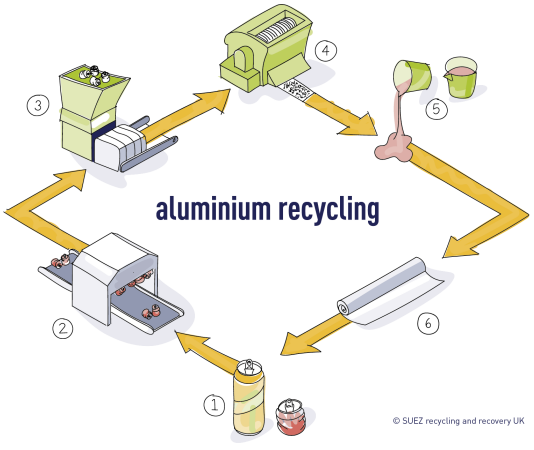

Fig. 2. Schematic flow chart of how aluminium is recycled (7).

Impurities in aluminium.

The addition of impurity elements as Fe in the aluminium melt gives unwanted properties in the metal. These additions

may cause the aluminium to lose the properties required to manufacture certain products as aluminium cans or car parts. Based on today's recycling rates the impurity levels in the aluminium is almost negligible.

The problem arises only when the amount of aluminium from recycled sources increase. The increasing amounts of recycled aluminium results in a higher degree of impurities in the metal. When the amount of impurity elements gets bigger, the bigger the problems becomes. The aluminium looses its ability to absorb energy before going to failure, it will require more energy to cast the molten aluminium in complex shapes, e.g. car bumpers.

> During WWII families were encouraged to save used aluminium foil, and in many cities they could trade the used foil against movie tickets. This was because aluminium was so vital for defensive efforts and construction of infrastructure (3).

As the % of aluminium that comes from recycled sources increases, steps to reduce the amounts of impurities in the metal needs to be taken. Stricter requirements on the separation of other metals before adding the scrap to the furnace would help reduce the amounts of impurities. If the impurity metals get added to the melt it will be to late to remove them, as impurity metals as Fe are extremely hard to remove from Al-melt, as they have similar properties when molten.

ACKNOWLEDGEMENTS
The authors are grateful for the help received by the two supervisors Dr. Robert Fritzsch and Prof. Ragnhild E. Aune. The authors would also like to thank Dr. Shahid Akhtar and Hydro for the materials provided for the experimental work, but also for the insight and information regarding casting of aluminium.

Bibliography

1. Figure: Furnace in aluminium recycling plant. https://dissolve.com/stock-photo/Worker-taking-sample-furnace-aluminium-recycling-royalty-free-image/101-D943-46-041, .
2. Bauxite, almost all of the aluminum that has ever been produced has been made from bauxite, article by: Hobart m. king, ph.d., rpg. https://geology.com/minerals/bauxite.shtml, .
3. The aluminium association: History of aluminium. https://www.aluminum.org/aluminum-advantage/history-aluminum, . (Visited 15:04, 14th May 2019).
4. Recycling aluminium, one can at a time. https://geminiresearchnews.com/2015/04/recycling-aluminium-one-can-at-a-time-2/, .
5. Aluminium beverage cans already well above the future eu circular economy recycling targets. https://european-aluminium.eu/media/2275/european-aluminium-press-release-2015canrecyclingresult.pdf, .
6. The Aluminum Association. Aluminum: The element of sustainability. a north american aluminum industry sustainability report. *The Aluminium Association*, pages 68–69, 2011.
7. Figure: What happens to aluminium waste? https://www.suez.co.uk/en-gb/our-offering/communities-and-individuals/what-happens-to-waste/recycling/cans, .